ABSTRACT

Title of dissertation: CRYOGENIC NEAR-FIELD SCANNING OPTICAL MICROSCOPY: QUANTUM DOTS, CHARGE-ORDERED DOMAINS, AND FERROMAGNETIC NUCLEATION

Paul Walter Kolb, Doctor of Philosophy, 2004

Dissertation directed by: Professor H. Dennis Drew
Department of Physics

Imaging of GaAs quantum dots (QDs) and the transition from charge-ordered insulator (COI) to ferromagnetic metal (FMM) in $Nd_{½}Sr_{½}MnO_3$ was achieved with sub-wavelength spatial resolution by means of near-field scanning optical microscopy (NSOM). To perform these imaging experiments, a cryogenic NSOM was developed. This instrument is compatible with high magnetic fields, has a novel capacitive sensor for *xy*-position measurement, and uses a novel light collection scheme with a parabolic mirror.

The NSOM was used to image GaAs QDs formed by monolayer islands in a 2 nm thick $Al_{0.3}Ga_{0.7}As/GaAs/Al_{0.3}Ga_{0.7}As$ quantum well (QW) by means of photoluminescence (PL). Discrete spectra associated with the QDs

are observed and studied. Individual QDs are imaged with a resolution of 150 nm. Quantum coupling of some nearby QDs is suggested by the observation of PL with identical energy emanating from two sources spatially separated by 300 nm. Modeling these candidate coupled QDs as monolayer islands with a "dumbbell" shape leads to a consistent description. PL excitation experiments were attempted to confirm the model but failed because of the low throughput of the near-field probes.

The NSOM was also used to image solid state structural phase transformations in $Nd_{½}Sr_{½}MnO_3$ which is known to exhibit two-phase coexistence. In particular, the transition from the low temperature COI to FMM which occurs at about 160 K was studied as a function of temperature. Both phases are shown to possess optical anisotropy in far and near-field imaging. Upon increasing temperature, the FMM phase is observed by far-field imaging to nucleate preferentially on variant boundaries and sometimes on twin boundaries, initially growing slowly and coexisting with the COI phase from about 155 K to 170 K. The NSOM is used to both image and measure the topography of FMM and COI twins. Polarization-dependent features are observed near the twin boundaries in the FMM and COI phases and are attributed to stress-induced birefringence. Upon increasing temperature near the transition to the FMM phase, polarization-dependent features appear on COI twin boundaries that are attributed to nucleation of the FMM phase.

CRYOGENIC NEAR-FIELD SCANNING OPTICAL MICROSCOPY: QUANTUM DOTS, CHARGE-ORDERED DOMAINS, AND FERROMAGNETIC NUCLEATION

by

Paul Walter Kolb

Dissertation submitted to the Faculty of the Graduate School of the
University of Maryland, College Park in partial fulfillment
Of the requirements for the degree of
Doctor of Philosophy
2004

Advisory Committee:

Professor H. Dennis Drew, Chair/Advisor
Professor Christopher Davis
Professor Theodore Einstein
Professor Romel Gomez
Professor Satish Ogale

DEDICATION

To my wife Giselle for her support.

TABLE OF CONTENTS

LIST OF FIGURES

I. Introduction

This dissertation covers three major topics. The first involves the development of a novel instrument, namely a cryogenic near-field scanning optical microscope (NSOM). The NSOM was used to perform imaging experiments at cryogenic temperatures on two different systems: one consisting of quantum dots (QDs) and the other of a particular manganite sample $Nd_{½}Sr_{½}MnO_3$. These two sets of experiments comprise the other two major topics of this dissertation. A chapter is devoted to each topic, while a brief introduction to each is provided here.

1.1 Near-field Scanning Optical Microscopy

Conventional optical microscopy has been a powerful measurement tool for hundreds of years. Its advantages include ease of use, fast capture rate, and large field of view. These advantages make conventional or "far-field" optics the best choice for most applications from biological to semiconductor systems. However, there is an important disadvantage. Diffraction implies a fundamental limit to the resolution of traditional optics of $\lambda/2$ (about 300 nm for red light) as first determined by Abbe [1]. This disadvantage becomes increasingly more critical as the systems of interest shrink into the nanometer range.

The recently developed technique of NSOM beats the diffraction limit and extends the range of optical resolution down to about 50 nm. The concept of

near-field microscopy was first proposed by Synge [2] and demonstrated for microwaves by Ash and Nicholls [3]. NSOM typically utilizes a sub-wavelength aperture probe which must be maintained in near-field proximity ($\lesssim \lambda/2$) to the sample. An image is generated as the probe is raster scanned over the sample with resolution on the order of the probe size.

NSOM is typically used to measure reflectance or transmittance, but it has been used in a large variety of experiments. A few examples are mentioned here as illustration. Fluorescence measurements have been made with NSOM to image individual molecules [4], including protein molecules in living cells [5]. Photoluminescence (PL) measurements have been made with NSOM to image individual QDs [6, 7], and NSOM has been used to coherently control QDs [8]. NSOM has been used to photoinduce carriers and thereby change the reflectivity of manganite [9] and YBCO samples [10].

Some samples reveal interesting results at cryogenic temperatures and in high magnetic fields. This group includes both the QDs and the manganite sample studied in this dissertation, and it is the motivation for building an NSOM able to operate in such extreme conditions.

1.2 Quantum Dots

As the name suggests, the energies of electron, hole, and excitonic bound states in QDs are quantized. QDs are “dot-like” or 0D in that the bound state wavefunctions are confined in all three spatial dimensions. Previous to the development of QDs, scientific research of 0D systems was largely limited to

the study of crystal impurity sites or isolated atoms or particles. Because they mimic the spectral properties of atoms, QDs are often referred to as artificial atoms. Unlike atoms, the properties of QDs can be engineered.

The emergence of QDs has been driven in part by their novel physics and the recent trend toward ever smaller semiconductor devices. In the early 1970s, molecular beam epitaxy (MBE) made it possible to grow crystals one monolayer at a time with high precision. Layers of different semiconductors could be sandwiched together making 2D structures known as quantum wells (QWs) [11, 12]. Now extensively studied, QWs have found applications in opto-electronics such as diode lasers and optical modulators. Additionally, narrow QWs exhibit monolayer fluctuations at the well interfaces that lead to further confinement in the growth plane [13, 14]. The QDs formed by these interface fluctuations are sometimes called “natural” or “accidental” dots. They are still an active area of research and are the type of QD probed in this dissertation. In the 1980s, *e*-beam lithography and etching techniques made it possible to deliberately produce structures with a controlled lateral dimension on the order of 30 nm [15]. However, the interlevel energy separation of lithographic QDs is low compared to natural QDs [16]. Furthermore, lithographic QDs typically exhibit impurities and structural imperfections which lead to inhomogeneous broadening and reduced photoluminescence (PL) yield [16]. In the 1990s, “self-assembled” QDs were developed. These dots form during two-dimensional MBE growth of strained layers due to thermodynamic instability [17]. For instance, as InAs grows on GaAs, a thin,

strained “wetting layer” forms followed by nucleation of strain-free InAs islands into disordered arrays. The size and shape can be somewhat controlled by growth conditions. Also of some importance are semiconductor nanocrystals which are precipitated out of organic liquids. There are other types of QDs presently being studied, and a more complete overview may be found elsewhere [16, 18].

The long term goal of QD research has been and continues to be the manipulation of single electrons, excitons, or photons in a controlled and coherent way. Applications of QDs in the next generation opto-electronic devices are being pursued and are perhaps not far away [19-22]. Still more ambitious is the use of QDs as quantum bits (qbits) in quantum computing. In this application, many single states must be addressed individually and coherently controlled to perform logical operations. There are already examples of coherent control of QDs [23]. To act as qbits, QD states must also interact or entangle in a controlled way. Presently, there are also examples of entanglement [24, 25]. However, any attempt to build a quantum computer must be viewed as a long-term project requiring a broad foundation of basic research.

Perhaps the most widely used and effective technique of probing single QDs is spectroscopy. In this way, the energy levels of QDs can be directly measured nondestructively. However, the high surface density of typical QD samples makes the resolution of single dots difficult to achieve. Some progress has been made in lowering the density of self-assembled dots [26]. Traditional

far-field microscopy can obtain resolution on the order of 400 nm while imaging with a solid immersion lens (SIL) extends this range down to 250 nm [27, 28]. Near-field methods, either *in situ* nanoapertures [14] or scanning probes [6], can achieve 50 nm resolution at the cost of optical throughput. Nanoapertures have the advantage that a single QD may be reliably found and isolated from its neighbors over the course of many experiments. However, near-field scanning optical microscopy (NSOM) has the capability to spatially scan a QD and its environment with the highest resolution presently possible. Recent experiments performed after those of this dissertation have used chemically etched high-throughput NSOM tips to image QDs with a resolution of 30 nm [7, 29]. It is this capability that should keep NSOM as a vital tool in QD research in the future.

1.3 Manganites

The pseudocubic manganites refer to the general class of materials with the formula $Re_{1-x}Ae_xMnO_3$ where Re and Ae refer to trivalent rare earth and divalent alkaline earth elements, respectively. The manganites have a crystal structure which closely resembles that of the mineral perovskite. In such a structure, six oxygen ions form an octahedral cage around a central manganese ion. The rare earth cations form a cube with manganese in the center and oxygen in the center of each face. These cations provide charge to the manganese-oxygen bonds such that the overall valence varies from Mn^{3+} at x = 0 to Mn^{4+} at x = 1. Manganese can only exist at valences of 3+ or 4+ in the

manganites. Coordination of spins of Mn *d*-electrons determines the magnetic properties of a particular manganite. Interaction of the electronic, crystal, and magnetic structures give rise to a wide variety of exotic properties and phases in the manganites. These properties and phases are a function of the *x*-doping and temperature.

Perhaps the best known exotic property of manganites is the magnetoresistance anomaly at the ferromagnetic metal (FMM) to paramagnetic insulator (PM) transition. First discovered in the 1960s, recent discoveries of very large magnetoresitance have led researchers to invent the name "colossal magnetoresitance" (CMR) [30]. With some exceptions, manganites tend to be insulators near room temperature. When near the Curie temperature in an insulating state, application of a magnetic field of a few tesla tends to align the manganese core spins. This allows conduction of valence electrons from manganese sites as mediated by the nearby oxygen atoms. The increased mobility of ferromagnetically aligned electrons leads to a lowering of the kinetic energy of the *d*-bands and an effective exchange energy for the Mn *d*-electrons called double exchange. The resulting reduction in electrical resistance can be as large as a factor of 10^7 at fields of a few Tesla.

Another important property of manganites is multiphase coexistence. This topic is one focus of this dissertation and has received considerable attention lately as recounted by Mathur and Littlewood in *Physics Today* [31]. Though perhaps simplistic and not applicable to all doping levels, their description serves as a good starting point for understanding the manganite phases. It is

applicable to the doping $x = ½$ in the $Nd_{1-x}Sr_xMnO_3$ sample studied in this dissertation. The three competing electronic phases of $Nd_{½}Sr_{½}MnO_3$ can be described as an insulating electronic solid, a poorly conducting electronic liquid, and a metallic electronic gas. They are alternatively denoted as charge-ordered insulator (COI), paramagnetic insulator (PM), and ferromagnetic metal (FMM), respectively. The equilibrium phase at a particular temperature depends on the competition of the processes known as the Jahn-Teller effect, double exchange, and charge-ordering due to on-site Coulomb repulsion. The Jahn-Teller effect is a consequence of strong electron-phonon coupling for singly occupied degenerate orbitals and results in the localization of the Mn valence electrons via a self-trapping distortion of the crystal lattice. The distortion opens a gap at the Fermi level and results in an insulator. Double-exchange, first proposed by Zener [32], refers to a two-step process by which electrons jump from Mn^{3+} to Mn^{4+} sites via the intervening oxygen ions. Due to a large Hund's coupling, this hopping is maximized when the Mn spins are ferromagnetically aligned. At low temperatures for $Nd_{½}Sr_{½}MnO_3$, charge-ordering wins out, and the result is an antiferromagnetic insulator. As temperature is raised, double-exchange takes over, and a ferromagnetic metal forms. At still higher temperatures, double-exchange is overcome by thermal fluctuations that randomize spins, and a paramagnetic insulator results. The transition from one phase to another is first-order. This is demonstrated by discontinuous changes in various properties such as heat capacity, resistivity, magnetic susceptibility, and reflectance. Unlike the phase change of liquid to

ice, manganites can exhibit more than one phase over a finite range of temperatures due to the effects of strain fields when the phase transitions involve a structural phase transition.

$Nd_{½}Sr_{½}MnO_3$ was chosen for this dissertation because of the possibility of observing phase coexistence optically with the resolution afforded by NSOM. In order to do this, one must be able to make measurements over a range of cryogenic temperatures or drive the phase transitions by application of large magnetic fields.

II. Cryogenic Near-field Scanning Optical Microscope

This chapter explains why the effort to build a cryogenic near-field scanning optical microscope (NSOM) was undertaken and describes how individual systems of the device work. Novel features are pointed out. The systems are divided into two groups: 3D positioning of the NSOM tip and sample and collection of light to form an image. Of particular importance in the latter case is how the geometry of light collection and the polarization of light affect image contrast.

2.1 Operation at 4 K and 14 T

2.1.1 Motivation

The motivation for designing a cryogenic NSOM compatible with high magnetic fields comes from the physics of potentially interesting nanoscale systems. Two examples of such systems are the ones studied in this dissertation: quantum dots (QDs) and nanocrystalline domains in $Nd_{½}Sr_{½}MnO_3$. Since thermal excitations will hide the discrete nature of QD energy levels, low temperatures are essential. The magnetic field dependence of those energy levels allows definitive characterization of the quantum states of the QDs. The phase transitions of $Nd_{½}Sr_{½}MnO_3$ occur at cryogenic temperatures and can be driven by application of a magnetic field.

2.1.2 Design Constraints

Any design of a cryogenic NSOM compatible with high magnetic fields must conform to several rather severe constraints. Positioning systems must work at low temperatures despite differential thermal contraction and reduced piezoelectric displacements. Construction materials should be non-magnetic. The assembled system must be compact and durable to insert into a cryostat that fits the bore of the high-field magnet. Since the magnet sits in a cryostat several feet into the floor, all systems must be remotely controlled.

A schematic of the cryogenic NSOM inner workings is shown in Figure 2.1. The NSOM fiber is glued to a quartz oscillator. As the tip of the NSOM fiber is brought into near-field approach with the sample, the oscillator experiences a damping force which reduces its vibration amplitude. The measured amplitude acts as the feedback signal. The near-field approach of tip to sample is actuated by a piezoelectric element called a "bimorph." Light from the tip is focused on a coherent fiber bundle (not shown) by the combination of lenses and a parabolic mirror. Machine screws control the coarse *z*-positioning of the tip and the focusing of the optics. The sample is scanned under the tip by a piezoelectric tube with quadrated outer electrodes. Inertial sliders actuate coarse motion of the sample in the *xy*-plane. The *xy*-position is monitored via a capacitive sensor. The machined components of the system are primarily brass and titanium. The entire package fits within a double-walled cryostat, 2½ inches in diameter. The NSOM cryostat inserts into the cryostat of a 17 Tesla magnet manufactured by Cryomagnetics. The magnet cryostat is attached to an

isolation platform by Technical Manufacturing Corporation (TMC) that uses air pressure to isolate the platform from vibrations in the floor.

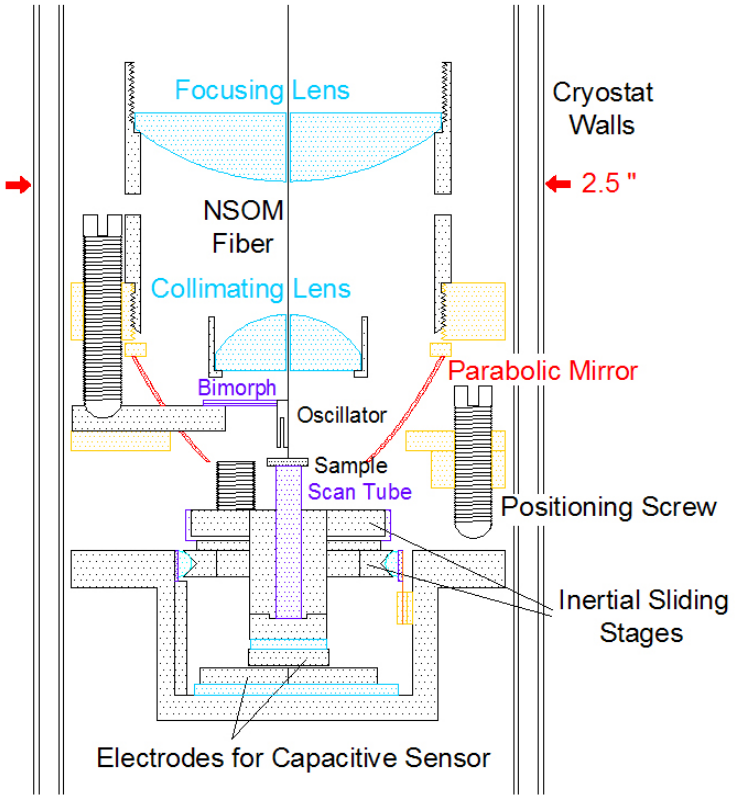

Figure 2.1. Inner workings of the cryogenic NSOM.

With the exception of the inertial sliders, the systems function at 4 K and 14 T. Problems can arise when ramping magnetic fields up or down due to the strong fringe fields that are generated. The isolation table can malfunction and cause the magnet cryostat to lean suddenly to one side. Loose objects in the room may become magnetically poled and violently collide with the magnet cryostat. If the NSOM tip is not retracted by at least several microns from the sample, these problems can cause the tip to break.

2.2 Sample Positioning

2.2.1 Probe to Sample Positioning

The shear force exerted on a tip vibrating parallel to the sample surface is used to control the tip height. This force is ideal for NSOM since its range is typically 50 nm or less. Though various shear-force schemes have been used in NSOM, perhaps one of the most popular, first proposed by Karrai and Grober [33], involves gluing the tip to a quartz tuning fork. Among the advantages of such a scheme, the tuning forks are small, cheap, and have large Q factors. Another important advantage is that no additional element is needed to vibrate or "dither" the tuning fork. In the variation used in this dissertation, also proposed by Karrai and Grober [34, 35], a voltage is applied to the leads of the fork, and the amplitude of the current is measured at the resonant frequency. Since gluing a tip to the fork leads to a broadening of the resonance, it has been found more favorable to use the in-phase component of current as shown in Figure 2.2. This signal current is measured with a lock-in amplifier and referenced to some set point. A proportional-integral (PI) control circuit supplies a voltage proportional to the sum of the integrated and direct difference between signal and set point. This voltage is applied to a piezoelectric actuator moving the tip up (down) when the difference is positive (negative). Lowering the set point below the signal causes the tip to lower until either the end of range is reached or the shear-force damping reduces the signal current to equal the set point. Plotting the amplitude of vibration versus height above the sample produces a so-called approach curve. An example of such a

curve is plotted in Figure 2.3. Noise in the vibration amplitude generally increases as the tip is lowered. However, the noise in the vibration amplitude is greatly reduced when the tip contacts the sample.

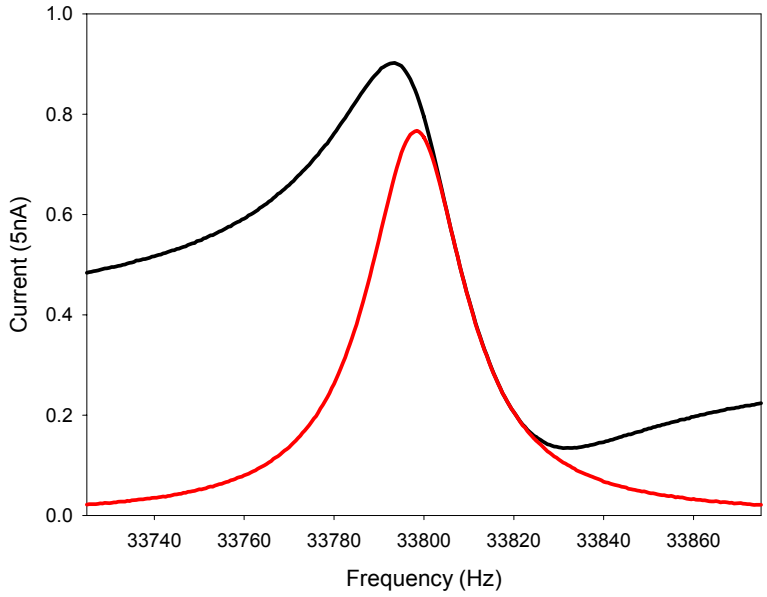

Figure 2.2. Vibrational spectrum of a quartz tuning fork with a glued tip. The black curve is the current magnitude. The red curve is the in-phase current.

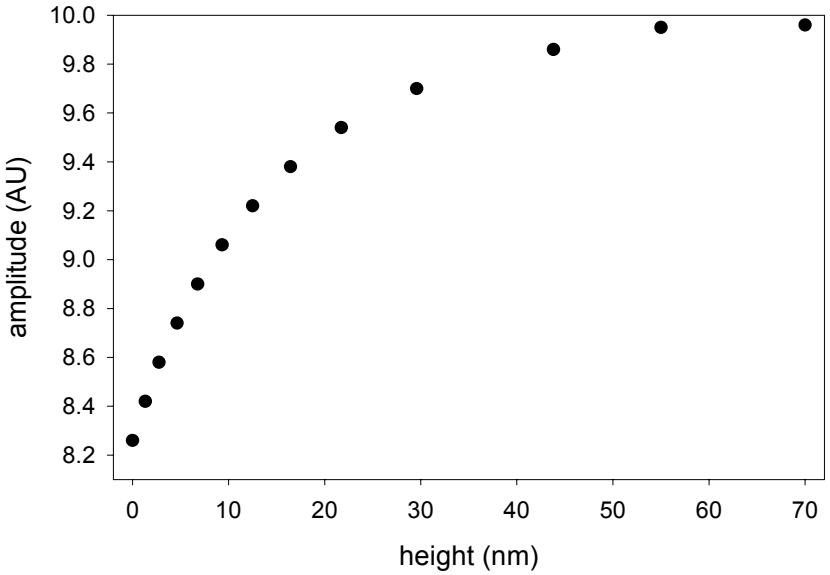

Figure 2.3. Example approach curve. Vibration amplitude is plotted versus tip height above the sample.

In order to achieve stable approach of the tip to the sample, the mechanical stability of the tuning-fork resonance is critical. It was experimentally found that the frequency and Q factor of the tuning-fork resonance are sensitive to stress applied to the NSOM fiber. As the *z*-motion of the NSOM tip is actuated, the measured amplitude of the tuning-fork resonance can change due to the changing stress on the NSOM fiber. If the measured amplitude decreases to equal the set point, the PI circuit does not lower the tip through the full *z*-range of the actuator. If the measured amplitude increases, the tip can be brought into deeper approach than desired. As a result the tip might "crash" the sample and be damaged. Additional problems may arise while scanning a sample as the *z*-position of the tip changes to follow sample topography. In particular, noise tends to increase as the tip-to-sample height decreases, the tip may crash the sample, or the tip can move up and out of approach during a scan. It was experimentally determined that the instability of the tuning-fork resonance was minimized when stress in the fiber was minimized. To alleviate the stress, the NSOM fiber was threaded through holes drilled in the collimating and focusing lenses as shown in Figure 2.1. Care was taken to position the tuning fork directly below the hole in the center of the collimating lens. The stability was generally best when there was only a slight amount of slack in the NSOM fiber. Despite the measures taken to reduce the instability, cooling the NSOM to cryogenic temperatures could result in an unstable resonance. Stability could usually be regained by mechanically adjusting the slack in the NSOM fiber via a feed-through at the top of the

cryostat or by adjusting the positioning screws. The instability proved to be nuisance but was never considered important enough to re-design the NSOM. In such a re-design, the tip would be kept stationary as the sample is *z*-actuated to approach the tip.

Optimizing the proportional and integral gain of the PI circuit is also critical for a stable approach. Otherwise ringing and even tip crash can result. Fortunately, the Laplace Transform, defined as $F(s) = \int_0^\infty f(t)e^{-st}dt,$ is ideal for modeling the NSOM approach system. Difficult integral equations become polynomial in Laplace space, where they can be solved more easily and transformed simply back into the time realm. Furthermore, Laplace Transforms of feedback systems are well known [36]. The approach feedback for the NSOM is shown schematically in Figure 2.4.

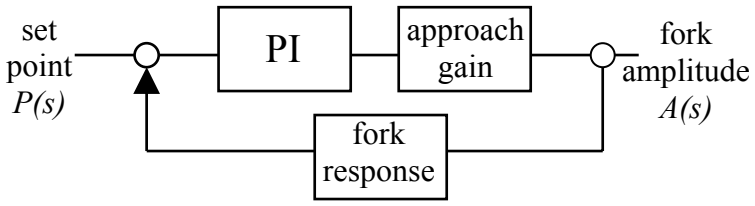

Figure 2.4. Schematic of the approach feedback for the NSOM. The difference between the set point and the measured amplitude is fed into the PI circuit. The output voltage of the PI is amplified and used to bring the tip into approach with the sample by lowering the tuning fork. As a result, the vibration amplitude of the fork is reduced until it equals the set point.

The Laplace transform for the NSOM approach system is given by

$$A(s) = 1 + \frac{\alpha\left(g_p + 1/s\tau_{RC}\right)}{1 + s\tau_F} P(s) = \frac{a_1}{s - s_1} + \frac{a_2}{s - s_2} + \frac{a_3}{s - s_3}, \qquad (2.1)$$

where *A(s)* is the tuning fork amplitude, *P(s)* is the set point, g_p is the proportional gain of the PI circuit, τ_{RC} is the time constant of the PI integrator, and τ_F is the response time of fork; the right hand side shows an expansion of *A(s)* in terms of its poles. From this expansion, *A(s)* is readily transformed into the time domain as a sum of exponentials. The parameter α could be termed an "approach gain" since it involves how the PI signal is converted to an actuating voltage on the bimorph which in turn reduces the fork amplitude as the tip comes into approach. It is taken as a constant, but its value really represents an average. This is because the approach curve, as seen in Figure 2.3, is not linear, and the value of α depends on the tip-to-sample height. To test Equation (2.1), step functions were applied to the set point while the tip was in near-field approach. The response of the fork amplitude to two consecutive steps in the set point is shown in Figure 2.5. To model the response, *P(s)* is set to *b*/*s*, the Laplace transform of a step function of amplitude *b*. Using known values of g_p, τ_{RC}, and τ_F, *A(s)* can be expanded in terms of its poles and transformed into a function of time as

$$a(t) = a_1 e^{-s_1 t} + a_2 e^{-s_1 t} + a_3 e^{-s_3 t}. \qquad (2.2)$$

The approach curve is used to approximate α for each step. The modeled response, also shown in Figure 2.5, is in excellent agreement with the measured response.

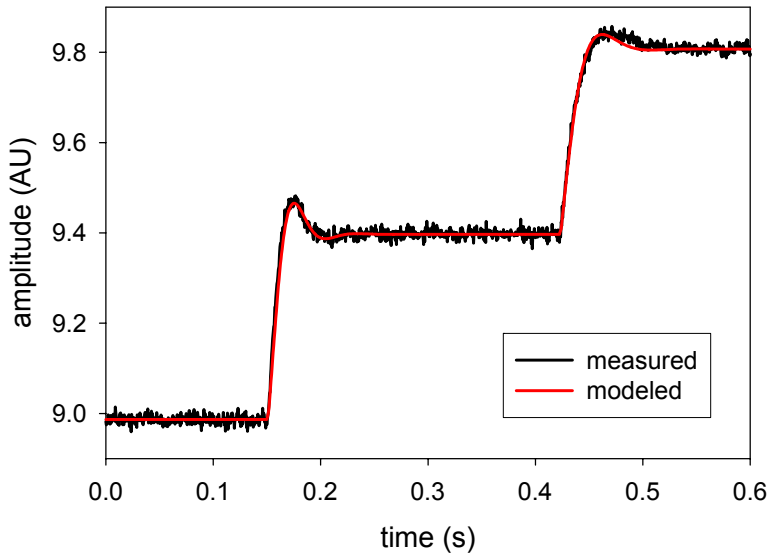

Figure 2.5. Measured and modeled response of the tuning fork. The feedback system is subject to consecutive steps in the set point with the tip in near-field approach.

A bimorph was initially chosen as the *z*-approach actuator because of its relatively large range and compact size. The bimorph consists of two oppositely-poled piezoelectric slabs glued to a metal strip. Applying a positive voltage to the upper electrode causes the top slab to contract along its length, the bottom to expand, and an overall upward motion of the free end. The bimorph has a range of motion of about 25 μm at room temperature down to about 1 μm at 4 K. Because the glue could potentially become rigid at low temperatures and limit range, the bimorph was eventually replaced with a so-

called “monolith” where the piezoelectric slabs are grown directly on the metal strip.

The coarse *z*-motion of the stage for the tip relative to the sample stage is accomplished by three 100-threads-per-inch titanium screws. The screws run through the brass tip stage to rest on sapphire pads on the sample stage. Dissimilar metals are used to prevent the screws from binding. Three similar screws are used to focus the stage for the optics, consisting of a parabolic mirror and a lens to collimate light, a second lens to focus light, and a fiber bundle (not shown in Figure 2.1) to transport the image out of the cryostat. The stages for the sample, tip, and optics are held together with phosphor-bronze springs. In the initial NSOM design, only one approach screw and one focusing screw could be driven via feed-throughs. The cryostat was later re-designed so all six screws could driven and better low-temperature focus could be achieved.

The evolution of the image of the tip reflected off the sample facilitates the coarse *z*-approach to the sample. This image is referred to as the virtual-tip image. There are actually two virtual-tip images: one formed by the parabolic mirror and one formed by collimating lens, both in conjunction with the focusing lens. In addition to these images, the actual tip can be imaged by the parabolic mirror in conjunction with the focusing lens, even when no sample is present. This is because a typical NSOM tip emits light over an angle that is large enough to be collected by the parabolic mirror. The actual-tip image can be focused to a spot by adjusting the *xyz*-position of the parabolic mirror. The

optical design is such that focus is maintained on the actual tip even while the tip is lowered to approach the sample. Conversely, the virtual-tip image formed by the parabolic mirror becomes visible only when the tip moves to within about 50 μm of the sample. This image initially appears as a wide ring, becomes smaller and brighter as the tip is lowered, and eventually collapses onto the actual-tip image. If the actual-tip image is poorly focused, it forms an interference pattern with the virtual-tip image as the tip is lowered. Independent of these two images and slightly displaced from them in the focal plane, a virtual-tip image is formed by the collimating lens in conjunction with the focusing lens. This image appears as concentric rings whenever a sample is present below the tip. As the tip gets closer to the sample and the image is focused, the rings collapse into a small spot.

2.2.2 Inertial-sliding Motors

The inertial-sliding motors, based on the design of Kleindeik [37], position the sample in the *xy*-plane. The principle of inertial sliding is shown in Figure 2.6. Application of a voltage causes thin piezoelectric plates to shear. If this is done with sufficient acceleration, static friction is broken and the plate slips relative to the load. The voltage is then removed slowly enough for the plate to pull the load with it. In principle, there is no limit to the range of motion realized in this way.

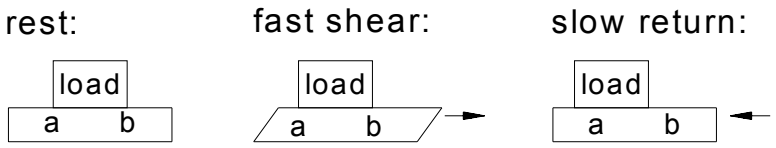

Figure 2.6. The principle of inertial sliding.

To facilitate sliding, sapphire half rods are glued to the piezoelectric slabs which index on *v*-grooves machined in the titanium sliders. The sliders are held in the *v*-grooves by beryllium-copper leaf springs. It was found by trial-and-error that the sliders work best when the spring is loose. To move the sliders at room temperature, a minimum of about 40 volts is needed, well below the 240 volt operating limit of the piezoelectric slabs. Speeds of several millimeters per minute could be achieved. There are points where the sliders tend to stick, and the voltage must be increased or the direction reversed to get them moving again. As the temperature is lowered, the piezoelectric displacement is reduced and sticking problems tend to get worse. At 4 K, the reliability of the sliders is very poor. Generally speaking, the lower slider works less well than the upper one, presumably because it bears its weight plus that of the upper slider. The performance of the sliders tends to degrade with time as titanium rubs off onto the sapphire half rods. Other potential problems include de-poling of the piezoelectric shears and dust on the sapphire. The construction of the sliders is shown in Figure 2.7.

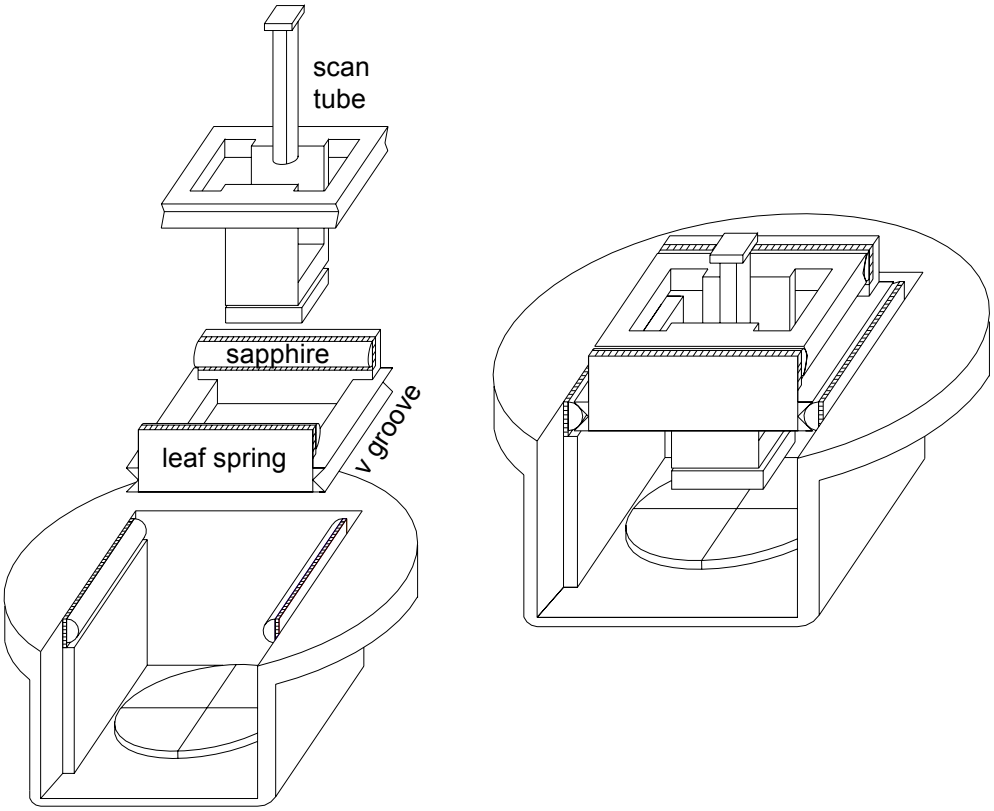

Figure 2.7. View of the inertial sliders exploded (left) and assembled (right). The thin piezo shears are striped for ease of viewing. Also shown are the piezoelectric scan tube and the quadrated electrode for the position sensor.

2.2.3 Capacitive Position Sensor

Considering the variable performance of the sliders with position, time and temperature and the lack of suitable commercial position sensors, a compact sensor was developed to measure the position of the sample stage in the *xy*-plane. The device, operating on the principle that the capacitance of parallel plate electrode depends on their mutual area of overlap, is compatible with high magnetic fields and cryogenic temperatures. Only a brief description

is given here, but a complete description of this device has been published elsewhere [38].

The sensor consists of planar metallic electrodes separated by a gap of about 0.5 to 1.0 mm. The top electrode, attached to the bottom of the lower inertial slider, moves above a stationary bottom electrode which is divided into four equally sized and electrically isolated quadrants. If edge effects are neglected, the capacitance of each top electrode-quadrant pair, denoted as C_1, C_2, C_3, and C_4, should be proportional to the respective overlap area. This is illustrated in Figure 2.8 (a). A current approximately proportional to the difference in capacitance between two adjacent quadrants is measured by the circuit shown in Figure 2.8 (b). A transformer is used to apply voltages to two adjacent quadrants while the remaining quadrants are grounded. The voltages between the two adjacent quadrants have the same magnitude V and frequency ω but are 180° out of phase. If the active quadrants are i and j, the current is ideally given by

$$I_{ij} = \omega V (C_i - C_j). \tag{2.3}$$

By means of a switch, currents from perpendicular quadrant pairs, I_{21} and I_{41}, can be measured. According to the overlap-area model of capacitance,

$$I_{21} \propto C_2 - C_1 = -2\varepsilon_0 \frac{x(y + d/2)}{z}, \tag{2.4}$$

$$I_{41} \propto C_4 - C_1 = -2\varepsilon_0 \frac{y(x + d/2)}{z}, \tag{2.5}$$

where d is the length of the top electrode (10 mm), ε_0 is the permittivity of free space, z is the gap between electrodes, and the origin is placed at the center of the upper electrode. Equations (2.4) and (2.5) provide a map between current measurements and the top electrode position.

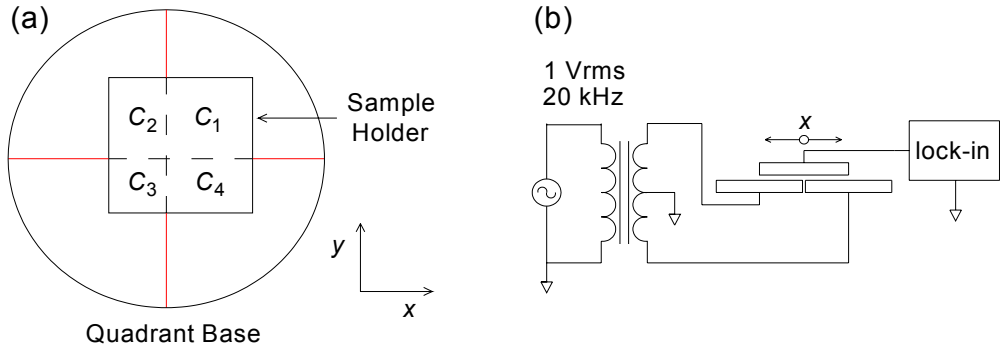

Figure 2.8. Schematic of the two dimensional capacitive position sensor. How the top electrode moves in the *xy*-plane changing the capacitance it forms with each quadrant is shown in (a). The circuit that measures the difference in capacitance between the top electrode and two adjacent quadrants is shown in (b).

To test the sensor, the upper electrode was glued to a flat surface mounted to a commercial *xyz*-translation stage. Directly below the upper electrode with a gap of about 430 μm, the quadrant electrode was glued to a flat surface mounted to the stationary block of the translation stage. A detailed account of the test is presented elsewhere [38], and only the conclusions are presented here. A resolution of approximately 1.2 μm was measured and was limited by the electronics used. The reproducibility of the position sensor was limited by the drift of the translation stage used to test the sensor and was

measured to be better than 3 μm. Equations (2.4) and (2.5) provided adequate predictions of the measured currents.

2.3 Light Collection and Image Formation

Understanding an NSOM image requires some interpretation and some knowledge of how the image is formed. To this end, the near-field probes used to generate the images, the polarization of light in these probes, and the geometry of collection are examined in this section.

2.3.1 Near-field Probes

The near-field probes used in this dissertation were fabricated by the common technique of pulling a laser-heated optical fiber. The details of this rather complex process are discussed elsewhere [39], and only brief treatment will be given here. The pulled fiber has a taper on the order of 500 μm and terminates in a blunt, flat end. All but the end of the tip is aluminized, typically with a thickness of 100 nm, to form an aperture. Figure 2.9 shows the taper and aperture of a typical tip. Due to losses in the taper, even the best pulled-fiber tips tend to have relatively low transmission efficiency or throughput. The throughput decreases strongly as aperture diameter decreases, and puts a practical lower limit of about 50 nm for usable near-field probes. Apertures of 100 nm fibers ideally have about 10^{-4} throughput [39]. As a practical matter, NSOM tips pulled with commercial fiber designed to transmit a single spatial mode at 1.55 μm were found to have better throughputs at optical wavelengths

than NSOM tips pulled with similar fibers which are single mode at optical wavelengths. This is perhaps because the 1.55 μm fiber has a larger core that is less lossy when tapered.

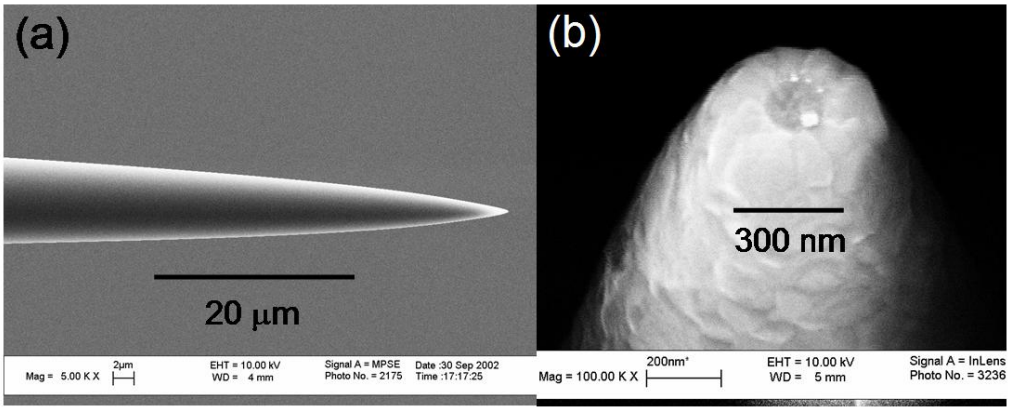

Figure 2.9. SEM images of pulled-fiber near-field probes. The taper of a probe is shown in (a). Aluminum surrounding the glass aperture of a probe [40] is shown in (b).

It is sometimes desirable to control the polarization of light when imaging with an NSOM. One way to do this is to use commercially available, 3-paddle polarization manipulators. These paddles stress the fiber in a way that varies as they are mechanically rotated. The stressed fiber becomes birefringent and acts to rotate the input polarization state. In principle, the paddles can rotate any input state to any output state, but the axis and amount of rotation cannot practically be known. Furthermore, bends anywhere in the fiber and asymmetries in the taper of the near-field tip can affect the output polarization at the tip. However, if the paddles, fiber bends and tip act together as a single arbitrary rotator, orthogonal input states should map into orthogonal output states. This can be achieved by launching orthogonal, linearly polarized

beams into the NSOM fiber. By trial and error, linear polarization of the far-field emissions of tips could be achieved with a typical extinction ratio of 200:1. Launching the orthogonal state resulted in a 90° rotation of the polarization of the output state and a similar extinction ratio. Because different spatial modes in the multimode fiber attenuate differently in the tapered tip, the intensity of the orthogonal output states can vary by as much as 50%.

2.3.2 Field Profile of an NSOM Tip

The near-field electric fields of an NSOM tip cannot be easily measured, but they have been calculated for a sub-wavelength aperture by Bethe [41] and Bouwkamp [42]. In his calculation, Bouwkamp uses oblate-spheroidal coordinates u, v, and φ defined by

$$z = auv,\;\; x = a\sqrt{\left(1-u^2\right)\left(1+v^2\right)}\cos\varphi,\;\; y = a\sqrt{\left(1-u^2\right)\left(1+v^2\right)}\sin\varphi, \qquad (2.6)$$

where a is the radius of the aperture [42]. For incident light polarized in the x-direction, Bouwkamp goes on to find the electric field components on the other side of the aperture [42]:

$$E_x \propto ikz - \frac{2}{\pi} ikau\left[1 + v\tan^{-1} v + \frac{1}{3\left(u^2+v^2\right)} + \frac{x^2-y^2}{3a^2\left(u^2+v^2\right)\left(1+v^2\right)^2}\right],$$
$$E_y \propto -\frac{4ikxyu}{3\pi a\left(u^2+v^2\right)\left(1+v^2\right)^2}, \qquad E_z \propto \frac{4ikxv}{3\pi\left(u^2+v^2\right)\left(1+v^2\right)}. \qquad (2.7)$$

The absolute values of these components have been plotted for a typical aperture size of 100 nm at typical heights above the sample in Figure 2.10. The electric field is dominated by E_x, but E_y and E_z are both present. Close to the

aperture at 3 nm, the component fields are most localized at the annulus of the aperture. The experimental consequence of this localization has been observed in at least one NSOM experiment [43].

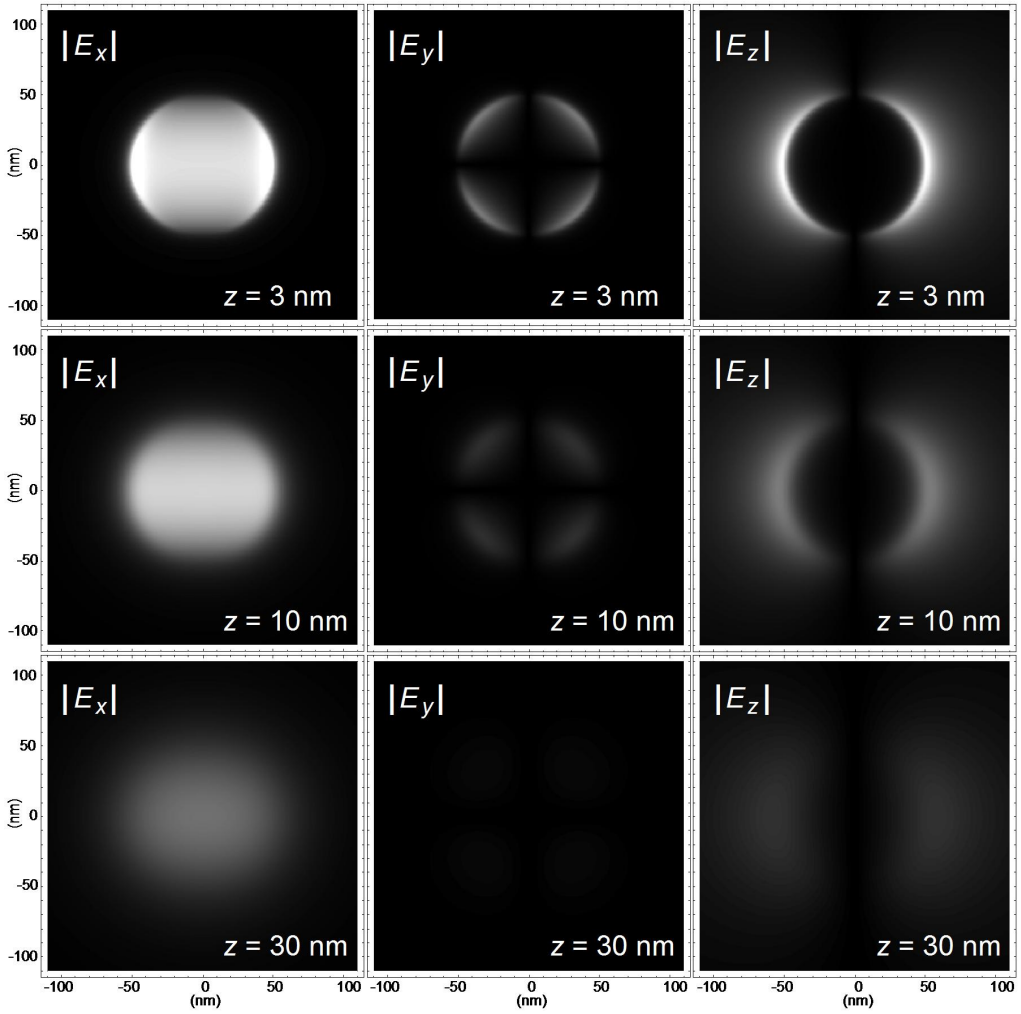

Figure 2.10. The electric field components near a 100 nm aperture illuminated by *x* polarized, 633 nm light based on the Bouwkamp solution [42]. The left, middle, and right columns are for the *x*, *y*, and *z* components, respectively. The components are plotted in the *xy*-plane for *z* = 3 nm, 10 nm, and 30 nm (top, middle, and bottom, respectively).

2.3.3 Illumination, Polarization, and Collection

The formed NSOM image depends strongly on the details of how light is polarized and collected. The two basic methods of light collection are transmission and reflection. In both methods, a near-field probe is typically used to illuminate the sample, and light is collected in the far-field. This is called illumination mode. The light path can be modified so that the near-field probe acts as the collector in either transmission or reflection. This is called collection mode. If the throughput is high enough, the near-field probe could be used for both illumination and collection [44]. In transmission NSOM, the polarization of illumination strongly affects the observed contrast. For example, the contrast of metallic lines on an insulator involves how the near-field coupling to the sample is affected by the boundary conditions on the electric field at the metal [45, 46]. In another instance, the contrast of twin domains were reversed by changing the polarization of light, domain boundaries were imaged, and the contrast was shown to be dependent of the numerical aperture of collection [47]. One might expect similar effects to exist in reflection NSOM.

The various important effects to consider in NSOM image formation in reflection include tip shadowing effects, the angle of light collection, and the symmetry of the collection geometry. Unlike transmission NSOM where there is no shadowing, tip shadowing tends to decrease the near-field light signal compared to the far-field signal, typically by a factor of 5 [48, 49]. The exact comparison will depend on tip size and shape [48] and the collection geometry.

A common cartoon picture used to qualitatively account for light collection artifacts due to tip shadowing is presented in Figure 2.11 [48, 50, 51]. Tip shadowing suggests that more light should be collected as the angle to the sample normal increases, and this does indeed seem to be the case [52]. At the time of writing this dissertation, no detailed study of near-field signal with collection angle could be found in the literature.

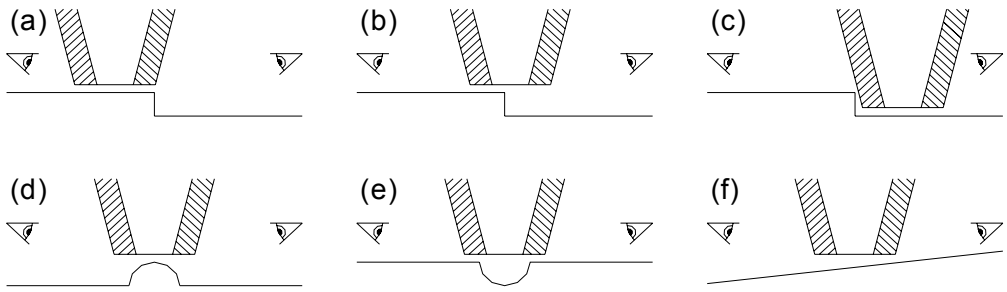

Figure 2.11. Cartoon of NSOM artifacts created by sample topography and detector position. Assuming an optically isotropic sample, the light collected by left (right) detectors should be (a) normal (normal), (b) normal (artificially bright), (c) artificially dark (normal), (d) artificially bright (artificially bright), (e) artificially dark (artificially dark), and (f) artificially bright (normal)

In the far-field, measurements of the angular emission profiles for small apertures have been made [53]. Consistent with Fourier optics where small apertures have high spatial frequencies, large apertures were found to have more collimated emissions than small ones. For linearly polarized light, the emission profile was found to be Gaussian and depended on the input polarization. For typical NSOM tips of about 100 nm, the full width at half-maximum (FWHM) was found to be about 110° (60°) in a plane parallel

(perpendicular) to the polarization. This result and how it might be relevant to the collected near-field signal is shown in Figure 2.12. Based on the far-field emission profile, a larger collection signal might expected in (a) than in (b). The large FWHMs of the far-field profiles indicate that a significant amount of light is actually backscattered. At 90°, the measured intensity was about half (one-tenth) the intensity at 0° in the plane parallel (perpendicular) to the polarization. This could potentially be responsible for adding a background to the collected near-field signal.

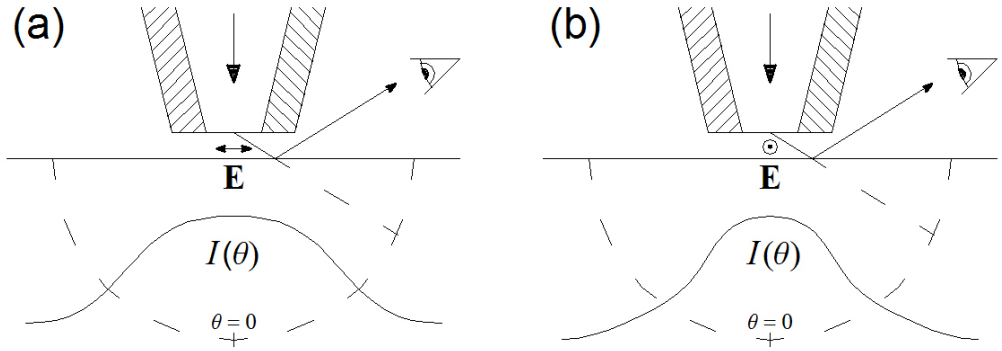

Figure 2.12. Cartoon on far-field emission profiles of small apertures and their possible influence on the collected signal from the near-field. Based on the broad far-field emission profile, a larger collection signal might be expected in (a). Experiments using asymmetric detection show that the larger signal comes from the configuration in (b) [51].

The tip shadowing effect combined with the broad emission profiles of near-field apertures suggest that reflection NSOM is not probing the optical properties for rays normal to the sample. Further evidence comes from an experiment using polarized light and an asymmetric collection geometry [51]. In addition to the topographical artifacts illustrated in Figure 2.11, a factor of 4

difference in collected signal from an aluminum test sample was observed depending on polarization and detector position. This result is depicted in Figure 2.12. This difference was explained by modeling the tip and sample as an effective waveguide and calculating the reflectivity of aluminum for TE and TM modes [51], but a simpler picture of radiating dipoles works perhaps even better. In this picture, radiating dipoles are induced in the sample along the direction of the electric field under the tip. The angular distribution of a dipole is well known to be $dP/d\Omega \sim \sin^2\theta$ where θ is measured from the axis of the dipole. Accordingly, the dipoles oscillating in the plane of the page in Figure 2.12 (a) should not able to radiate in the direction of the detector and the collected signal is dramatically reduced. The signal does not go to zero presumably due to scattered light, a finite numerical aperture for collection, and the vertical dipoles that are induced by the relatively weak E_z near the tip.

2.3.4 Symmetric Large-angle Collection

To maximize the light signal, the cryogenic NSOM was designed to collect light over a large angular range with a parabolic mirror. As an added benefit, the symmetric collection geometry and large numerical aperture should reduce the effect of artifacts, as other groups have reported [48]. Light propagating close to the normal of the sample can also be collected by a lens as shown in Figure 2.13. Misalignment may cause some degree of asymmetry, giving the collection system a preferred orientation. This is illustrated in Figure 2.14. In addition to misalignment, the collected light could potentially be

blocked by the tuning fork or bimorph, giving a bias to the collection orientation.

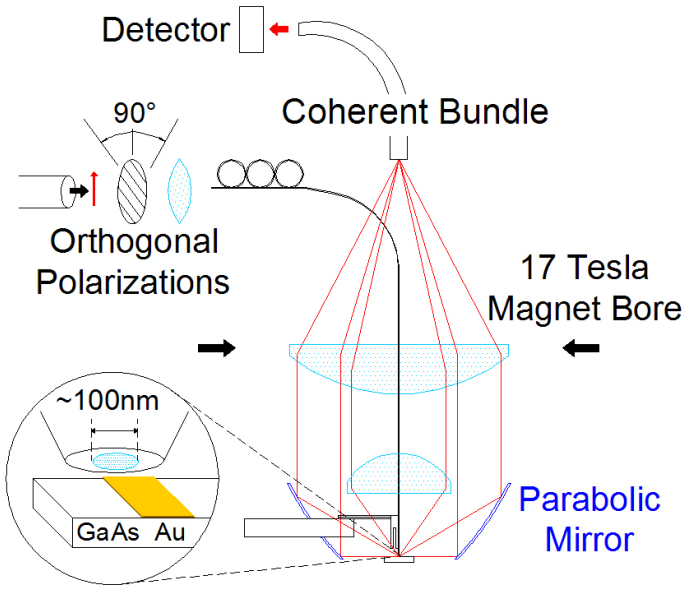

Figure 2.13. Light collection scheme for the low temperature NSOM. Light is sent through a fiber ending in the NSOM tip, interacts with the sample in close approach to the tip, and is then focused onto a fiber bundle. The polarization of light in the fiber is controlled with a three-paddle manipulator.

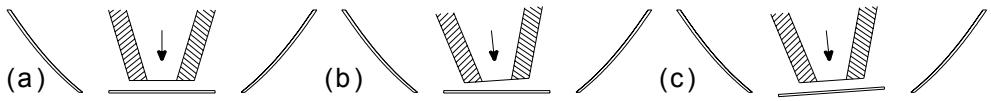

Figure 2.14. Collection asymmetry due to misalignment. Light collection in (a) is symmetric. Light should be preferentially collected to the right in (b) due to asymmetric tip-shadowing. Light should be preferentially collected to the left in (c) due to asymmetric shadowing of the mirror by the sample.

A sample consisting of gold (Au) lines on gallium arsenide (GaAs) was used to test the NSOM. The lines have a horizontal width of 1.0 μm and a vertical thickness of 50 nm. Figure 2.15 shows two NSOM scans of these lines

using orthogonal polarizations. As expected, sample topography plays a role in the collected NSOM signal. Small particles cause the tip to pull up and accordingly appear bright. The bright, Au plateaus appear wider than the dark, GaAs grooves due to the finite diameter of the NSOM tip. Straight lines may appear slightly curved due to piezo hysteresis, non-linearity and coupling of *xy* with *z*-motion. To correct for these effects and for sample tilt, a quadratic background is typically subtracted from the topographic images. The scales of nted in this dissertation is the fact that the Mn-O bonds in the ab plane are

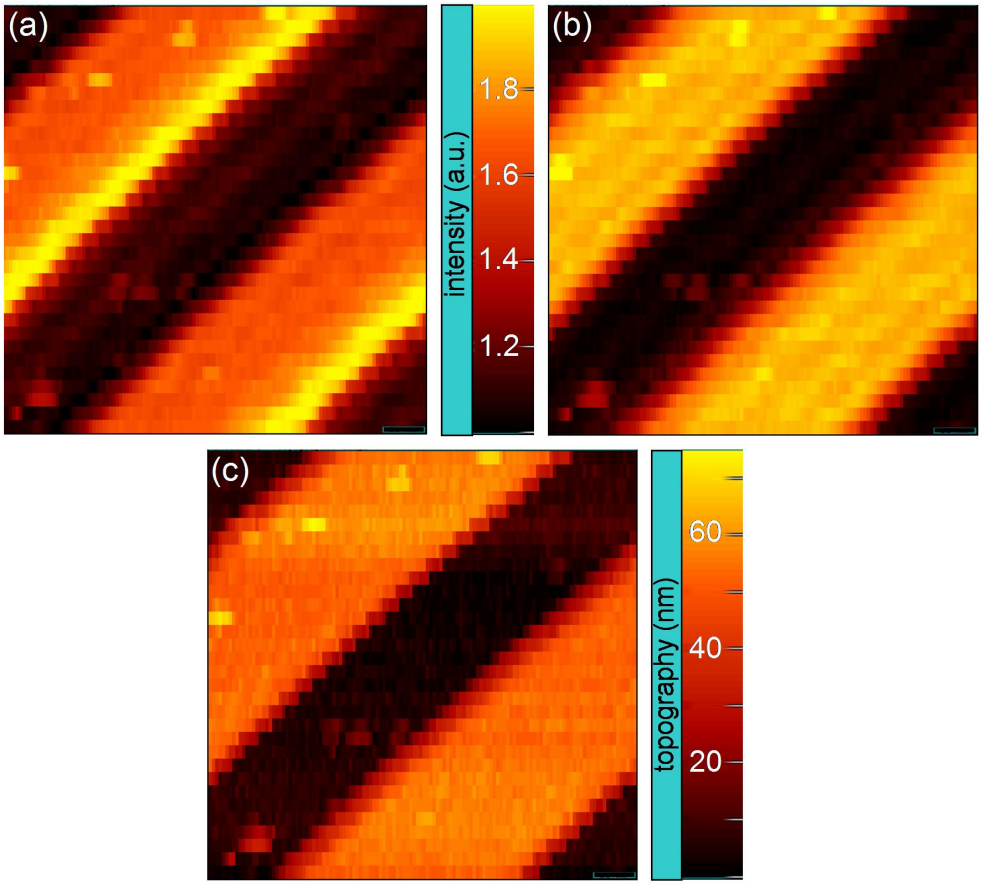

Figure 2.15. NSOM scans of 1.0 μm Au lines on GaAs. Intensity scans are made using 633 nm light with orthogonal polarizations in (a) and (b). The topography is shown in (c). The lines are about 50 nm in height.

The contrast in the NSOM scans is less than expected from the normal incidence reflectivities of Au and GaAs and differs slightly from scan to scan. One potential cause is background light that is leaked from the fiber as it backscatters from the tip. Another factor involves the geometry of collection. As discussed previously, the NSOM tip acts as a large-angle emitter which is severely shadowed by the tip. As a result, the reflectivity at large angles to the normal should be important. Relying on equations from Born and Wolf [54], the reflectivity for *s* polarized light is

$$\rho_{12}{}^2 = \frac{(n_1 \cos\theta - u_2)^2 + v_2{}^2}{(n_1 \cos\theta + u_2)^2 + v_2{}^2}. \tag{2.8}$$

Equation 2.8 uses a complex index of refraction $\hat{n} = n(1 + i\kappa)$ and

$$\begin{aligned} 2u_2{}^2 = {} & n_2{}^2(1-\kappa_2{}^2) - n_1{}^2 \sin^2\theta + \\ & \left\{\left[n_2{}^2\left(1-\kappa_2{}^2\right) - n_1{}^2 \sin^2\theta\right]^2 + 4n_2{}^4\kappa_2{}^2\right\}^{1/2}, \\ v_2 = {} & \frac{n_2{}^2\kappa_2}{u_2}. \end{aligned} \tag{2.9}$$

For *p* polarization the reflectivity is

$$\rho_{12}{}^2 = \frac{\left[n_2{}^2\left(1-\kappa_2{}^2\right)\cos\theta - n_1{}^2u_2\right]^2 + \left(2n_2{}^2\kappa_2\cos\theta - n_1v_2\right)^2}{\left[n_2{}^2\left(1-\kappa_2{}^2\right)\cos\theta + n_1{}^2u_2\right]^2 + \left(2n_2{}^2\kappa_2\cos\theta + n_1v_2\right)^2}. \tag{2.10}$$

Using the complex $\hat{n}$ of Born and Wolf and $\{n, \kappa\} = \{0.175, 18.24\}$ for Au and $\{n, \kappa\} = \{3.856, 0.0508\}$ for GaAs at 633 nm [55], the resulting *s* and *p* reflectivities are shown in Figure 2.16. Also shown are the reflectivities for unpolarized light, taken to be the average of *s* and *p* reflectivities. The ratio of

Au to GaAs reflectivities is about 2.7 at normal incidence and 1.0 at 90°. One would expect the *s* reflectivity to dominate because of the strong E_x field under the tip. The parabolic mirror collects from 45° to 90° where the s reflectivity of GaAs is rapidly rising. Assuming a uniform distribution of emitted *s* rays with incident angles from 45° to 90°, the integrated ratio of reflectivity of Au to GaAs is about 1.3. This is actually less than the 1.8 or so that is observed in the NSOM scans. However, as previously discussed, the NSOM tip emission profile is not uniform but weighted toward normal rays, and the contribution of E_z is not negligible. Furthermore, there is some light collected from the collimating lens normal to the sample. All these will contribute to increase the reflectivity ratio.

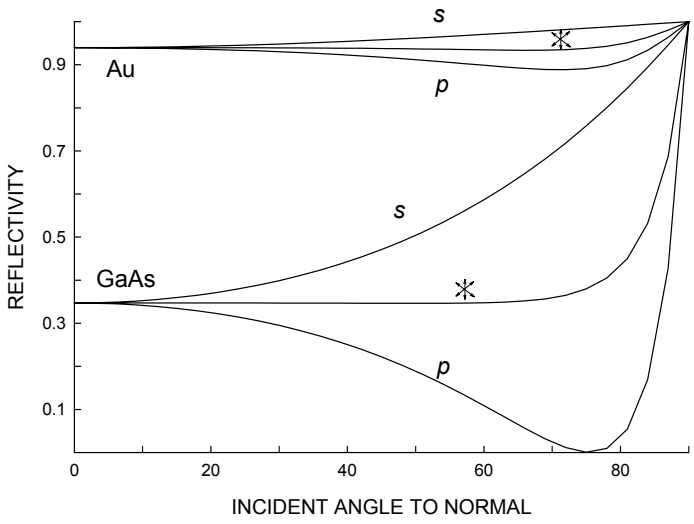

Figure 2.16. Calculated reflectivity for Au and GaAs at 633 nm for *s*, *p* and unpolarized light.

An alternative model of NSOM contrast treats the metalized tip in close proximity to the sample as an effective waveguide. Depending on the

properties of the sample, the waveguide transmission can be sensitive to E_x or E_z. Boundary conditions require continuity of the tangential electric field. As a result, all modes from E_x are cut off when the tip-sample spacing goes below $\lambda/2$ for a metal sample. Since this constraint is more severe for metal samples, their response to E_x is reduced more than it is for insulators. Conversely, the condition of tangential continuity does not apply to E_z. Surface currents act to support the tangential **H** field. Higher conductivity allows metals to transmit this mode more effectively than insulators. This picture is supported by experiments in which the polarization state of light collected from the near-field is compared to that of light collected from far-field reflection with the tip retracted [56]. The polarization state did not change from the far-field to the near-field for insulators, but it did for conductors. Converting the waveguide language to reflection language, the contrast between metal and insulator is reduced for *s* polarization and enhanced for *p* polarization.

The difference in contrast of the two scans in Figure 2.15 is most likely due to a preferred orientation in the tip-sample emission and collection. How this might work is illustrated in Figure 2.17. Also indicating a preferred detection orientation is the bright edge seen in scan (a) of Figure 2.15. Using the same polarization, scans of diagonal lines running from lower right to upper left also exhibit a bright lower left edge. This type of edge effect has been observed elsewhere using asymmetric detection with the detector on the same side of the edge in direct line with it [51]. An illustration of this result is shown in Figure 2.18.

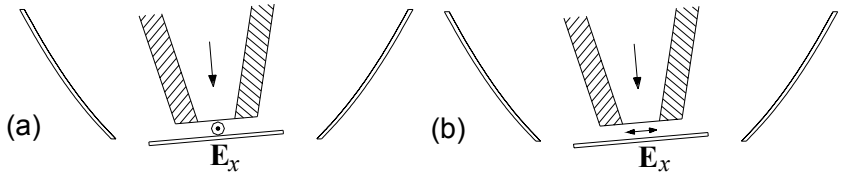

Figure 2.17. Preferred orientation of emission versus collection. In (a), the induced dipole tends to radiate to the left and to the right. The sample shadows the mirror to the right. In (b), the induced dipole tends to radiate into and out of the page where no such shadowing occurs. Since intensity from E_x is lost in (a), E_z presumably contributes more to the contrast in (a) than in (b).

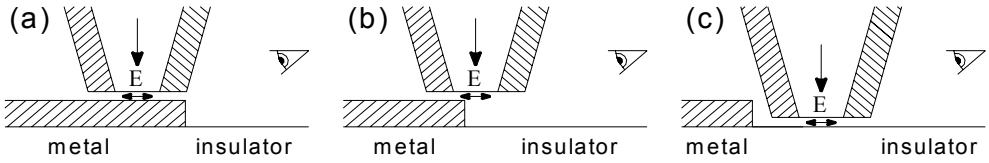

Figure 2.18. Polarization and detection scheme for bright-edge observation. The collected signal will be weak since the dipole radiates weakly in the direction of the detector, and the effect of the edge will be strong by comparison.

In summary, contrast in NSOM images does not have a one-to-one correlation to contrast in far-field imaging at near normal incidence. NSOM contrast is a function of a tip-shadowing, polarization, and collection geometry. These considerations will be of particular importance in understanding the NSOM images of the optical domains of $Nd_{½}Sr_{½}MnO_3$ in its various phases.

III. Near-field Photoluminescence of GaAs Quantum Dots

The cryogenic NSOM was used to probe accidental quantum dots (QDs) that form in narrow quantum wells (QWs) by a spectroscopic technique known as photoluminescence (PL). The sample consisted of a stack of ten GaAs QWs of varying thickness from 20 nm to 2 nm separated by 22.5 nm layers of $Al_{0.3}Ga_{0.7}As$. Only the narrowest QW was relevant for the NSOM, but the wider QWs are simpler and provide a basis for understanding the 2 nm QW. This chapter starts by explaining what PL is and how it is used to study bulk semiconductors. A model predicting the PL energies of wide QWs is then presented, and the predictions are compared to actual PL data taken on the sample. The model is finally extended to the 2 nm QW, and PL data taken on QDs by the NSOM is presented. Evidence for the presence of coupled QDs is discussed.

3.1 Introduction to Photoluminescence

3.1.1 Probing the Band Gap

PL has long been a method for probing the band gap of semiconductors. In this technique, illustrated in Figure 3.1, the semiconductor is illuminated with photons of energy above the bandgap to excite an electron-hole pair. In the simplest scenario, the electron (hole) will lose energy by phonon emission and eventually occupy the bottom (top) of the conduction (valence) band. At this point the Coulomb interaction can bind the two particles together into a hydrogen-like composite particle called an exciton. This lowers the overall

energy of the pair below the band gap energy. The exciton is short-lived as the electron and hole recombine, giving up their energy as a photon. The energy of the photon is equal to the bandgap minus the binding energy of the exciton. As will be seen in the following sections, the application of PL is not just limited to bulk semiconductors but to QWs and QDs.

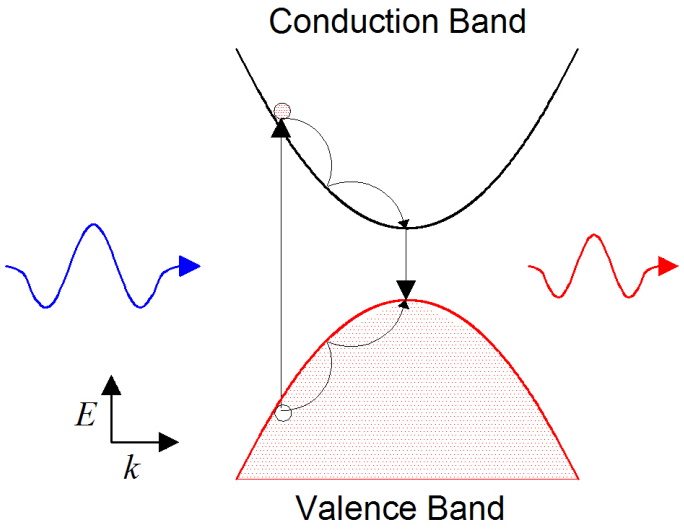

Figure 3.1. Probing the band gap with photoluminescence. An electron and a hole are generated, decay non-radiatively to the low points in the bands, form an exciton (not shown), and recombine. The energy of the emitted photon is equal to the bandgap minus the binding energy of the exciton.

3.1.2 Quantum Wells

In contrast to the formation of an exciton, which lowers the energy, confinement of an electron-hole pair in a QW raises the energy. A QW is formed when a thin layer of one semiconductor is sandwiched between layers of a different semiconductor, typically by means of molecular beam epitaxy (MBE) [57]. In such structures, the effective band gap is discontinuous at the interface. The QW is type I if the sandwiched layer has a smaller gap that

aligns inside the larger gap of the barrier material, as illustrated in Figure 3.2. The difference between the conduction (valence) band of the layers is called a "band offset," and it gives rise to a potential well responsible for the confinement of electrons (holes) in the *z*-direction. The energy of the electron-hole pair (and the resulting exciton) is raised with respect to the bandgap by an amount called the confinement energy. As the QW is made thinner, the confinement energy is increased, and the resulting PL is shifted toward the blue. Thickness fluctuations cause inhomogeneous broadening of the PL. These fluctuations occur naturally during the MBE growth of QWs and tend to be on the order of a few monolayers or less. The PL broadening increases as the width of the QW decreases.

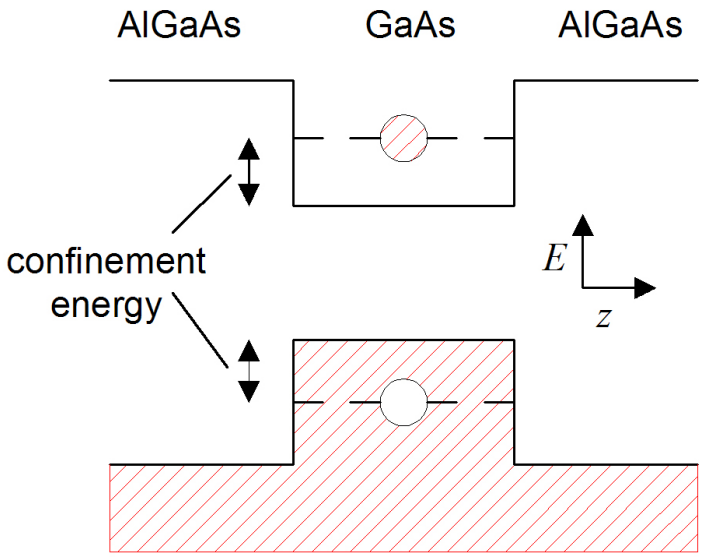

Figure 3.2. Electron-hole pair in an AlGaAs/GaAs/AlGaAs quantum well. The binding energy of the resulting exciton is not shown.

Provided that the band offsets are not small compared to the bandgap, the simple picture of a particle in a 1D box gives reasonably accurate predictions

of the PL energies observed from QWs. This is because the discontinuities in the band offsets can be controlled to be rather abrupt [57]. The simpler case of wide QWs will be considered first, and measured PL energies of the sample used in this dissertation will be compared to predicted values. E_{QW}, the PL energy of the QW is given in terms of the GaAs band gap E_G, the exciton confinement energy E_C, and the exciton binding energy E_B as

$$E_{QW} = E_G + E_C - E_B. \tag{3.1}$$

E_G is about 1519.2 meV at low temperature, and E_B is about 4.9 meV [57]. The electron and hole confinements must be calculated separately and then summed together since the band offsets are not equal. The height of the box for the electron (hole) is just the conduction (valence) band offset of the semiconductors. For $Al_xGa_{1-x}As$ the band gap at 2 K is given by $E_G(x) = 1519.4 + 1360x + 220x^2$ meV [58]. For GaAs/$Al_xGa_{1-x}As$ interfaces with $x < 0.4$, the conduction bands are responsible for 60% of the band gap difference and the valence bands only 40% [57]. The energy E of a particle in a finite square potential of height V and dimension a is well known [59] and has even solutions related by

$$a = \frac{2\hbar}{\sqrt{2mE}} \tan^{-1} \sqrt{\frac{V-E}{E}}. \tag{3.2}$$

The lowest energy of the even wavefunction solution is the ground state and is equal to the confinement energy. In GaAs the electron mass can be taken as 0.068 times m_o, the free electron mass, while the heavy hole mass must be adjusted from its bulk mass of $0.53m_o$ to $0.35m_o$ in the QW [57]. In $Al_xGa_{1-x}As$

the electron mass is given as $(0.0665+0.0835x)m_o$ and the heavy mass as $(0.48+0.063x)m_o$ [60]. The difference in mass, m in GaAs and M in $Al_xGa_{1-x}As$, will introduce a discontinuity in the wavefunction at the interface given by [57]

$$\frac{1}{M}\frac{\partial \psi_M}{\partial z} = \frac{1}{m}\frac{\partial \psi_m}{\partial z} \quad \text{at} \quad z = \pm\frac{a}{2}. \tag{3.3}$$

This adjusts equation (3.2) to

$$a = \frac{2\hbar}{\sqrt{2mE}} \tan^{-1}\sqrt{\left(\frac{m}{M}\right)\frac{V-E}{E}} \tag{3.4}$$

which can be solved iteratively for E to arrive at a known value of a. Equations (3.1) and (3.4) can be used to predict the PL energies of the GaAs QWs. For the 20 nm well, equation (3.1) predicts a PL energy of 1526.6 meV which compares favorably to 1526.4 meV as measured by Srinivas at 7 K [61]. Further modifications must be made when considering the narrowest wells.

3.1.3 Narrow Quantum Wells and 3D Confinement

By design, QWs confine the exciton in the z-direction only. Fluctuations of thickness for narrow wells lead to the additional 2D lateral confinement required to form a QD. For relatively thick QWs consisting of several hundreds monolayers, thickness fluctuations will broaden the PL slightly but will otherwise have little effect. However, for narrow QWs consisting of only a few monolayers, the effect of thickness fluctuations is large. The ground state energy of the exciton in the thicker region of the QW will be lower than it is in the rest of the well. Scanning tunneling microscopy (STM) following the

interruption of QW growth shows that 1-monolayer high islands do indeed form and tend to be elongated along the $[\bar{1}10]$ direction [14]. These islands typically have sizes from 5 to 300 nm, sufficiently small to localize excitons in the *xy*-plane, and effectively form a QD. A cartoon of a QD as monolayer fluctuation is shown in Figure 3.3.

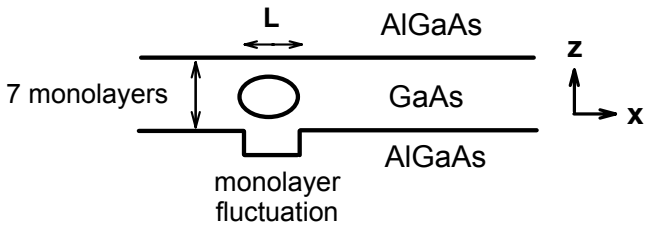

Figure 3.3. Cartoon of a QD formed by a monolayer fluctuation in a 7 monolayer thick QW.

For the sample used for the research in this dissertation, the 2 nm QW layer was closest to the surface, 27.5 nm away. This was the QW layer of interest since it was the thinnest and close enough to the surface to be measured in the near-field. Using a monolayer thickness of 0.2827 nm [57], the layer is nominally 7 monolayers thick. Band bending could become important for QWs of such small thicknesses, but it is ignored to avoid complications. Similar to the case of the 20 nm QW, the PL energy of the 2 nm QW can be calculated by equations (3.1) and (3.4) if a modified binding energy is used. Because the 3D Bohr radius of the exciton of about 11 nm [57] is significantly greater than the 2 nm well width, it is more appropriate to use the 2D exciton binding energy. In general, the 2D binding energy of a hydrogen-like system, given by $\left(E_B\right)_{2D} = \mu/8\hbar^2\varepsilon^2$, is greater than the 3D binding energy by a factor

of 4 [57], but it is also proportional to the reduced mass μ. Related to the phenomenon known as mass reversal, the heavy hole mass in the *xy*-plane decreases to $0.054m_o$ [57] which decreases the reduced exciton mass by roughly half. The resulting exciton binding energy in the 2 nm thick well is taken to be 10.4 meV. The Bohr radius, defined as $a_b{}^2 = \hbar^2/2\mu E_B$, stays about the same. Using equations (3.1) and (3.4) with the modified binding energy, the PL energy of the 2 nm well was calculated to be 1746.8 meV. Thickness fluctuations of the 7 monolayers will likely broaden the expected 1746.8 meV PL peak and provide 2D confinement energy. Similarly, the PL energies of 6 and 8 monolayers were calculated to be 1771.7 meV and 1724.6 meV, respectively. The observed energy spectrum, consistent with the calculated values, is presented in the next section along.

3.2 Near-field Photoluminescence Experiment

3.2.1 Experimental Set Up

In collection mode, laser light was focused onto the coherent fiber bundle, collected with the NSOM tip along with PL from the sample, and focused onto the entrance slit of a single-grating spectrometer. The position of the focused spot on the bundle was adjusted by trial-and-error to optimize the intensity of collected laser light. A relatively large NSOM probe diameter of 150 nm was typically used to get a relatively large throughput. The experimental scheme is illustrated in Figure 3.4.

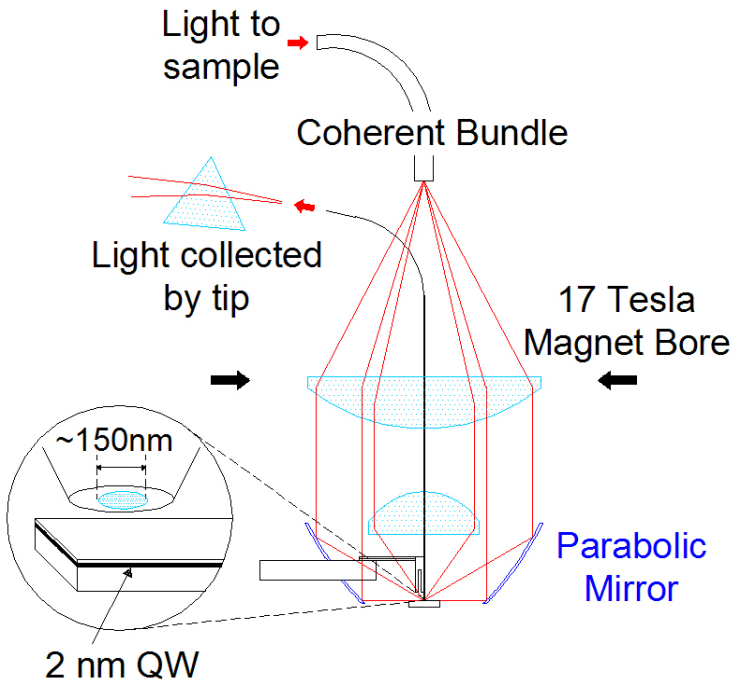

Figure 3.4. Experimental set up for near-field PL of GaAs QDs.

There are several reasons for using collection mode over illumination mode. When the NSOM tip is used to illuminate the sample, the spot formed by the parabolic mirror can be aberrant, poorly defined, and difficult to focus. Differential thermal contraction makes focusing at low temperatures more difficult still. A large portion of light from the spot is lost when focused on the entrance slit of the spectrometer. This is not the case for light emitted by the tail-end of the NSOM fiber. In either mode, the excitation power can not simply be cranked up to get more PL. In illumination mode, the large field density under an NSOM tip can over-charge the QDs and saturate the spectrum. The tip itself may be damaged by coupling more than a few milliwatts to it. In collection mode, the sample can begin to heat if more than a few milliwatts is used, and the spectral lines broaden. Considering spectral

resolution and signal alone, collection mode works at least as well as illumination mode. Furthermore, spatial resolution is an issue in illumination mode. The tip can shadow PL coming from a QD and cause the spatial scan to appear ring-like [6]. Another potential problem is exciton diffusion. Above gap excitons can be created under the tip but then diffuse to a QD some distance away. Since diffusion lengths can be on the order of a 250 nm or more [28], spatial resolution is lost. This is not a problem in collection mode since PL is collected only from excitons directly under the tip.

3.2.2 The Near-field Spectrum

A typical spectrum is shown in Figure 3.5. The humps in the spectrum presumably correspond to distributions of lateral sizes of monolayer fluctuations on backgrounds with thicknesses of 7, 6 and 5 monolayers. Clear signatures of QDs are seen as sharp lines in the low energy range of the spectrum. The energy of each line corresponds to the ground state energy of an exciton in each QD. Sufficient spatial and spectral resolution is needed to observe these lines. To demonstrate this, the average spectrum from a scan roughly 1 μm^2 in size is shown. In this average spectrum the sharp features are washed out.

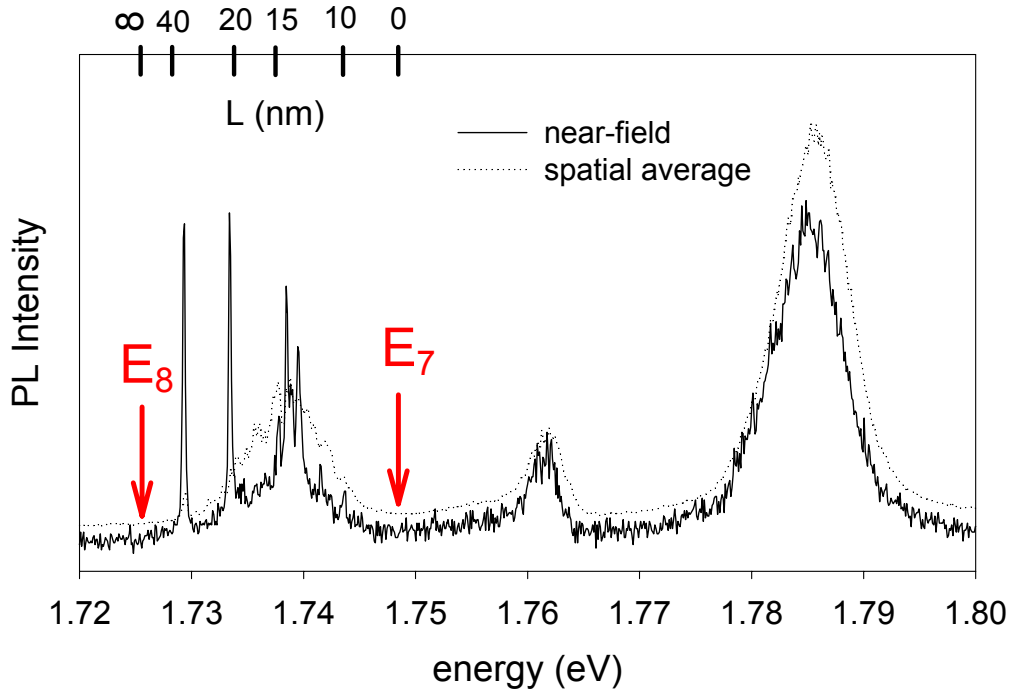

Figure 3.5. Typical PL spectrum from light collected through the NSOM tip. E_x indicates the ground-state energy of an exciton in a perfect well x monolayers thick. The lateral size of a monolayer island L is plotted to illustrate its influence on the PL energy. The dotted line shows the average of spectra over a spatial scan of roughly 1 μm^2. The excitation energy is 1.96 eV.

The dots are taken to be 8-monolayer thick islands on a background of a 7-monolayer thick QW. Excitons move freely in the well until they fall into a monolayer island where they subsequently recombine. As the lateral size of the monolayer island increases, the lateral confinement energy becomes less and the spectral signature is red shifted. An infinitely large island corresponds to a perfect 8-monolayer thick well. If the sizes of all the islands would go to zero, a perfect 7-monolayer thick well would result. Following the interpretation of Wu *et al.* [62], the energy of a perfect 7-monolayer well corresponds to a node

in the spectrum. The approximate position of the node, indicated on Figure 3.5 as E_7 = 1748.5 meV, favorably compares to 1746.7 meV, the energy previously calculated for a 7 monolayer well. The spectrum similarly goes to zero at about E_8 =1725.5 meV, predicted as 1724.6 meV for 8 monolayers. The lateral confinement energy can be estimated using a particle in a square 2D box of dimension L. Equation (3.2) relates E, the 1D confinement energy, to L with $V = E_7 - E_8$, $a = L$, and $m = 0.12\ m_o$, the exciton mass in the xy-plane. The 2D confinement energy is twice the 1D energy and is plotted versus L in Figure 3.5. The picture of an exciton in a box should be valid as long as the exciton Bohr radius of about 11 nm is smaller than the box dimensions.

Several sharp lines are typically seen at low energy within the low energy hump. There apparently are several dots in the near vicinity of the tip, and so there is a distribution of sizes and energies. Each of the dots should have excited states that contribute to the spectrum, as has been observed elsewhere [6, 63]. Unlike the ground state, excited states can pump their energy into lower energy states before they luminesce and should appear dimmer than the ground state. PL excitation (PLE) spectroscopy has shown that isolated QDs typically have four well defined excited states [14, 63]. Sometimes a QD exhibits a more continuous spectrum with some lines common with other QDs, which is attributed to potential coupling between dots [14]. In summary, the spectrum of each QD will have a bright line coming from the ground state and dimmer lines coming from excited states at higher energy. The overall spectrum will be the superposition of spectra from individual QDs. This

spectrum appears as a hump with many dim lines contributing at high energy and only a few bright lines contributing at low energy.

Compared to the low energy hump, the higher energy humps have less definition. One possibility is that band bending, insignificant for broad QWs, weakens the confinement of excitons in the thinnest parts of the QW. Most QD samples previously studied come from QWs at least 2.8 nm thick, significantly thicker than the 2 nm QW studied in this dissertation. However, even for thicker QWs, low definition in the higher energy humps has been reported [63]. Presumably, energy can be pumped from these higher energy regions to the 7-monolayer islands instead of luminescing. This will have the effect of dimming PL from large, low energy islands in the 5 and 6-monolayer regions as illustrated in Figure 3.6. This could help explain why sharp features are absent from the low energy end of the high energy humps. The middle energy hump at a width of about 18.5 meV is slightly narrower than the low energy hump. Based on the picture of inhomogeneous broadening by monolayer fluctuations, this is not expected, but it has been previously reported [14, 62, 63]. Conversely, the high energy hump at a width of over 30 meV is wider than the low energy hump and does not fit the trend. Variation of the excitation energy and intensity, as discussed in the next section, seem to suggest that the high energy hump may have a different origin than the low energy humps.

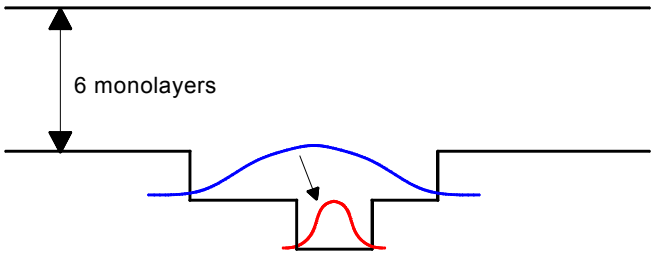

Figure 3.6. Illustration of a high energy QD transferring energy to a low energy QD.

3.2.3 Variation of Excitation

Varying the details of excitation provides some insight into the nature of the PL spectrum. These details include the intensity of excitation, the energy of excitation and the mode (collection vs. emission) of excitation.

Spectra at two different above-gap excitation intensities are shown in Figure 3.7. The higher intensity corresponds to the source maximum while the lower intensity limit is set by long integration times required for a good signal-to-noise ratio. The height of the peaks in the low energy hump roughly scales with excitation intensity. Changes in relative peak intensities could be due to *xy*-motion between tip and sample. This motion could be caused by drift or sample heating -- several Kelvin is observed at higher excitation intensity. The intensities of the higher energy humps initially scale with excitation intensity but eventually saturate and shift to the blue. This behavior has been observed elsewhere and was attributed to emission from an electron-hole plasma [64]. In this picture, the plasma initially forms in the QDs but becomes increasingly delocalized as excitation intensity increases. Low energy tails on the high energy humps could be due to the formation of biexcitons in the QDs [64].

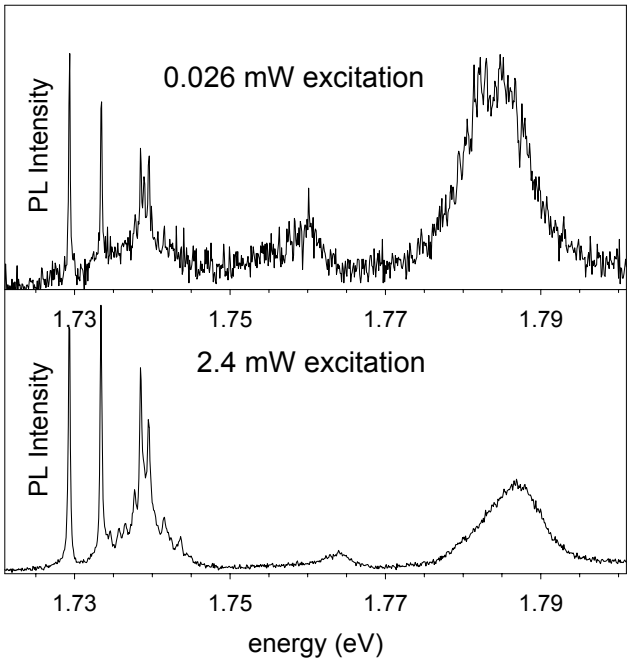

Figure 3.7. PL spectra in collection mode at two different excitation intensities. The intensity is measured before the fiber bundle. The above-band excitation energy is 1.960 eV.

It was possible to further raise the excitation intensity using below-band excitation, as shown in Figure 3.8. The excitation energy, generated with a Ti-sapphire laser, is now insufficient to create electron-hole pairs in the $Al_{0.3}Ga_{0.7}As$ layers. These layers can no longer feed the QDs, and the overall PL signal drops by about a factor of 5. The spectra show the tail of the 1.808 eV excitation line. Unfortunately, the laser became unstable at higher energies, and the tail could not be eliminated. Nevertheless, the high energy PL hump is still visible. Because the position of this hump does not change with small changes in excitation energy, it is taken to be real PL and not a laser artifact. Compared to above-band excitation, this hump is clearly suppressed relative to

the lower energy humps. However, it does not seem to saturate unlike the lower energy humps. This could be evidence that the high energy hump is related to the barrier and does not originate from PL of the QDs. At high excitation intensity, the peaks in the lower energy hump broaden and shift to the red. This could be due to local heating of the sample. Increasing temperature will have the effect of increasing scattering, reducing exciton lifetimes and thereby broadening peaks. In addition, the GaAs band gap (in eV) will decrease as the temperature T (in Kelvin) increases according to the empirical formula [65]:

$$E_{\Gamma}(T) = E_{\Gamma}(0) - \frac{5.41 \cdot 10^{-4} \cdot T^2}{(T + 204)}. \tag{3.5}$$

To achieve the 1 meV red shift observed in Figure 3.8, a temperature of 20 K would be needed. A temperature of 9.6 K is in fact measured, but the local temperature could be significantly larger. At lower excitation intensity, the positions of peaks in the low energy hump are unchanged from those of above-band excitation. Relative peak height changes could be due to *xy* tip-sample drift. The increased brightness of the middle energy hump might also be the result of tip drift over a couple of bright QDs, but it could be a resonance effect. Figure 3.9 shows the result of changing excitation energy on the spectrum.

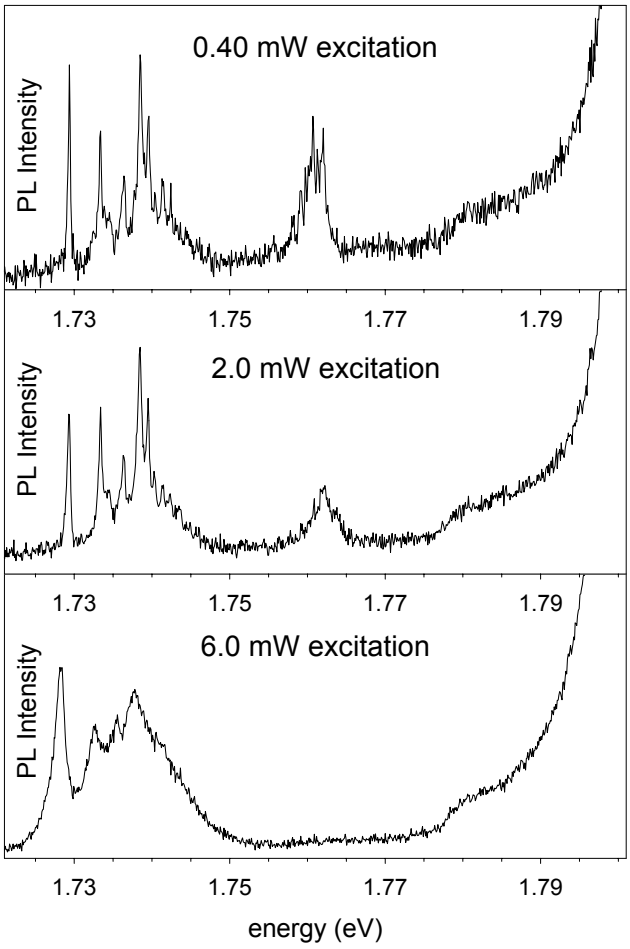

Figure 3.8. PL spectra in collection mode at three different excitation intensities. The intensity is measured before the fiber bundle. The below-band excitation energy is 1.808 eV. The tail of the excitation dominates the high energy side of the spectra.

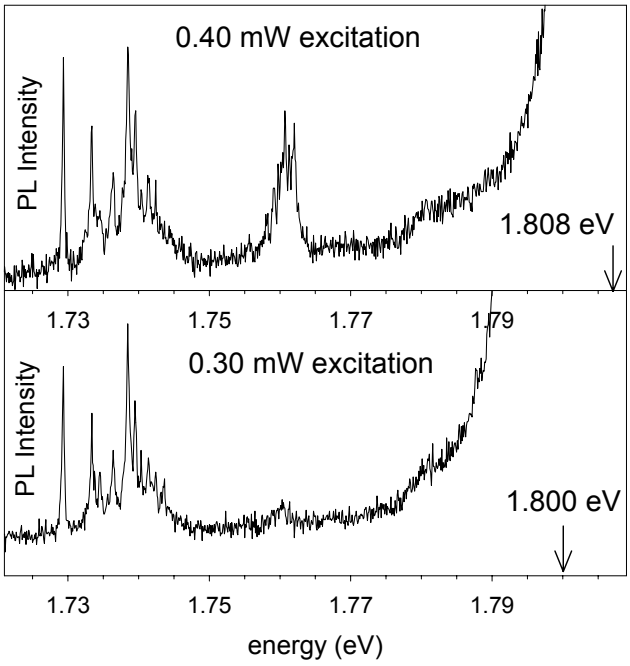

Figure 3.9. PL spectra in collection mode at excitation energies of 1.808 eV (top) and 1.800 eV (bottom).

The relative heights of the three spectral humps depend not just on excitation energy and intensity, but also on the mode of PL excitation/collection. In collection mode, PL is only collected from the recombination of electron-hole pairs below the tip. In emission mode, carriers created under the tip can diffuse and recombine somewhere else in the sample. Spectra taken in emission mode are shown in Figure 3.10. Because of diffusion, the number of excited QDs is increased, and peaks from individual dots can rarely be picked out. As the power coupled to the tip increases, the spectrum begins to saturate, and all definition in the low energy hump is washed out.

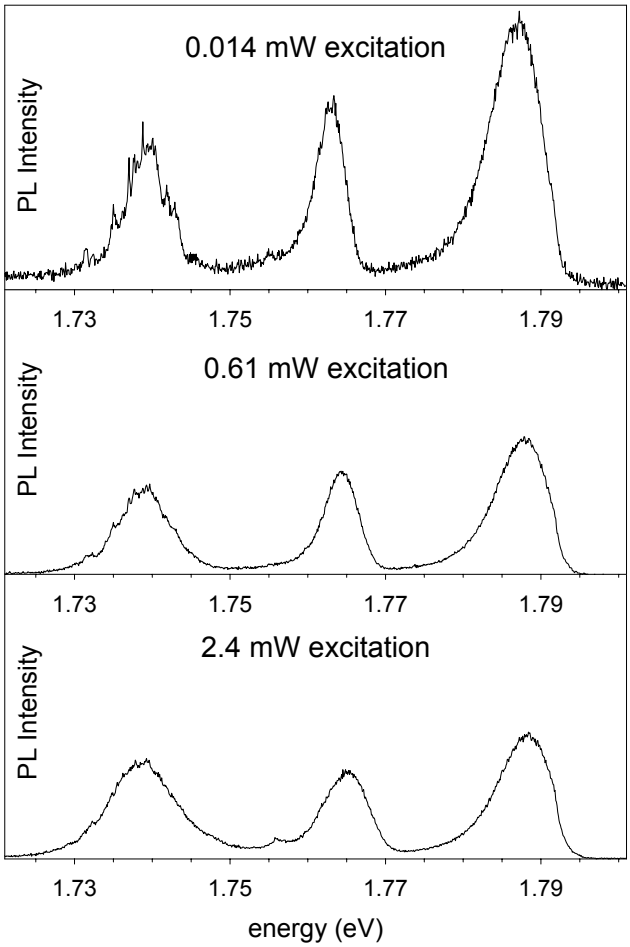

Figure 3.10. PL spectra in emission mode at three different excitation intensities. The intensity is measured before being coupled to the NSOM fiber. The above-band excitation energy is 1.960 eV

3.2.4 Spatial Scans

NSOM images of individual QDs can be generated by measuring its PL peak intensity as the tip is scanned across the sample. Since individual QDs are expected to be much smaller than the NSOM tip size, the dot is effectively imaging the tip. However, this is only true in collection mode. NSOM scans in emission mode are a measure the diffusion pattern of the created excitons as

they fall into the QD. Typical scans of a spectral peak taken in emission mode and collection mode are shown in Figure 3.11.

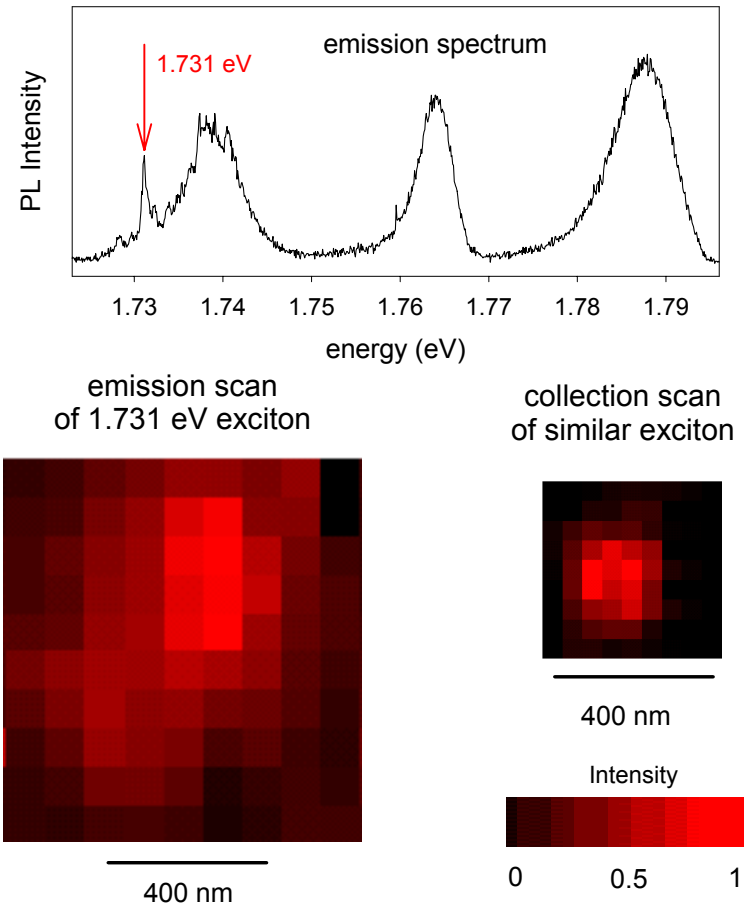

Figure 3.11. Near-field spectrum in emission mode (top) and NSOM scans of the spectral peak (bottom left) and of a similar peak in collection.

Because a spectrum is taken at each location of the tip, simultaneous imaging of many QDs is possible. The usual 3D scan information of *xy*-position and intensity is transformed into a 4D hyperscan including energy. Scans of two spectral peaks in collection mode are shown in Figure 3.12.

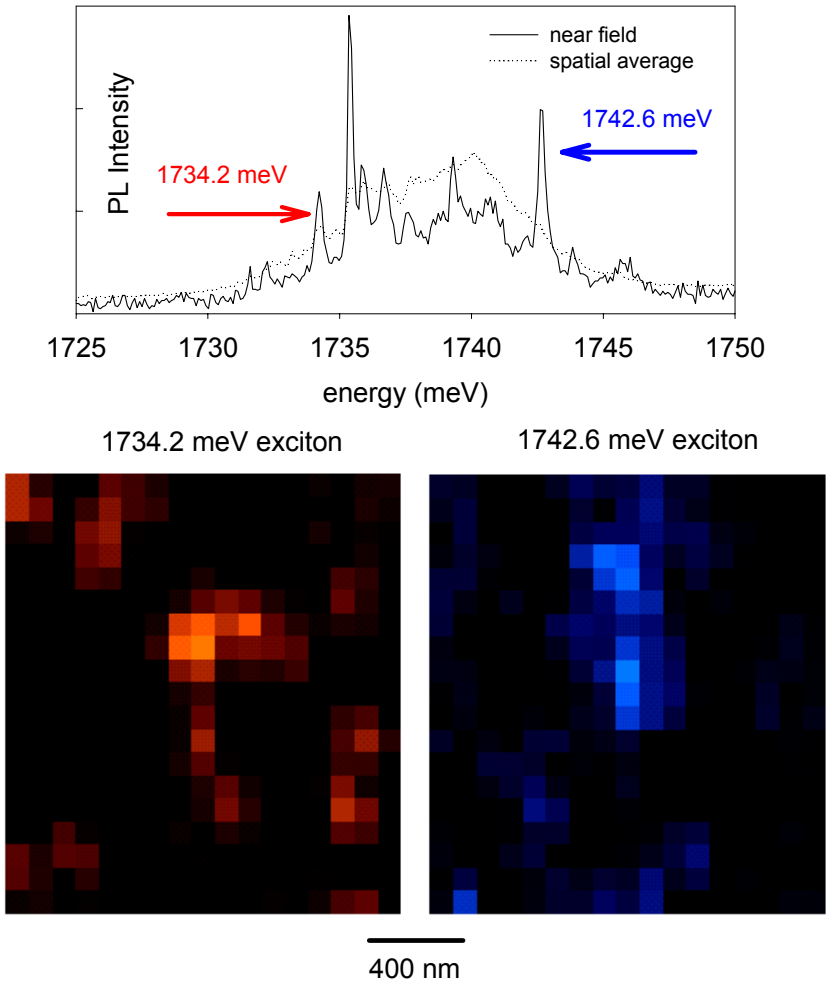

Figure 3.12. Near-field spectrum in collection mode (top) and NSOM scans of two spectral peaks (bottom).

Similar simultaneously acquired scans are shown in Figure 3.13. The QDs can appear de-localized due to the inhomogeneous broad background. Perhaps the result of chance, QDs of a similar energy emanate from sources that are close together in space. Both of these difficulties can be overcome by searching out QDs with very low energies, far in the left wing of the inhomogeneous distribution. Such a QD observed in a separate scan is presented in the next section.

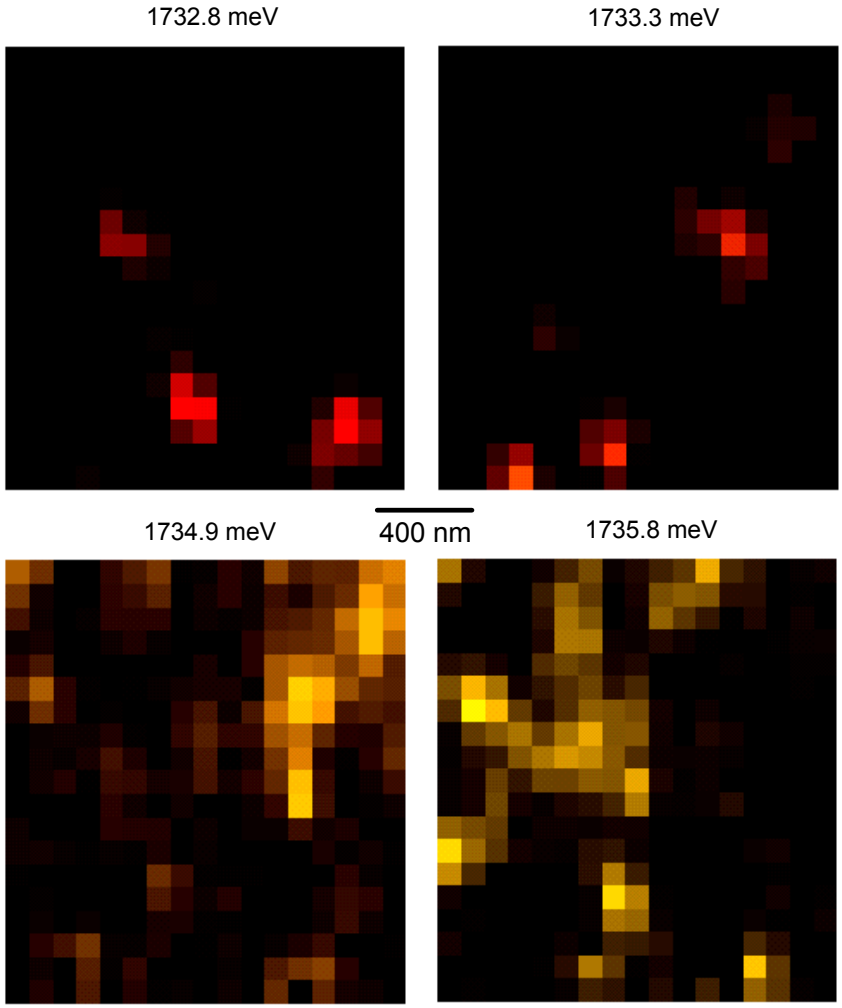

Figure 3.13. NSOM scans at 4 different energies. The plotted intensities are the integration of the spectrum over a 0.40 meV interval.

3.3 Coupled Dots

3.3.1 Low Energy Pair Coincidence

In one particular scan, a very low energy peak is observed at two separate spatial locations. The scan is presented in Figure 3.14. The peak's energy position in the far left of the low energy hump makes its presence a rare event. Despite this, the peak reoccurs close together in space in the same scan. The

probability that this observation is pure coincidence seems remote. A rough estimate of the number of expected peaks of a particular energy in a scan of a particular size can be made. From a total of N dots following an energy distribution $P(E)$, the number of dots $n(E_o)$ with an energy E_o in a range of ΔE will be given by $n(E_o) = NP(E_o)\,\Delta E$. N should be set to the number of QDs lying within a circle with a diameter of 300 nm, the separation between the rare dots. N is estimated as 40 since roughly 10 peaks are seen under the 150 nm NSOM tip at any particular position. The actual number of dots may be somewhat less, but it is better to err on the side of caution. $P(E)$ is estimated with a Gaussian

$$P(E)\,dE = \frac{e^{-\left(E-\bar{E}\right)^2/2\sigma^2}}{\sigma\sqrt{2\pi}}\,dE, \tag{3.6}$$

where $\bar{E}$ is roughly 1738 meV and σ is about 5.8 meV. Finally, ΔE is set to the spectral resolution of about 200 μeV, yielding n(1729.3 meV) $\approx$ 0.2 dots. Since this number is much less than one, a more likely explanation is that the double peak is produced by QDs that are not independent but coupled. Various mechanisms have been considered to explain potential QD coupling. They include exciton tunneling, dipole-dipole interaction, and shape fluctuations of the monolayer islands.

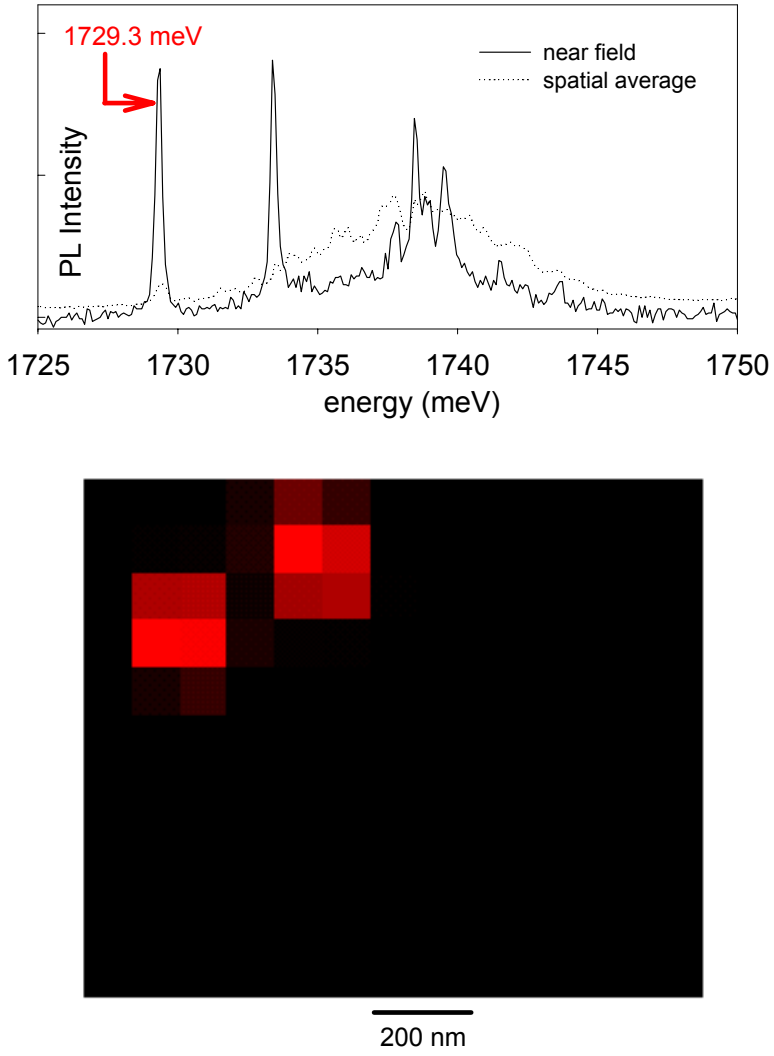

Figure 3.14. Near-field spectrum featuring a peak at 1729.3 meV and the NSOM scan of the peak.

Exciton tunneling can potentially couple otherwise isolated QDs having different ground state energies and independent wavefunctions. The isolated ground state wavefunction with the lower energy corresponds to the ground state wavefunction of the coupled system. In the coupled system, the ground state wavefunction is even with non-zero amplitude in both QDs. The strength of the coupling is given by the tunneling rate and gives an indication of the

wavefunction amplitude in the higher energy QD. The rate of exciton tunneling from one QD to another can be estimated using the Wentzel-Kramers-Brillouin (WKB) approximation to calculate the tunneling amplitude. This approach is used in quantum mechanics texts to estimate alpha particle decay rates. In this picture, the exciton moves with speed $v = \sqrt{2E/m}$ and bangs into the wall of the QD of lateral size *a* with frequency $f = v/2a$. Upon collision, the exciton has a probability of escape to an adjacent QD a distance *r* away given by $e^{-\gamma}$, </YEAR> is given by $\gamma = \left(2r/\hbar\right)\sqrt{2m\left(V-E\right)}$. The mean tunneling time is $\tau = \left(1/f\right)e^{\gamma}$ or

$$\tau \approx \frac{2a}{\sqrt{2E/m}} \exp\left(\frac{2r}{\hbar}\sqrt{2m\left(V-E\right)}\right). \tag{3.7}$$

Following the model of an exciton in a 2D box for the QDs in question, $V = 23$ meV, $E \approx 3.8$ meV, $a \approx 32$ nm, $m = 0.12\ m_o$, and $r \approx 300$ nm. The resulting tunneling time is on the order of 10^{52} seconds, which is longer than the age of the universe.

By another mechanism the exciton in one QD could tunnel into an adjacent QD by decaying into a photon and then reappearing in the second QD as an exciton. This type of energy transfer between molecules, atoms or ions is called the Förster process [66] and has been applied to excitation of electron-hole pairs in semiconductors [67] and exciton coupling in QWs [68]. Applied to exciton excitation in adjacent QDs, one would expect the solid angle for absorption to be too small compared to 4π to be significant. However, if the

two energies happen to be resonant, this process could have a large cross section.

Dipole-dipole interaction would require excitons to inhabit both of the adjacent QDs. Since it is a two particle process, one would expect peak intensity to vary non-linearly with excitation intensity. As discussed in 3.2.3, this does not seem to be the case, but it can not be ruled out completely. In the picture of interacting dipoles, fluctuations of charge distributions in excitons in adjacent QDs could give rise to a net dipole moment, as occurs between nearby gas atoms. The energy E_{dd} associated with the coupling of induced dipoles of magnitude p is $E_{dd} \approx \alpha p^2 / \varepsilon^2 r^6$ where α is the polarizability of the exciton and r is the separation between excitons [69]. Using the rough estimates $\alpha \approx 4\pi\varepsilon a_b^3$ [70], $p \sim e a_b$ where a_b is the exciton Bohr radius, and r = 300 nm,

$$E_{dd} \sim \frac{4\pi}{\varepsilon a}\left(\frac{a}{r}\right)^6 \sim 10^{-6} \text{ meV}. \tag{3.8}$$

This is clearly too small to be relevant.

The mechanism that seems best able to explain QD coupling involves the shape of the monolayer island that forms the QD. As previously mentioned, STM has revealed that monolayer islands tend to be elongated along the $[\bar{1}10]$ axis. These islands have lengths frequently over 100 nm, aspect ratios from 2 to 10, and widths that vary along the lengths [14]. As will be shown shortly, a slight narrowing of the width can produce an effective potential barrier and a node in the wavefunction. Such an island might look somewhat like a dumbbell.

3.3.2 The Dumbbell Potential

The wavefunction of a particle in an infinitely deep 2D box has the separable form $\Psi(x,y) = \Psi_x(x)\Psi_y(y)$. Both lateral dimensions, L_x and L_y, confine the wavefunction and contribute to the energy as

$$E(n_x, n_y) = \frac{\hbar^2 \pi^2}{2m}\left(\frac{{n_x}^2}{{L_x}^2} + \frac{{n_y}^2}{{L_y}^2}\right). \tag{3.9}$$

For the lowest energy states in the case that $L_x >> L_y$, only $n_y = 1$ need be considered. If L_y is allowed to have a slight variation ΔL_y as a function of x, then the energy should be altered by

$$\Delta E = \frac{\pi^2 \hbar^2}{2m{L_y}^2}\left(-\frac{2\Delta L_y(x)}{L_y}\right) \equiv V_{bar}. \tag{3.10}$$

Ψ_y is squeezed in the narrowed region, raising its contribution to the energy and effectively producing a potential barrier to Ψ_x. The effective potential becomes

$$V_{eff}(x) = V(x) + V_{bar}(x), \tag{3.11}$$

where $V(x)$ is the original square well potential. If sufficiently large, the barrier could produce a minimum in the barrier region for the ground state Ψ_x. A simplified dumbbell shape is presented in Figure 3.15.

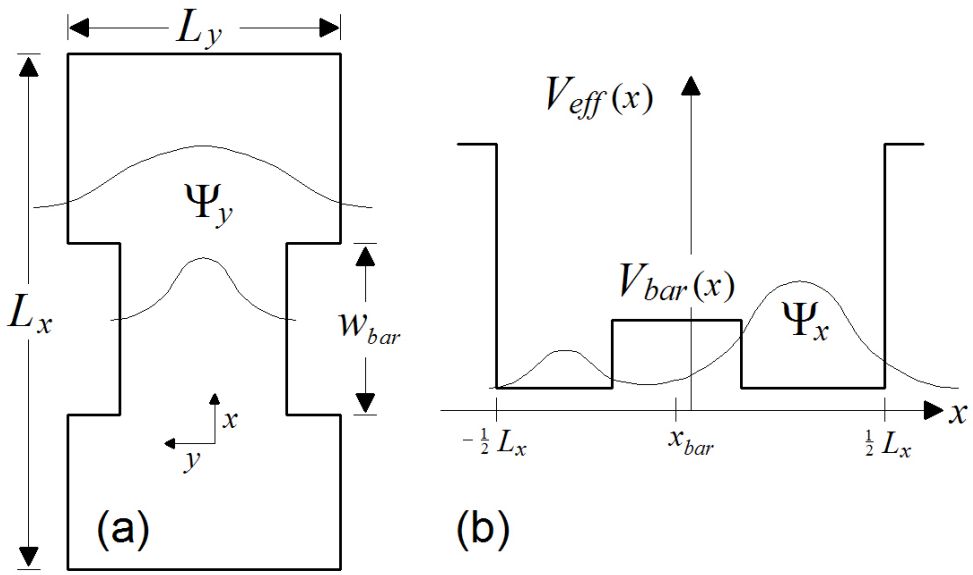

Figure 3.15. The dumbbell potential. The narrowing of the dumbbell-shaped monolayer island shown in (a) confines Ψ_y and produces an effective potential for Ψ_x shown in (b).

The model of the dumbbell potential is readily applied to the low energy double dots. Estimations of the various parameters are necessarily somewhat speculative, and so the results are intended to be illustrative. The coincident PL peaks are separated by about 300 nm in space. Since the maximum amplitude of the wavefunction will not be at the monolayer wall, L_x is estimated to be about 400 nm. Since the island is assumed to have a large aspect ratio, the x-contribution to the confinement energy should be small compared to that of y. The confinement energy was previously estimated to be about 3.8 meV, and the y-contribution is taken to be about 3.5 meV. For this energy, equation (3.9) for an infinite square well yields $L_y \approx 30$ nm. This compares to about 22 nm predicted by equation 3.2 for a finite square well. Equation (3.10) predicts V_{bar} to range from about 0.7 meV to 2.0 meV for the

rather modest 10% to 30% variation in L_y. The position x_{bar} and width w_{bar} of V_{bar} are free parameters in the model. The position is chosen slightly off center $(x_{bar} \neq 0)$, such that one end of the dumbbell is longer than the other in the x-direction by about 10% to avoid degeneracy and to be more realistic. For the initial calculation, the w_{bar} is set to about one third of L_x. For ease in computation, the potential walls at either end of L_x are set to infinity rather than 23 meV. As long as the wavefunction energies are well below 23 meV, this approximation should be valid. Using the Schrödinger equation with the necessary boundary conditions, the lowest 4 energies are calculated along with their wavefunctions. The results are shown in Figure 3.16 for V_{bar} values of 0.5 meV and 2.0 meV.

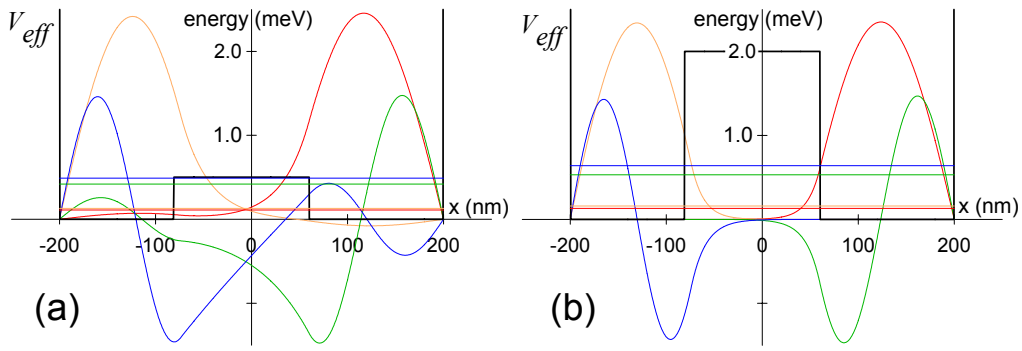

Figure 3.16. Calculated energies (horizontal lines) and wavefunctions for V_{bar} = 0.5 meV (a) and 2.0 meV (b). To avoid degeneracy, V_{bar} is slightly off center at x_{bar} = -7 nm. w_{bar} = 134 nm.

It is interesting to note that even a slight amount of narrowing causes the ground state and first excited state wavefunctions to collapse on opposite sides of the barrier. These states typically differ in energy by about 20 μeV, too small to be differentiated by the spectrometer. This energy difference increases

to about 45 μeV when V_{bar} is offset such that one end of the dumbbell is twice as long as the other. The overlap of the ground state and first excited state wavefunctions is relatively small, even for the 0.5 meV barrier. Narrowing w_{bar} will increase the amount of overlap as shown in Figure 3.17. In any case, as the energy of the excited states increases, the excited state wavefunctions will have increased overlap with the ground state and first excited state wavefunctions. In other words, the two lowest energy states may not be directly coupled, but they should be coupled indirectly through the excited states.

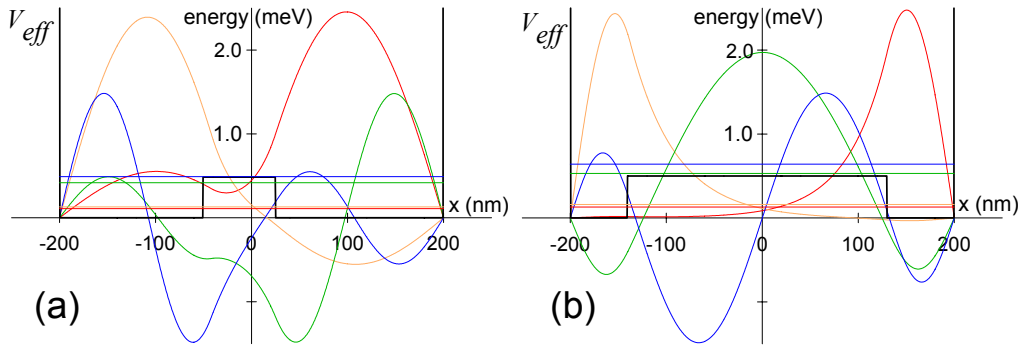

Figure 3.17. Calculated energies (horizontal lines) and wavefunctions for V_{bar} = 0.5 meV with varying widths. Compared to Figure 3.16 (a) where w_{bar} = 134 nm, the barrier width is about half as much in (a) and twice as much in (b). To avoid degeneracy, V_{bar} is slightly off center at x_{bar} = -7 nm.

In a long, dumbbell-shaped QD, the number of excited states can be very large, and the spacing close together. As previously mentioned, quasi-continuous excited states have been reported [14]. A long QD should have a large number of states available for exciton capture and a large capture area, proportional to length. Provided that there is no anomalous drop in phonon scattering cross-section, the PL from long QDs should be relatively bright.

This seems to be the case with the double dots. Considering the STM scans alone, it would seem surprising if long, bright dots with apparent coupling and quasi-continuous excited states did not exist.

To confirm the picture of the coincident QDs as dumbbell shaped, it would be useful to probe the excited states by performing photoluminescence excitation (PLE) on candidate coupled QDs. In PLE, the PL intensity of a particular excitonic peak is measured as a function of the energy of excitation. When the excitation energy is in resonance with an excited state, the PL peak intensity increases dramatically. Combined with NSOM, excited state wavefunctions could be imaged. Unfortunately, it has not been possible to do this experiment to this date. The chief problem is insufficient PL signal due to various causes. PLE requires below-band excitation, typically from a laser, close in energy to the PL peak being studied. Spectrometers designed to filter out the laser excitation need more optical surfaces and are therefore less efficient than simple spectrometers. The signal is small to start with since below-band excitation produces less PL intensity than above-band excitation. Presumably there are fewer states to pump into. Using an excitation within the low energy hump of the near-field spectrum, some PL peaks disappear completely. PLE spectroscopy attempts to pump into a single excited state, but collection mode NSOM benefits from diffusion of carriers from the large illumination spot to the area under the tip. A possible solution to the signal problem could involve using higher throughput tips fabricated by chemical etching. QDs have recently been imaged with such tips [7, 71].

IV. Imaging of the Manganite $Nd_{½}Sr_{½}MnO_3$

In this chapter, the near-field and far-field imaging of the various electronic phases of $Nd_{½}Sr_{½}MnO_3$ as it undergoes phase transitions is described. $Nd_{½}Sr_{½}MnO_3$ has a low temperature phase consisting of a charge-ordered insulator (COI), a transition to a ferromagnetic metal (FMM) at about 160 K, and a transition to a paramagnetic insulator (PM) at about 250 K. Regions with polarization-dependent contrast, termed here as optical domains, are observed in all three phases. The chapter begins with a description of the phases, crystallography, characterization, and preparation of the sample. Far-field images of the FMM, PM, and COI phases in that order are presented and discussed. The COI to FMM and FMM to COI transitions are also investigated. Finally, NSOM imaging of the FMM, PM, and COI phases and the COI to FMM transition is presented and discussed.

4.1 Background on $Nd_{½}Sr_{½}MnO_3$

4.1.1 Electronic Phases and Crystallography

The most up-to-date phase diagram of $Nd_{1-x}Sr_xMnO_3$ has been published by R. Kajimoto *et al.* [72]. From the phase diagram of M. Uehara *et al.*[73] for $La_{1-x}Ca_xMnO_3$, it can be inferred that $Nd_{1-x}Sr_xMnO_3$ should have a transition from an orthorhombic structure to a rhomohedral phase well above room temperature. A merger of the phase diagrams of both groups is presented in Figure 4.1. It shows that only in the vicinity of $x = ½$ does the true COI state reside as the low temperature phase. The presence of the charge-ordered state

is revealed by neutron scattering experiments [72], and it is accompanied by antiferromagnetic spin order and orbital order as shown in Figure 4.2. Also for x = ½, the phase diagram shows a transition to a FMM phase at a temperature of about 160 K and a transition to a PM phase at a temperature of about 250 K.

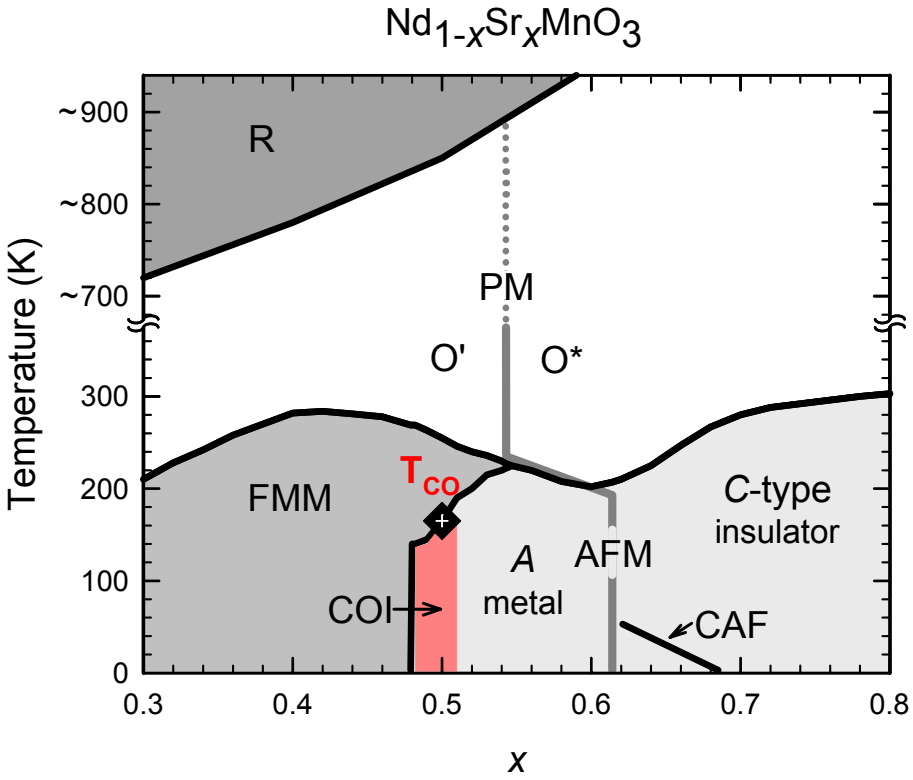

Figure 4.1. Phase diagram of $Nd_{1-x}Sr_xMnO_3$ adapted from R. Kajimoto *et al*. [72] and M. Uehara *et al.* [73]. Different phases are denoted by capital letters as follows; PM = paramagnetic insulator, FMM = ferromagnetic metal, AFM = antiferromagnetic, COI = charge-ordered insulator with *CE*-type charge and spin order, A = *A*-type antiferromagnetic order, C = *C*-type antiferromagnetic order, CAF = possible canted antiferromagnetic order. O' (O^*) indicates that the MnO_6 octahedra is compressed (elongated) along the *c*-axis. T_{CO} is the transition temperature between COI and FMM for x = ½.

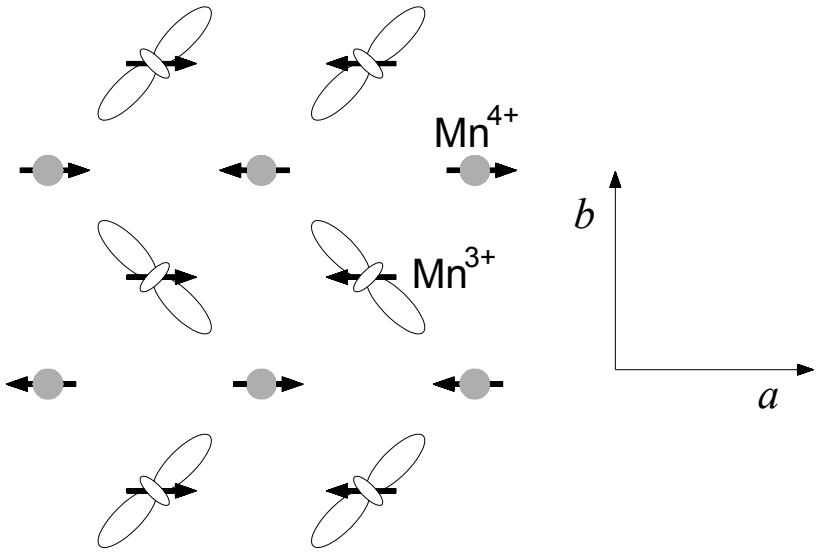

Figure 4.2. Schematic of the ordering of the charge, spin, and e_g orbitals in the COI phase. Black arrows represent spin. The d $(3x^2–r^2)$ and d $(3y^2–r^2)$ orbitals of Mn^{3+} are perpendicular to each other in the ab plane.

The crystal structure of $Nd_{1-x}Sr_xMnO_3$ can be understood as a distorted perovskite crystal. The octahedra formed by Mn ions surrounded by six O ions is apically compressed and tilted relative to the crystallographic axes. Figure 4.3 shows two possible tilt orientations with their associated symmetry groups of *Pbnm* and *Ibmm*. Because of its lower symmetry, the *Pbnm* structure should produce additional Bragg reflections in neutron scattering at small angles. Since R. Kajimoto *et al.* did not observe such reflections in the PM phase [72], they assign it to *Pbnm*. However, they were unable to definitively discriminate between *Pbnm* and *Ibmm* for the COI phase due to potential overlap of the *Pbnm* Bragg peaks with the COI superlattice peak. Due to the distortions, the resulting $Nd_{1-x}Sr_xMnO_3$ lattice is only pseudocubic with an orthorhombic unit

cell of dimensions ≈ $\{\sqrt{2},\ \sqrt{2},\ 2\}$ times the cubic cell dimension. In the COI phase, orbital ordering doubles the unit cell along *b*, but R. Kajimoto *et al.* omit this from their analysis [72]. They find $a \gtrsim b \gtrsim c/\sqrt{2} \approx 5.4$ Å for the COI, FMM and PM phases at $x \simeq ½$. For the FMM and PM phases, $c/\sqrt{2}$ and *b* differ from *a* by roughly 1.5% and 0.8%, respectively. For the COI phase at about 10 K, these differences increase to roughly 3.5% and 1.2%, respectively. Similarly, the difference of Mn-O bond lengths along *c* and within the *ab* plane increases from about 0.5% in the FMM and PM phases to about 1.1% in the COI phase.

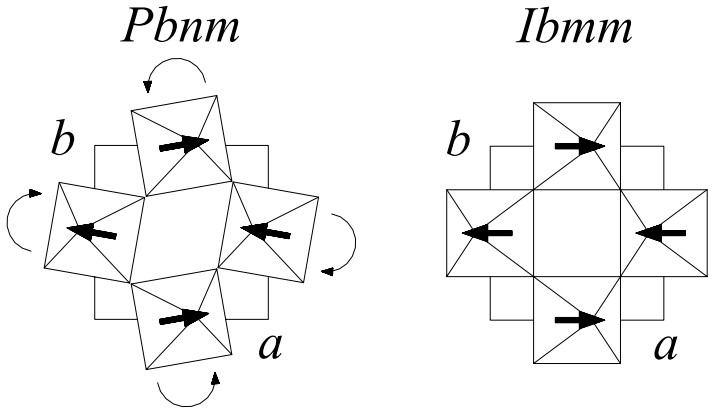

Figure 4.3. Schematic of the possible tilts of the MnO_6 octahedra with their associated symmetry designations according to R. Kajimoto *et al.* [72].

4.1.2 Optical Anisotropy

Of critical importance to the work presented in this dissertation is the fact that the Mn-O bonds in the *ab* plane are longer than those along the *c* axis. Presumably, there are also differences of these bond lengths within the *ab* plane. As a result, the optical response for light polarized along each of the

orthogonal crystal axes should be different. In principle, this optical anisotropy can be exploited to observe domains of differing axis orientation within each electronic phase. These domains will be referred to as optical domains in this dissertation to distinguish them from ferromagnetic domains or domains of different electronic phase. As pointed out in the previous section, the difference of Mn-O bond lengths along the *c* axis and in the *ab* plane is about twice as large in the COI phase compared to the FMM or PM phases. As a result, contrast between optical domains in the COI phase should be greater than it is in the FMM or PM phases.

Optical domains in metals have long been studied by polarization microscopy. The general technique of optical microscopy has been employed for some time to investigate many aspects of the microstructure of metals [74]. Included among these aspects is the formation of martensitic steel. This has particular relevance to the study of $Nd_{½}Sr_{½}MnO_3$ and is discussed in the next section.

4.1.3 Martensitic-like Character

Martensitic transformation in steel and other metals has been studied extensively [75], and it has been recently suggested to be relevant to the understanding of phase transitions in the manganites [76]. Originally attributed to only carbon steels, a martensitic transition has come to mean any phase transformation that occurs by cooperative atomic movements according to three essential characteristics: there is no diffusion of atoms, there is surface

upheaval producing surface relief, and there is generation of a large number of lattice imperfections such as stacking faults and internal twinning. As suggested by this characterization, accommodation strain plays an important role in the formation of the martensite. Martensitic transformations have been described as "military" to reflect the orderly fashion in which they occur and as domino-like since atoms move one after another in succession. Optical microscopy often has sufficient resolution to view lattice imperfections, while smaller features can be imaged with transmission electron microscopy (TEM). Typically, martensitic transitions are very fast, on the order of 10^{-7} sec for steel, but they are sometimes slow enough to follow with an optical microscope.

The optical micrograph of Figure 4.4 [77] shows many of the characteristics of a martensitic transformation. The bright regions coincide with the parent or austenite phase of the steel crystal. The regions labeled as "*A*" and "*B*" are different *variants* or crystal orientations of the martensite phase. For Fe-Ni alloys the possible variant orientations were first worked out by Nishiyama [75]. Accordingly, the following relations bear his name;

$$(111)_\gamma \,||\, (001)_{\alpha'}, \quad \left[\bar{1}\,\bar{1}2\right]_\gamma \,||\, \left[0\,\bar{1}1\right]_{\alpha'} \tag{4.1}$$

In the Nishiyama relations, γ represents the austenite and α' the martensite. The $(111)_\gamma$ plane of parallelism can be one of the four planes (111), $(\bar{1}11)$, $(1\,\bar{1}1)$, or $(11\,\bar{1})$. For each one of these planes three different directions can be chosen, implying $4 \times 3 = 12$ different variant orientations. In Figure 4.4,

variant *A* forms first, and *B* forms later. As *B* penetrates *A*, is deforms it at the crossing point. The striations within *B* are taken to be twins. This particular transition is never quite complete, and the austenite remains even down to a few Kelvin.

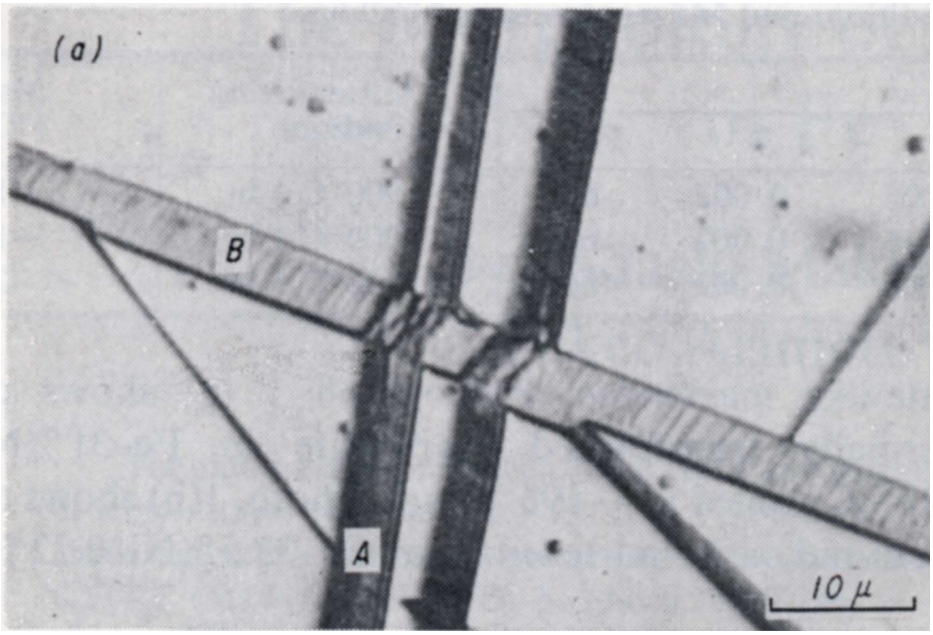

Figure 4.4. Optical micrograph of thermally transformed martensitic variants in Fe-31%Ni-0.28%C steel from Maki *et al*. [77].

4.1.4 Sample Characterization and Preparation

To this point, generic background information on $Nd_{½}Sr_{½}MnO_3$ has been discussed. Now the particular sample studied in this dissertation is treated. The sample was provided by Moritomo's group at Nagayo University in Japan. It was grown as a single crystal by the floating zone method [78]. Though no transport measurements have been made on the particular sample used in this dissertation, Moritomo's group has shown the dc resistivity of similarly prepared samples to be discontinuous near the FMM to COI transition [79].

Magnetic susceptibility measurements on the sample were made by Satish Ogale at the University of Maryland. The results are presented in Figure 4.5. The FMM phase is clearly present in the resulting curve. The transition shows hysteresis, a signature of a first order transition.

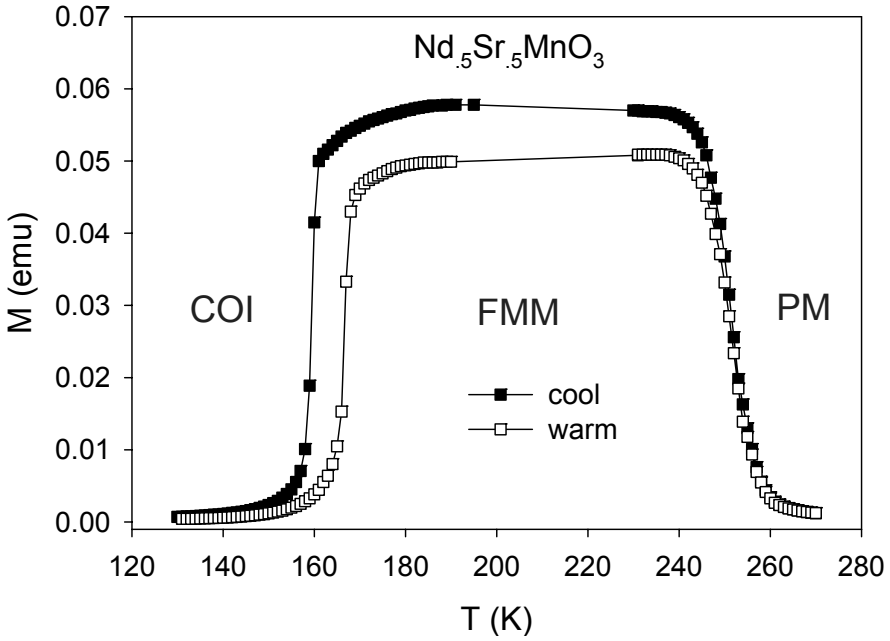

Figure 4.5. Magnetic susceptibility of the $Nd_{½}Sr_{½}MnO_3$ sample. The poling field used is 0.2 Oe.

The sample was originally polished and annealed in an O_2 atmosphere at 1000° C for Raman studies [80]. This annealing recipe for this class of samples was developed to remove surface damage due to polishing in order to make reliable optical measurements [81]. However, initial NSOM scans of the sample showed surface roughness and associated topographical artifacts in the collected light signal that would likely mask the observation of optical domains. The sample was re-polished with a 9.8 pH, 0.05 μm silica suspension. Its surface was probed using optical microscopy and atomic force

microscopy (AFM). The surface became locally smooth but faceted, as shown in Figure 4.6(a). The faceting was presumably due to differential polishing rates along different crystal axes. The sample was also annealed by the aforementioned recipe. During annealing the sample was driven into the rhombohedral phase. The annealing results in a smoother surface as shown by the AFM images in Figure 4.6(b) and (c). A limited sampling of the surface by optical microscopy and AFM suggests an increased density and complexity of faceting, presumably due to the sample's passage into and out of the rhomohedral phase during annealing. Some of the topography from the polishing/annealing process is "frozen-in" in the sense that it persists even as the surface undergoes upheaval during the FMM-COI phase transitions. These frozen-in features sometimes appear in optical micrographs and NSOM scans and are not associated with optical domains.

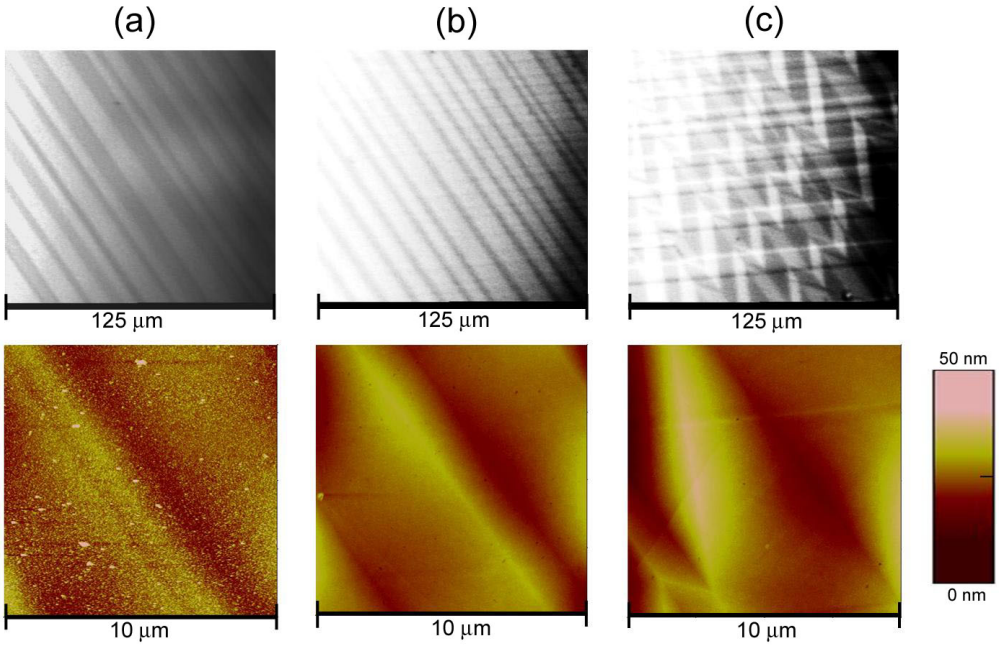

Figure 4.6. Optical micrographs (top) of the $Nd_{½}Sr_{½}MnO_3$ sample, each paired with a corresponding AFM scan (bottom). The images were taken directly after polishing (a) and after annealing (b) and (c).

The reflectance of the $Nd_{½}Sr_{½}MnO_3$ sample as a function of wavelength at different temperatures was measured by Andrei Souchkov at the University of Maryland. The shapes of the resulting plots, shown in Figure 4.7, have features indicative of the electronic phase of the sample. The reflectance of the COI phase is relatively flat with a slight downward slope. Indicative of an insulator with an onset of inter-band transitions, the magnitude of the slope increases in the visible. There is only slight variation in the plot shape as temperature is raised from 11 K to 150 K in the COI phase. Reflecting the first order nature of the transition, the change in plot shape from the COI phase at 150 K to the FMM phase at 180 K is abrupt. Suggestive of a *d-d* hopping transition in the COI phase changing to conduction of delocalized electrons in

the FMM phase, oscillator strength around 1.5 eV in the COI phase is transferred to a Drude response at low energy in the FMM phase. Consequently, the COI reflectance in the visible and near-infrared, used in the imaging experiments, is higher than the FMM reflectance. Consistent with the free-carrier response of a metal, at low energy the FMM reflectance increases as energy decreases about 7 times faster than the COI reflectance and becomes about twice as large. Also reflecting a phase change, the plots from the PM phase are significantly different from the FMM plot. In particular, the decrease in the reflectance at low energy is consistent with a broadening of the Drude response corresponding to a polaron-hopping conductivity in the PM phase.

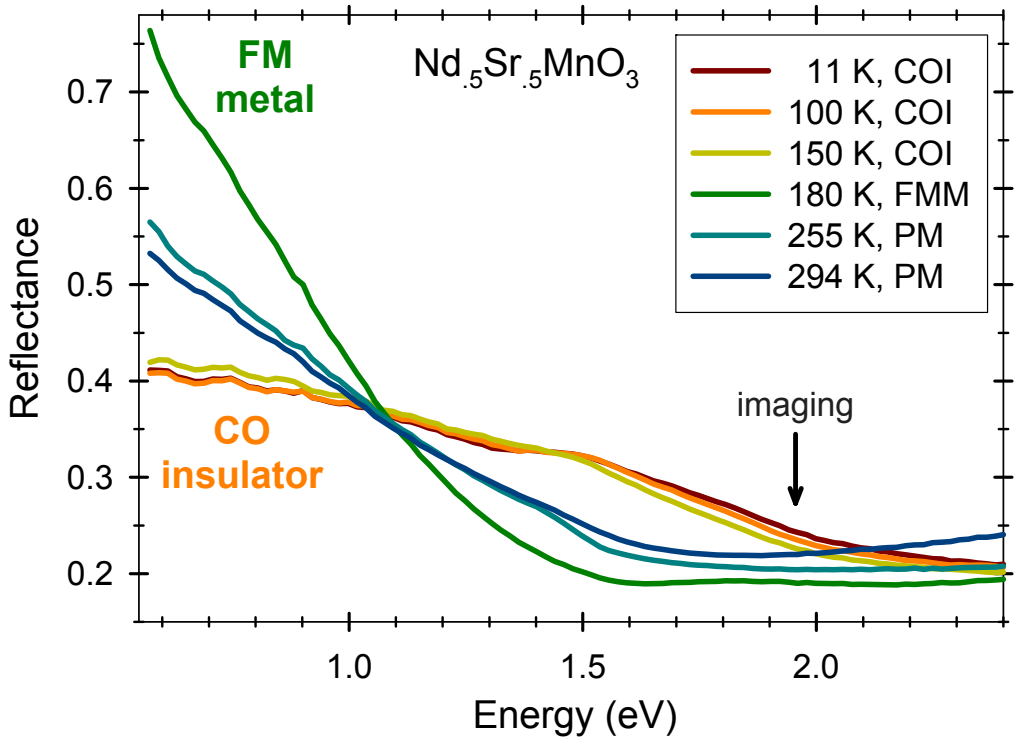

Figure 4.7. Reflectance vs. photon energy for the $Nd_{½}Sr_{½}MnO_3$ sample at six different temperatures. Most imaging experiments are performed at 1.96 eV.

4.2 Far-field Imaging of Optical Domains

Far-field imaging was performed on $Nd_{½}Sr_{½}MnO_3$ primarily to complement the NSOM imaging. Far-field microscopy as an investigational tool possesses worthiness of its own, and few studies of the manganites have been made in this way. Compared to NSOM, the chief advantages of far-field imaging are ease of use, speed of image capture, and large image size. Far-field imaging is well suited to characterizing the extent and interaction of both optical domains and phase domains. With far-field imaging as a backdrop, the high resolution imaging of domain boundaries by NSOM can be better interpreted.

4.2.1 Experimental Setup

Far-field micrographs of $Nd_{½}Sr_{½}MnO_3$ were taken with a traditional bright-field, reflection microscope. A commercial tungsten lamp was used for illumination. Narrow-band interference filters were placed in the illumination path to make the light quasi-monochromatic. The polarization was controlled by rotating a Glan-Taylor type polarizer which was placed in the illumination path directly after the field aperture of the microscope. The sample was placed in an Oxford cryostat, called a microstat, with a quartz optical window and was cooled by a continuous flow of cold helium. A commercial heater with a proportional-integral-derivative (PID) feedback circuit was used to control the sample temperature to within a tenth of a Kelvin. The microscope objectives used had magnifications of 4x, 10x, and 40x with numerical apertures of 0.13,

0.30, and 0.55 respectively. The 40x objective was designed to compensate for optical windows of varying thicknesses. Images were directed to the top of the microscope where they were recorded by a CCD camera. Typically, no analyzing polarizer was placed in front of the camera.

4.2.2 Ferromagnetic Metal (FMM)

According to both the phase diagram of Figure 4.1 and the magnetic susceptibility curve of Figure 4.5, $Nd_{½}Sr_{½}MnO_3$ is a FMM from about 160 K to about 250 K. The FMM phase is considered first because it is the parent phase for the martensitic-like transition into the COI and because its microscopic appearance is almost identical to the PM phase. The micrographs in Figure 4.8 show that there is indeed optical anisotropy in this electronic phase.

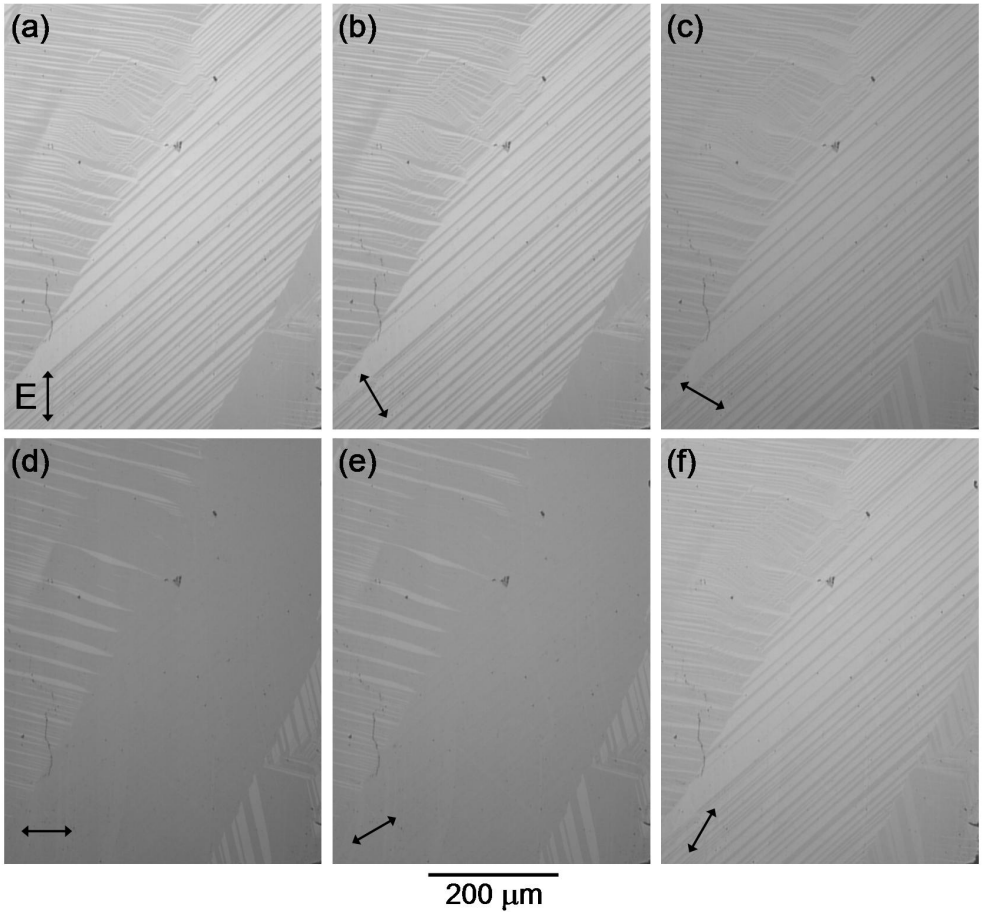

Figure 4.8. Optical micrographs of the FMM phase using the 10x objective. 190 K is the temperature. 600 nm, bandwidth 25 nm light is used. The polarization of illumination is successively rotated by 30° as indicated by the double arrows.

The micrographs of $Nd_{½}Sr_{½}MnO_3$, showing a large number of lattice imperfections, are reminiscent of similar images of martensitic metals. The central band running diagonally from lower left to upper right shows alternating dark and bright lines for vertically polarized light. Borrowing the terminology from martensitic metals, this band is most likely a variant with

very straight, regular twins. In other places, the twins have a wavy appearance perhaps due to the deforming interaction between variants.

4.2.3 Paramagnetic Insulator (PM)

Upon cooling the sample into the FMM phase from the PM phase, no major differences are apparent in the micrographs, as seen in Figure 4.9. This suggests that the transition involves a fundamental change in electronic properties rather than crystal properties. It should probably not be described as martensitic since there is no large-scale surface upheaval apparent.

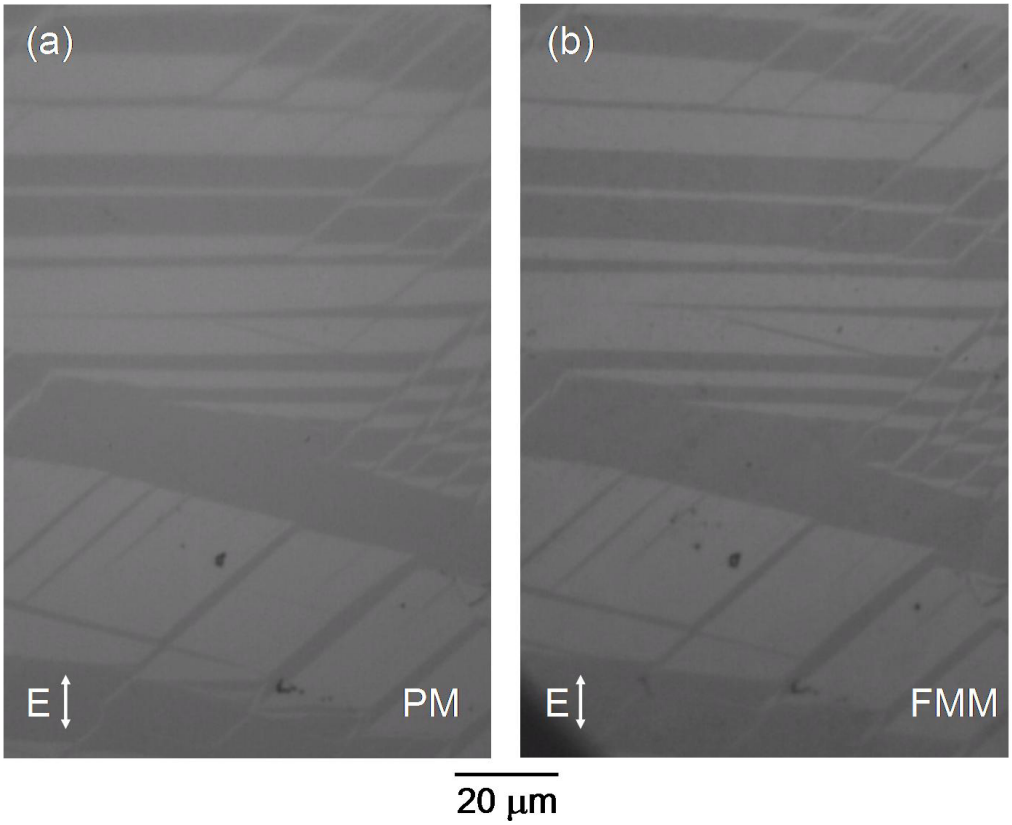

Figure 4.9. Optical micrographs comparing the PM and FMM phases. The temperature is 265 K in the PM phase (a) and at 220 K in the FMM phase (b). Both images are taken with the 40x objective using vertically polarized light with a wavelength of 630 nm, bandwidth 10 nm. The micrograph in (b) shows some granularity due to freezing of vapor that typically occurs in the cryostat at about 250 K. The dark triangle at the lower left of (b) is the field stop. No major differences are seen in the optical domain structure.

4.2.4 Charge-ordered Insulator (COI)

Optical micrographs of the COI phase are similar to those in the FMM and PM phase but differ in some fundamental ways. Contrast between optical domains in the COI phase is more pronounced than in the FMM phase. The overall image brightness is greater in the COI phase, as would be expected

from the reflectance plots of Figure 4.7. Figure 4.10 shows the COI phase illuminated by different polarizations. In this particular region, two variants dominate. Each of these variant appears as two parallel, broad bands running from upper right to lower left. The bands of one type of these dominant variants are separated by a band of the other. Figure 4.11 at higher magnification shows a variant boundary and the twinning that occurs in the variants.

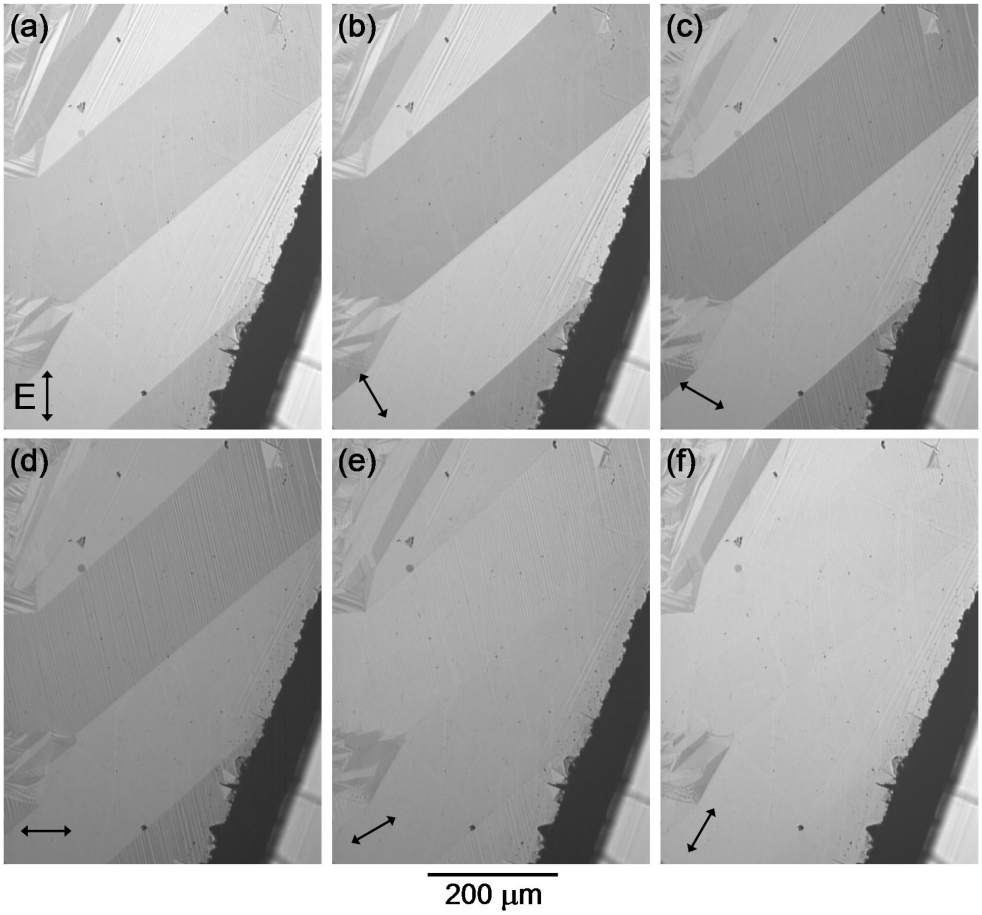

Figure 4.10. Optical micrographs of the COI phase using the 10x objective. The temperature is 80 K. 600 nm, bandwidth 25 nm, light is used. The polarization of illumination is successively rotated by 30° as indicated by the double arrows.

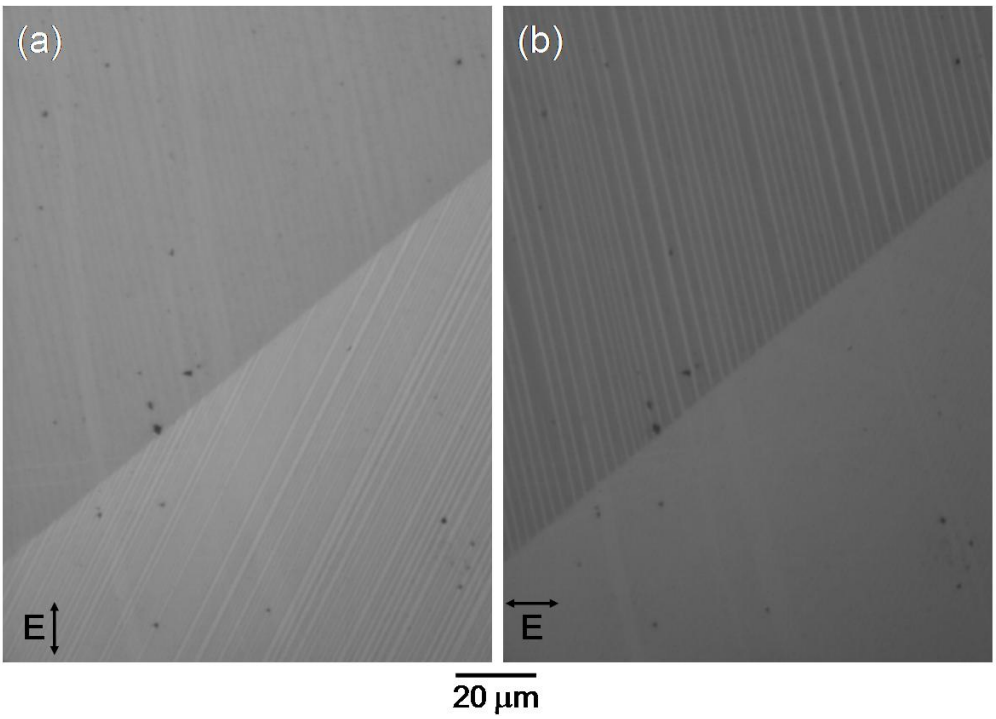

Figure 4.11. Optical micrographs of a COI variant boundary using the 40x objective. The temperature is 80 K. 600 nm, 25 nm bandwidth light is used. The polarization of illumination is vertical in (a) and horizontal in (b).

Though the surfaces occasionally bear some resemblance, the COI surface is generally very different than the FMM parent surface. This is shown in Figure 4.12 and is indicative of a dramatic change in crystal structure. The presence of surface upheaval is characteristic of a martensitic transition.

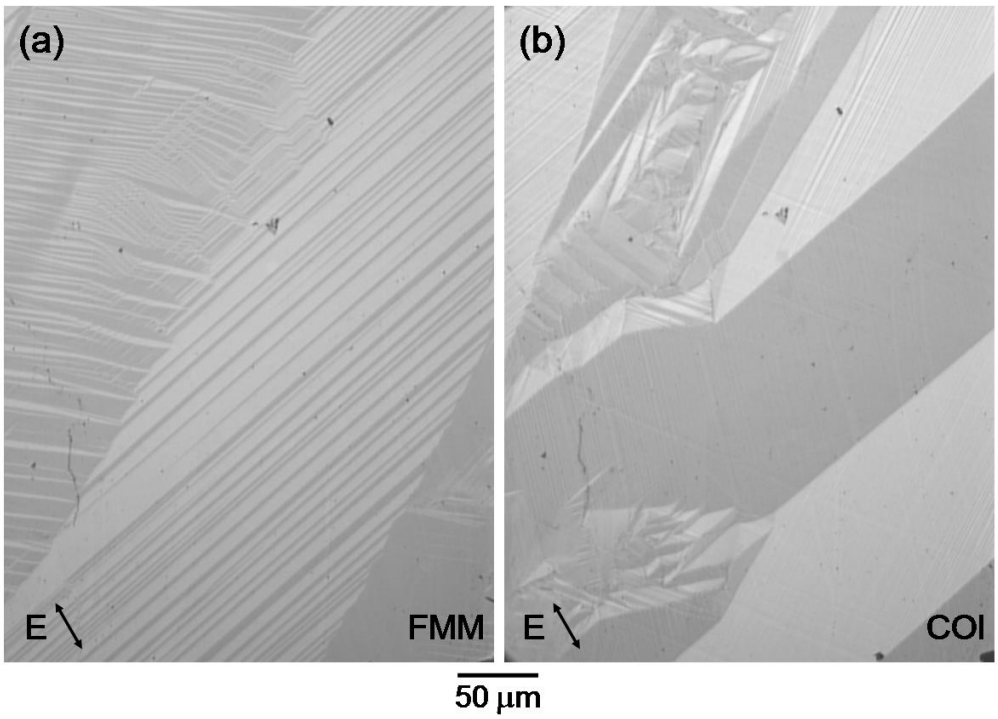

Figure 4.12. Optical micrographs comparing the FMM and COI phases. The same region is imaged in (a) at 190 K and in (b) at 148 K. 600 nm light, 25 nm bandwidth light is used. The polarization of illumination is 30° from the vertical.

As with polarization, changing the wavelength of illumination can reveal different features of the sample. The contrast of the optical anisotropy changes with wavelength and can even be reversed. This is shown in Figure 4.13 where three wavelengths with two polarizations are shown. For one polarization, the contrast between twins is high. When rotated by 90° the contrast virtually disappears. Also present at all wavelengths and polarizations are faint bright lines at about 15° counterclockwise from the twins. These arise from the residual faceting of polishing/annealing and are essentially unchanged by wavelength or polarization. In the high contrast micrograph at 670 nm, the

twins become bright on the upper edge and dark on the lower edge. This combination of wavelength and polarization is apparently sensitive to strain arising on the twin boundary.

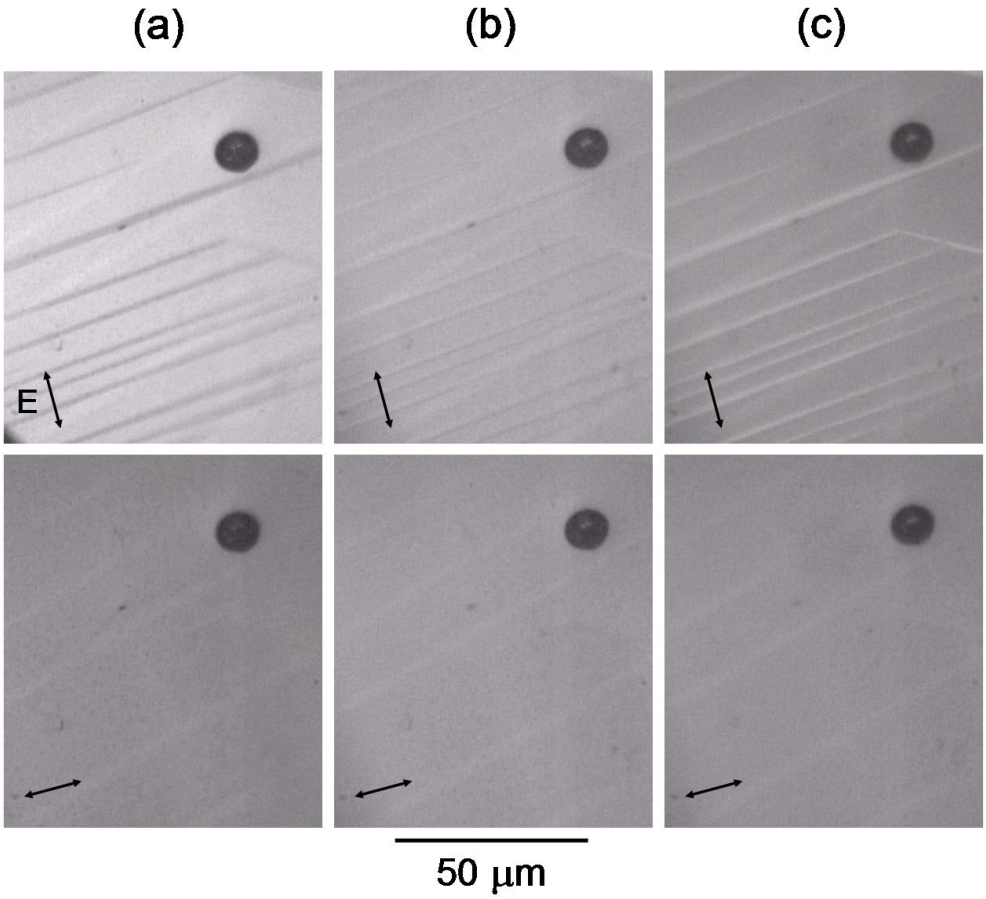

Figure 4.13. Optical micrographs of the COI phase using the 40x objective with 630 nm (a), 670 nm (b), and 730 nm (c) illumination. The temperature is 80 K. The light bandwidth is 10 nm. The polarization of illumination is 15° counterclockwise from vertical for the upper micrographs and 75° clockwise from vertical for the lower ones.

4.2.5 Martensitic Formation of COI domains

The transition from FMM to COI was imaged as a function of temperature. Large COI phase domains suddenly appear as the temperature is

lowered by a just a few mK below the transition temperature. Though the imaging system used did not have synchronous control, some rough estimates of the time scales of the transition can be made. At constant temperature slightly below the transition temperature, some COI domains initially grow quickly, on a time scale of seconds, as large distinct variants. Growth then slows down to a crawl, and a drop in temperature of a few degrees is needed to complete the transition. Figure 4.14 shows one region as it makes a transition from FMM to COI. Initially, wedges of bright COI variants slam through the top left and lower right regions of the micrograph. This has a dramatic effect on the FMM twins in the center as they become strained and distorted. Small, bright COI domains pop up in the upper part of the region. A slightly darker COI variant then penetrates the region from the middle right and joins the bright variant below it. The variants continue to grow as a large, bright variant appears in the upper right. Small, bright variants continue to pop up. However, at this point the transition slows considerably, and the temperature must be lowered several degrees to continue and eventually complete the process. In Figure 4.14(f), the temperature has been lowered by 3 K, but some dark FMM domains still remain. Accordingly, there are an increasing number of small COI variants with very complex boundaries. Unlike the FMM optical domains which evolve due a changing stress, once COI optical domains form they remain unchanged while the transition proceeds. This implies that during the transition, stress can change the crystal orientation of the FMM phase but not the crystal orientation of the COI phase.

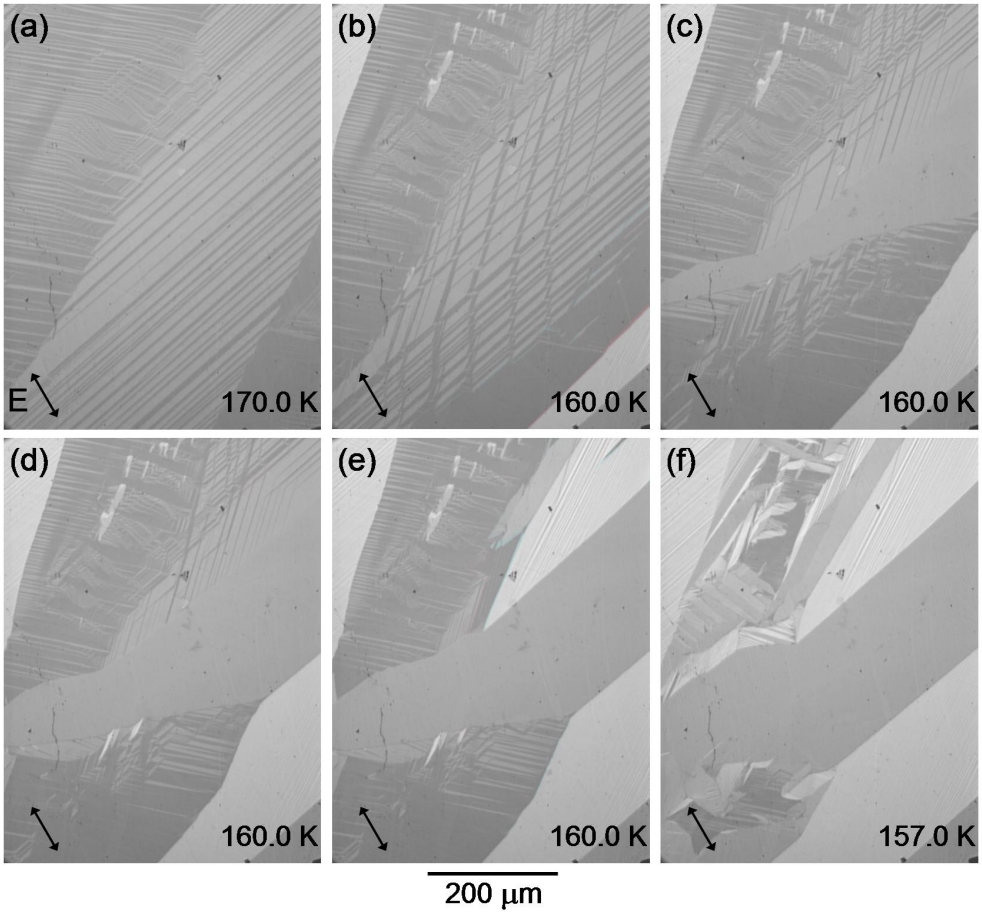

Figure 4.14. Optical micrographs of the transition from FMM to COI using the 10x objective. 600 nm light, 25 nm bandwidth, light is used. The polarization of illumination is 30° counterclockwise to vertical.

4.2.6 Nucleation of the FMM Phase

The nucleation of the FMM occurs at first very slowly, over a range of temperature of about 13 degrees and tends to occur on variant boundaries. Nucleation and growth of the FMM are shown in Figure 4.15 at low magnification. These micrographs are dominated by COI variant bands running diagonally from the lower left to the upper right. Additionally, there are smaller, irregularly shaped variants which are more difficult to pick out.

The FMM phase domains, generally seen as dark regions, first appear along various variant boundaries, preferentially choosing some over others. The FMM domains then grow, forming wedge-like patterns that eventually merge with other FMM domains. Qualitatively speaking, the initial FMM transition upon heating occurs much more slowly than the reverse transition, i.e. the COI growth upon cooling, and there is phase coexistence over a larger range of temperature. The FMM nucleation on the variant boundary running through the center of Figure 4.15 is shown under high magnification in Figure 4.16. These micrographs suggest that the FMM tends to nucleate where strain is at a maximum. As the transition proceeds and new FMM phase domains appear, existing FMM optical domains appear and evolve. This suggests an evolving strain pattern in the FMM crystal. Meanwhile the surviving COI optical domains appear not to change in response to an evolving strain.

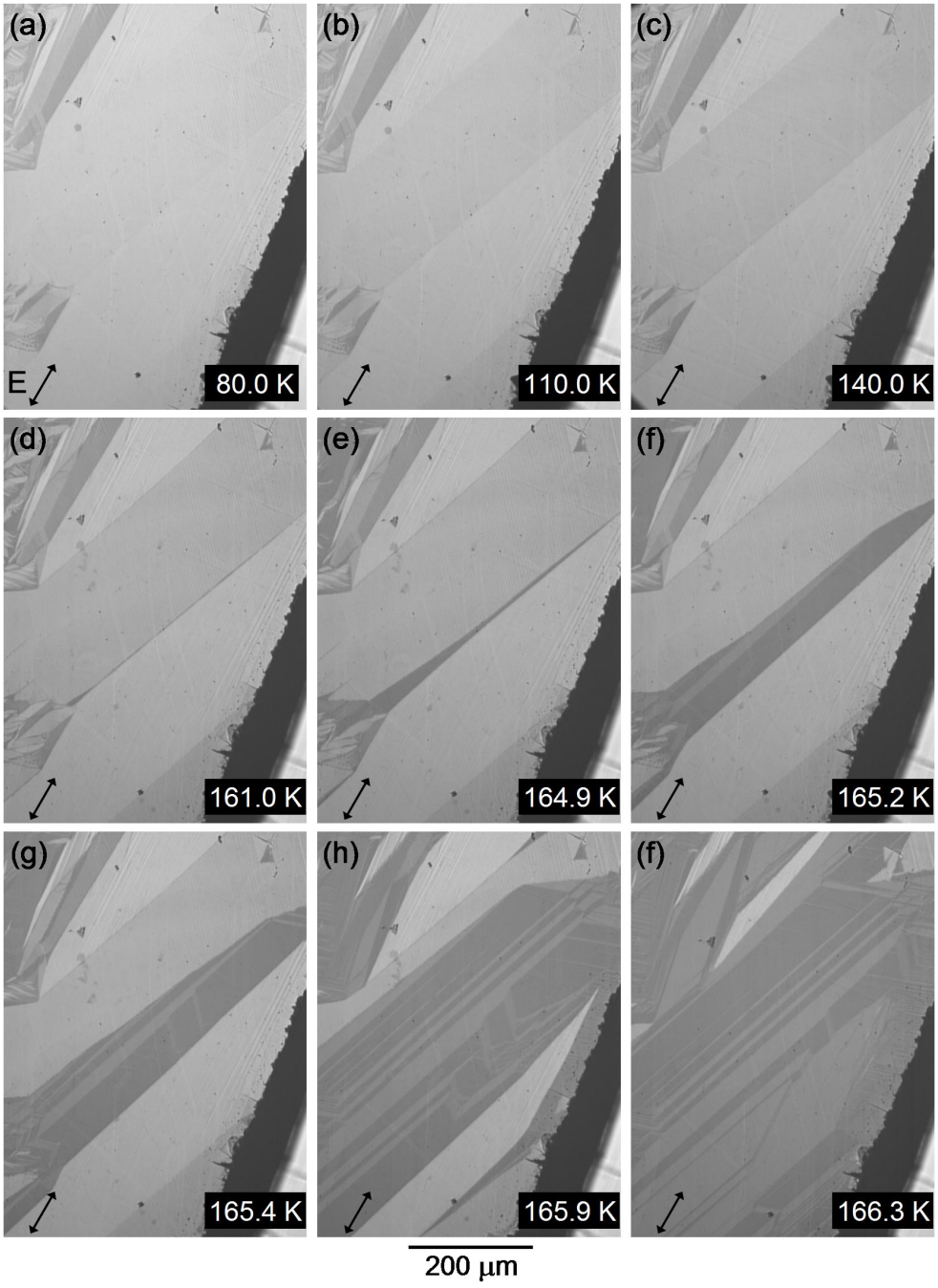

Figure 4.15. Optical micrographs of the nucleation and growth of the FMM phase domains (dark regions) using the 10x objective. 600 nm light, 25 nm bandwidth light is used. The polarization is 30° clockwise from vertical.

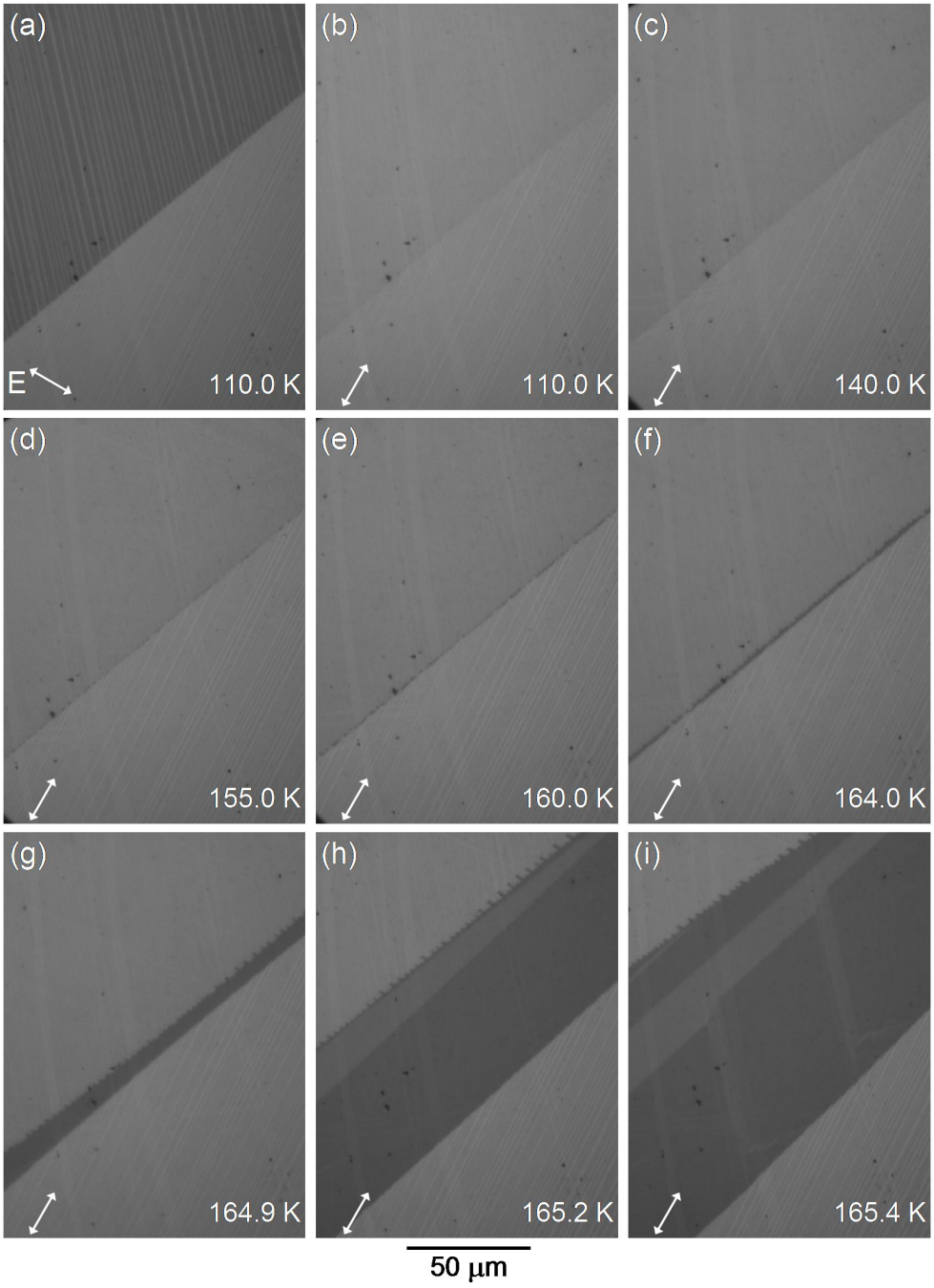

Figure 4.16. Optical micrographs of the nucleation and growth of the FMM phase domains using the 40x objective. 600 nm light, 25 nm bandwidth light is used. The polarization is 60° counterclockwise from vertical in (a) to show a variant boundary and the twins on either side. In (b) through (i), the polarization is 30° clockwise from vertical.

The FMM phase might also be expected to grow along twin boundaries. However, before this can occur, twinned COI regions are usually overwhelmed by FMM domains growing from elsewhere. What can be asserted from far-field imaging is that the FMM phase may occasionally nucleate on a twin boundary and often prefers to grow along a twin boundary than in a random location. An example of this is shown in Figure 4.17. The polarization can be chosen to image the COI twin domain structure as in 4.17(a) and (b) or to pick out FMM phase domains as in 4.17(c) through (i). As the temperature rises, a dark FMM needle appears roughly in the center of 4.17(d). Using the speck of dirt at its center as a fudicial mark, a comparison of 4.17(d) with (a) and (b) shows that the left part of the FMM needle lies along a COI twin boundary. The right part of the needle curves upwards and terminates on another twin boundary. The needle then disappears at slightly higher temperature in 4.17(f). As the temperature rises further, long narrow FMM wedges grow along the twin boundaries in 4.17(g), (h) and (i). Relative to the thinner COI twins, the FMM wedges point to the left on the upper boundaries and to the right on the lower boundaries.

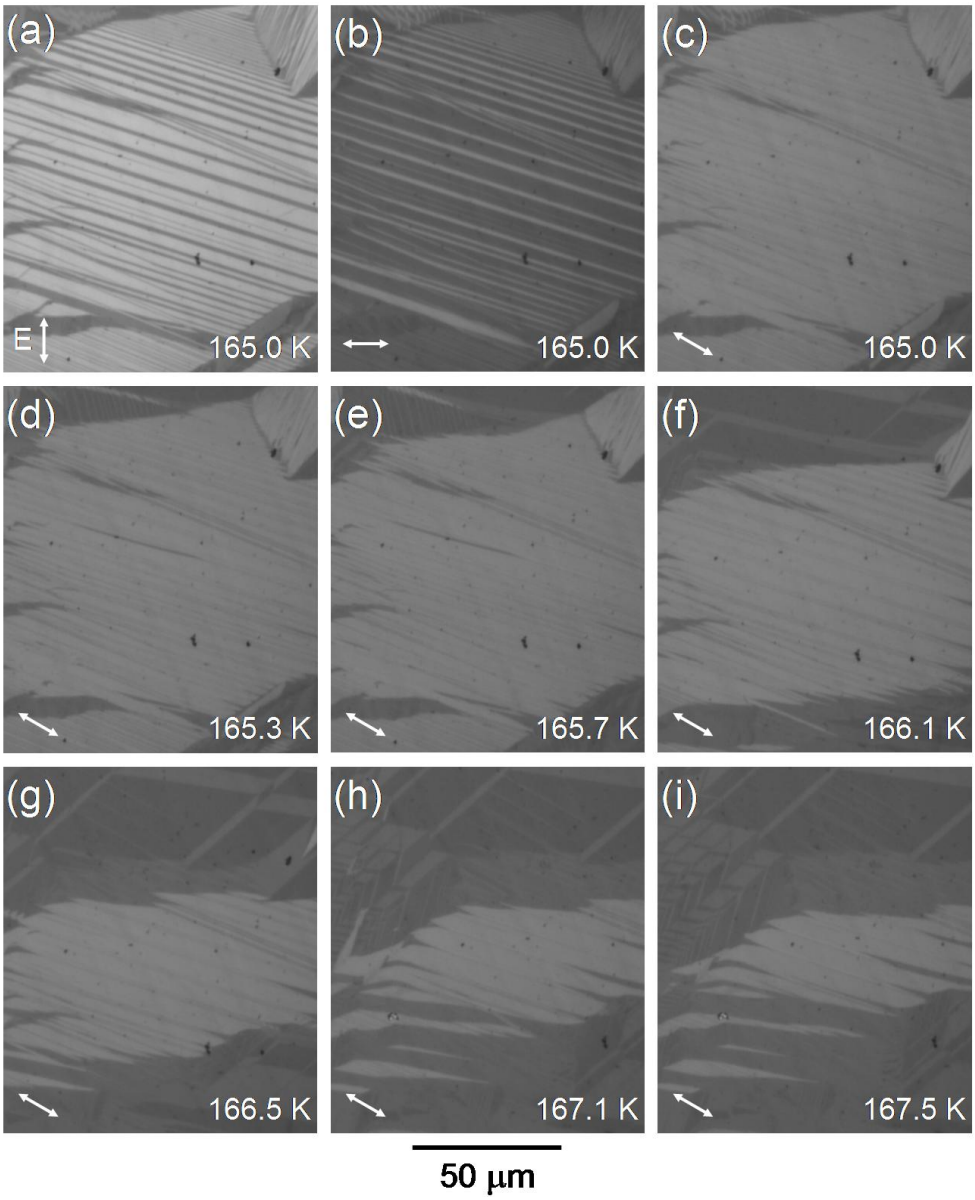

Figure 4.17. Optical micrographs of the nucleation and growth of FMM phase domains along COI twins using the 40x objective. 600 nm, 25 nm bandwidth light is used. The polarization is vertical in (a) and horizontal in (b) to reveal COI twins. The polarization is 30° clockwise from vertical is used in (c) through (i) causing FMM domains to be dark and producing almost no contrast from twinning in COI domains.

4.3 Near-field Imaging of Optical Domains

The far-field imaging of $Nd_{½}Sr_{½}MnO_3$ helps set the scope for the near-field imaging. Far-field experiments show that optical domains and phase domains exist and both can be optically imaged. It shows that variants can be hundreds of microns in extent in the PM, FMM, and COI phases. Finding variant boundaries with NSOM, with its scan range of a few microns, promises to be difficult and was not attempted at the date of writing this dissertation. The NSOM is most suited for investigating the optical domains with the smallest widths, i.e. twins. Far-field imaging also shows that nucleation of FMM phase domains is potentially slow enough to be imaged by NSOM. The nucleation can occur along twin boundaries if a FMM phase domain from elsewhere in the sample does not encroach upon the twin. NSOM can image the twins with higher resolution than in far field and provide topographic information as well.

4.3.1 Experimental Setup

Near-field images in this thesis are generated in the so-called emission mode since light is sent through the tip and collected in the far-field. The collection optics and method of polarization control are illustrated in Figure 4.18. As described in 2.3.1, the polarization is controlled with 3-paddle polarization manipulators. With the tip in near-field approach to the sample, it was not possible to determine the output polarization state. Instead the tip was pre-scanned over a region with optical anisotropy while the paddles were

adjusted to maximize contrast. Typically, the orthogonal polarization state was also used to scan the sample. The average NSOM signal varied from scan to scan by as much as a factor of two. The sample reflectance, the NSOM probe throughput, and the light detection system can all exhibit polarization sensitivity and contribute to this variation. For convenience of viewing, each NSOM scan is re-scaled so that the lowest value is 100.

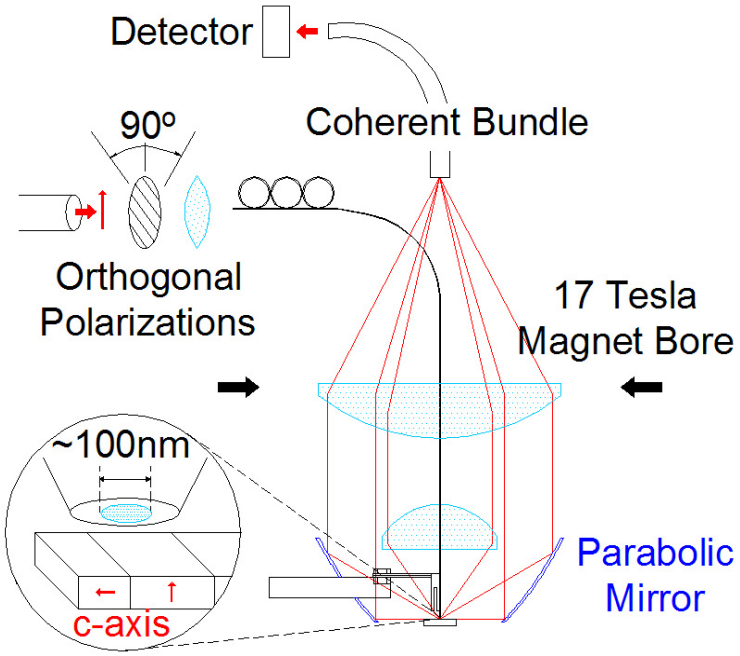

Figure 4.18. NSOM Collection optics and polarization control for imaging of optical and phase domains.

4.3.2 Light Intensity and Topographic Images

Anisotropy can be seen in the near-field for the COI, FMM, and PM phases. As in the far-field, narrow bands consistent with twinning are frequently seen. These twins often show polarization effects near their edges reminiscent of the far-field image of Figure 4.13. Most of these edge effects

would be difficult to observe and impossible to resolve in the far-field. Typically, topographic images reveal faceting of the surface which coincides with regions of optical anisotropy. Additionally, there are other facets that show only slight polarization contrast. For this reason and because these facets have twins running through them, it is probable that they are part of the topography that is frozen-in during polishing/annealing. Dramatic edge effects are not seen in these types of facets. Because edge effects are occasionally seen in the far-field and because they are seen in the near-field only coincident with optical domain topography, they are probably not artifacts. A potential cause of the anisotropic edge effects is strain near the twin boundaries. This possibility is discussed in more detail once NSOM images are presented.

Figure 4.19 shows NSOM scans in the FMM phase while Figure 4.20 shows scans in the COI phase. Both figures show topographic particles which cause high intensity artifacts in the NSOM images. There is a particularly large particle in the scans of Figure 4.19. Both figures also show the presence of frozen-in facets in near-field intensity and topographic scans. These facet boundaries run parallel in the scans at about 65° counterclockwise from the *x*-axis. From scan to scan, the near-field intensity signal from these facets is only weakly polarization dependent. Contrast from these regions presumably comes from a preference in the illumination/detection system as described in 2.3.2. Running through the frozen-in facet boundaries are faceted stripes that make an angle of about 35° clockwise from the *x*-axis. These stripes exhibit a stronger polarization contrast, including contrast reversal and edge effects, and

are presumed to be the signature of optically anisotropic twin domains. Another indication that the edge effects are not artifacts comes from Figure 4.20(b), where a bright (dark) edge corresponds to a facet valley (ridge). Due to the sample lens effect described in 2.3.2, a sample valley (ridge) would be expected to artificially increase (decrease) the NSOM signal. Also described in 2.3.2, straight lines may appear slightly curved due to piezo hysteresis, non-linearity and coupling of *xy* with *z*-motion. These effects tend to increase with temperature. Turning on the heater to warm the sample to the FMM phase introduces noise in the near-field tip-to-sample feedback. As a result, the scans of Figure 4.19 are noisier than those of Figure 4.20, and the scan ranges are reduced as a practical precaution.

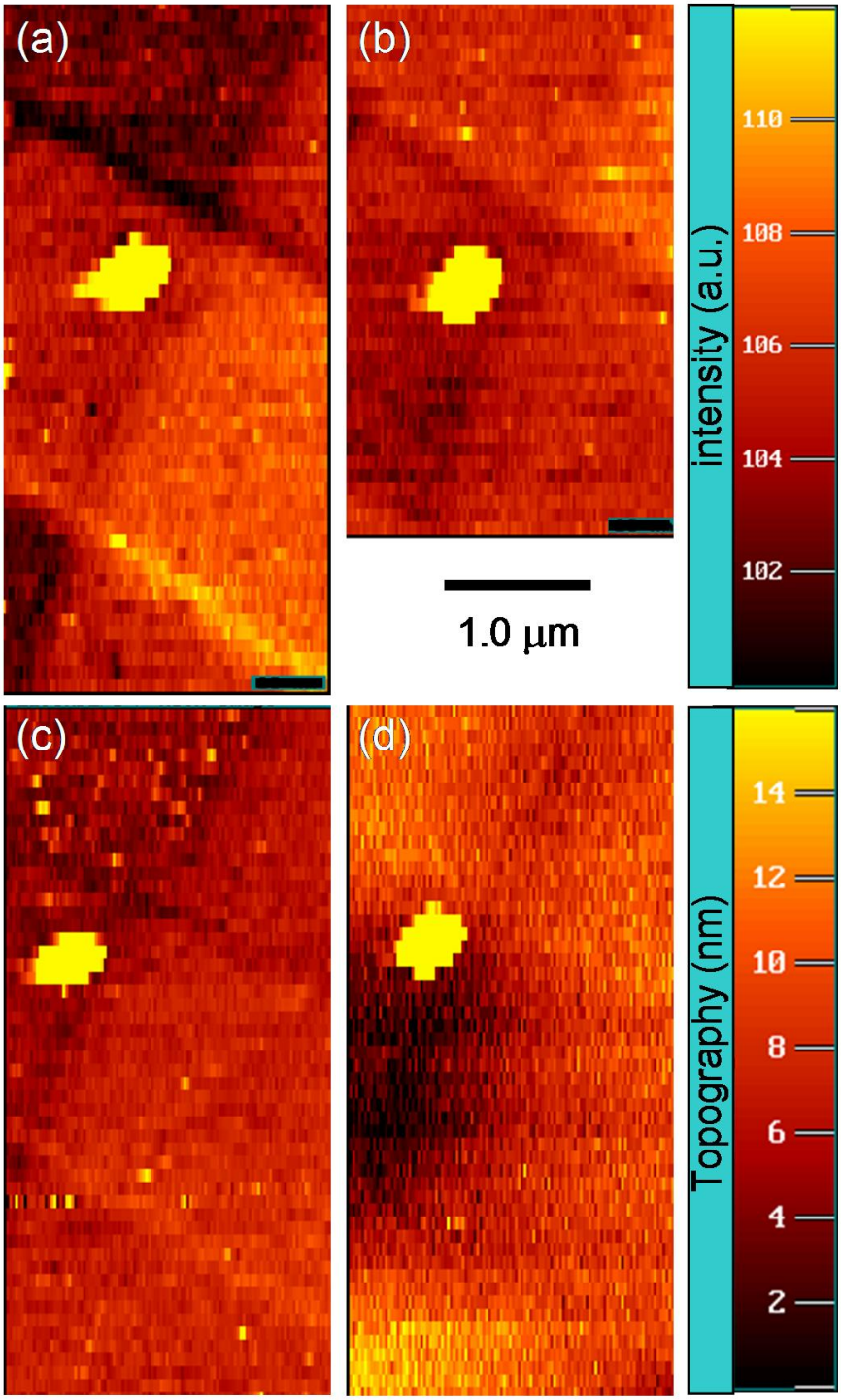

Figure 4.19. NSOM scans of the FMM phase using 633 nm light. Polarization is adjusted to maximize contrast in (a), the orthogonal polarization is used in the (b), and an arbitrary polarization is used in (c). The topography is shown in (d). The temperature is 193 K.

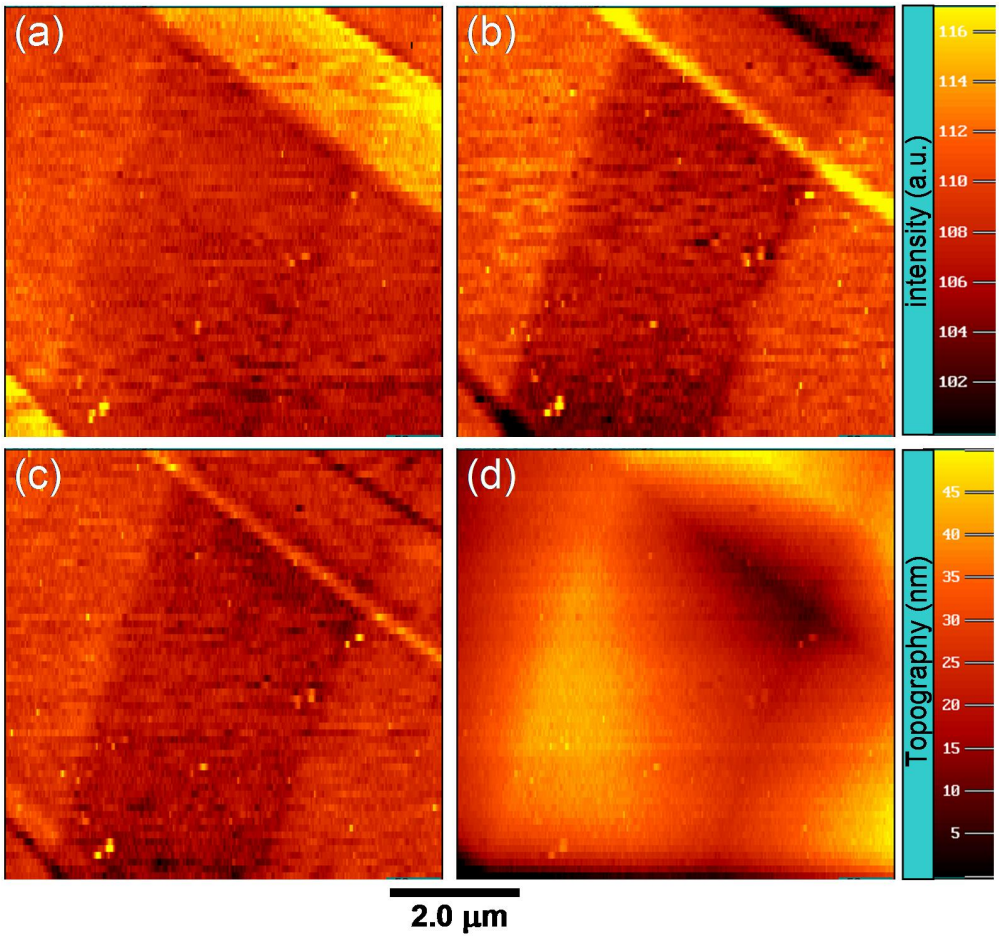

Figure 4.20. NSOM scans of the COI phase using 633 nm light. Polarization is adjusted to maximize contrast in (a), the orthogonal polarization is used in the (b), and an arbitrary polarization in (c). The topography is shown in (d). The temperature is 77 K.

Differences in contrast between the near-field and far-field are presumably due to a difference in the effective angle of illumination. As described in 2.3.2, the NSOM probe and sample can be modeled as a waveguide in which rays at large angles to the normal are most efficiently emitted and detected. Conversely, far-field illumination and collection is

essentially a cone centered on the normal. Contrast of COI optical domains in the far-field tends to be about 50% at 630 nm, but the near-field contrast is typically only about 10%. The case is similar for FMM and PM optical domains. The near-field contrast between phases also differs from the far-field. The average NSOM signal before re-scaling of the scans of Figure 4.19 in the FMM phase is roughly the same as those of Figure 4.20 in the COI phase.

Perhaps the most interesting features of the NSOM scans of Figures 4.19 and 4.20 are the alternating bright and dark edges of the twin boundaries. As previously mentioned, a potential cause of the anisotropic edge effects is strain. In this picture, stress causes the Mn-O bonds to change length and thus introduces additional optical anisotropy. The stress might be expected to take the form of tension, rather than shear, since it would produce the larger change in bond length; linear with tensile stress but quadratic for shear stress. Because the edges alternate between bright and dark, the stress should also alternate from tensile, perpendicular to one side of the boundary, to compressive, perpendicular to the other side. Local strain conditions would be expected to vary, and accordingly edge effects are not present in every NSOM scan.

Though a thorough and systematic near-field survey of the sample would be enormously time-consuming, some tentative conclusions may be reached from a limited survey. Sample roughness in the form of faceting seems to be most prominent in the COI phase. As twins get smaller and closer together, the COI surface appears to get rougher. This is demonstrated by the scans of Figure 4.21. Diagonal twins are seen crossing a frozen-in facet boundary.

Apparently due to the relatively large tilt between twin facets, the sensitivity of the illumination/detector system to angle becomes significant. As a result, the contrast is enhanced between twins, but it can not be reversed or even reduced to zero. The stripe in the upper right of the scans appears to be only about 100 nm wide at the resolution limit of the NSOM. Conversely, the FMM or PM phases generally do not demonstrate densely packed parallel twins. Figure 4.22 presents an example where complex optical domains are fairly densely packed, yet the associated topography is rather minimal.

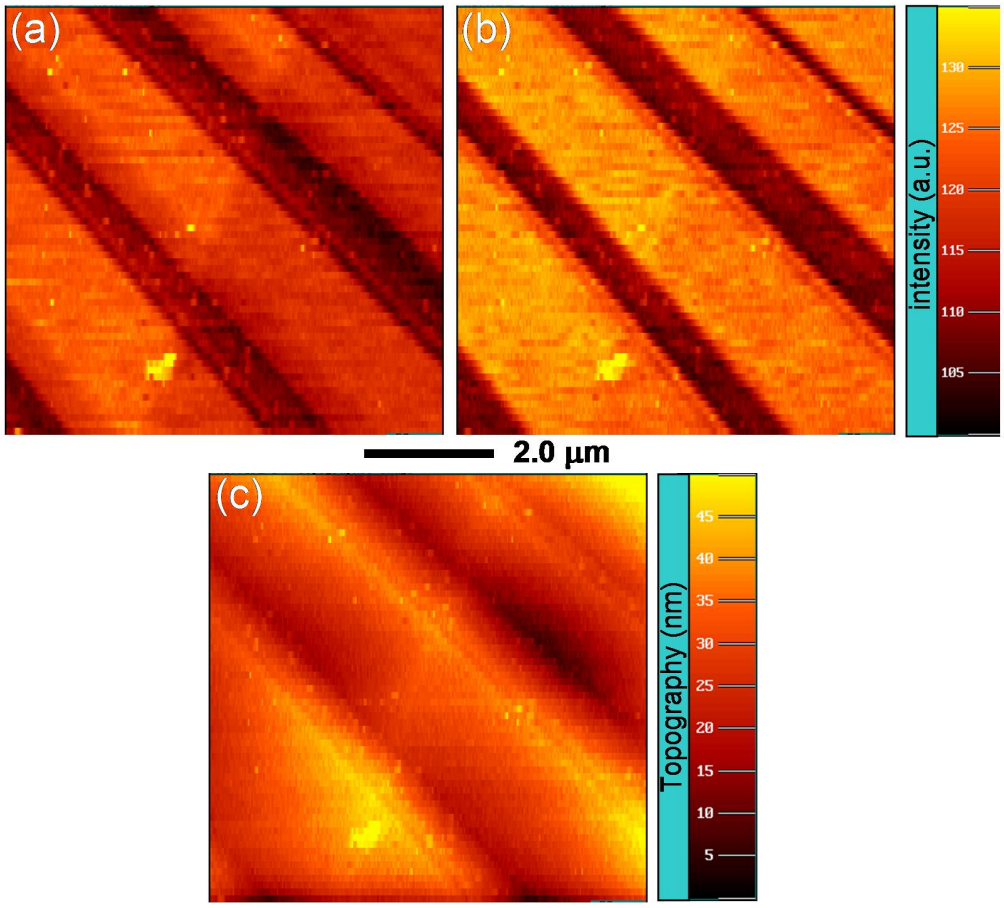

Figure 4.21. NSOM scans of the COI phase using 633 nm light. Polarization is adjusted to minimize contrast in (a), the orthogonal polarization is used in (b). The topography is shown in (c). The temperature is 77 K.

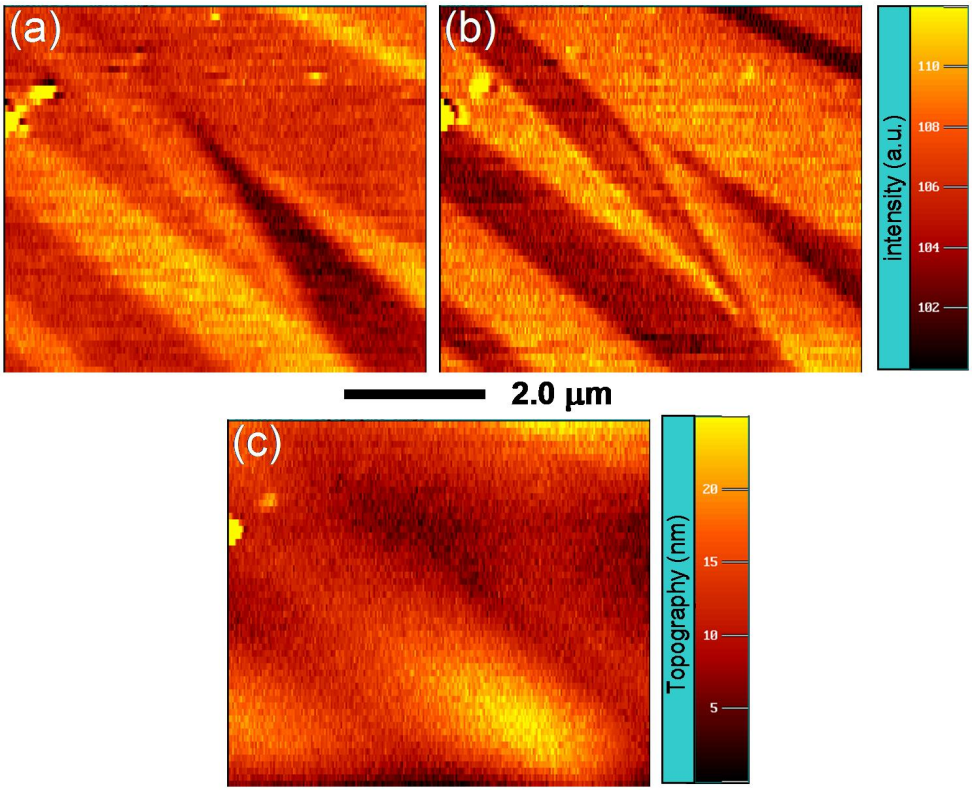

Figure 4.22. NSOM scans of the PM phase using 633 nm light. At room temperature, the polarization is adjusted to maximize contrast in (a), the orthogonal polarization is used in (b), and the topography is shown in (c).

4.3.3 Temperature Dependence

Despite several practical limitations, we were able to look at a particular spot on the sample as temperature is swept through the COI to FMM transition. Because of the relatively large thermal mass of the NSOM system, heating the NSOM by a few Kelvin to a stable temperature can take about half an hour. Due to differential thermal contractions, the relative position of tip to sample changes in both *z* and *xy* on the order of microns per Kelvin. There is sufficient coupling of the *z*-positioning screws to the *xy*-sample position to compensate for the thermal motions. However, the process is not straightforward, and since

NSOM scans typically take a few minutes per square micron, it adds significant delay to the experiment. Scans are usually slowed down further as a precaution against mechanical instabilities caused by the heater in the temperature control system. The observed spot may undergo sudden changes during the phase transition, and the spot may not be recognizable from scan to scan.

One micron wide gold lines deposited on GaAs were scanned to calibrate the scan range of the NSOM as a function of temperature. The calibration uncertainty in the scan range at a given temperature is typically 5%. Calibration scans used a zero *xy*-offset and a near-field approach near the center of the range of the *z*-actuator. However, to compensate for differential thermal contractions, a range of *xy*-offsets and of *z*-actuator displacements was used in the scans of the COI to FMM transition.

Figure 4.23 shows the near-field intensity scans from one temperature sweep where a COI twin stripe is observed and followed as a function of temperature. This stripe appears dark for one polarization and bright in the orthogonal polarization. As temperature is increased, the exact spot along the stripe changes from scan to scan, but common artifacts from particles can sometimes be seen. Also, the noise is increased as the heater is driven harder. The measured width of the stripe decreases by about 10% as the temperature is swept upwards, which may be an artifact of changing *xy*-offsets and *z*-actuator displacements. Eventually the FMM phase is apparently reached. During two scans at 167 K, the approach feedback began to jump discontinuously.

Presumably the sample surface was heaving during the COI to FMM phase transition causing the NSOM tip to suddenly change height. In the second scan, the near-field signal also jumped by 25%, probably due to a minor crash of the tip into the sample surface. After some time order was restored, and the scans began to be reasonable again. Although the polarization state could have changed due to the presumed crash of the tip, these scans, shown in Figure 4.24, reveal a changed structure under the tip. Instead of a single stripe, what appears to be a single boundary now appears. Changing polarization shows that the boundary is perhaps not a simple, single boundary. The complex structure revealed in the scans could be an indication of the strain field along the boundary. Alternatively, the narrow, dark-looking region could be either an unusually thin FMM domain or a thin remnant of the COI phase.

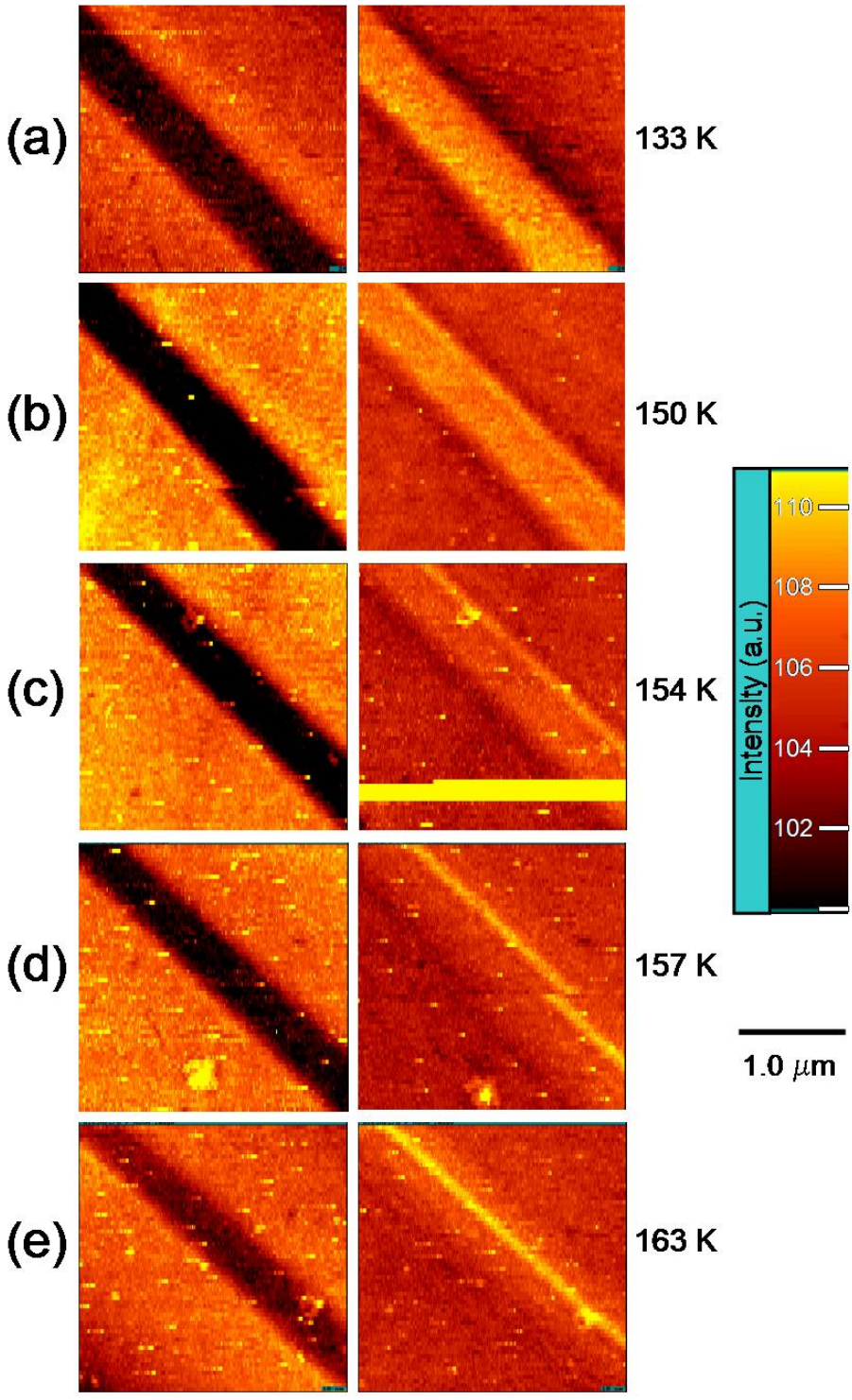

Figure 4.23. NSOM scans of the COI phase as temperature is swept upwards. Orthogonal polarizations are used in left and right scans. The wavelength used is 633 nm.

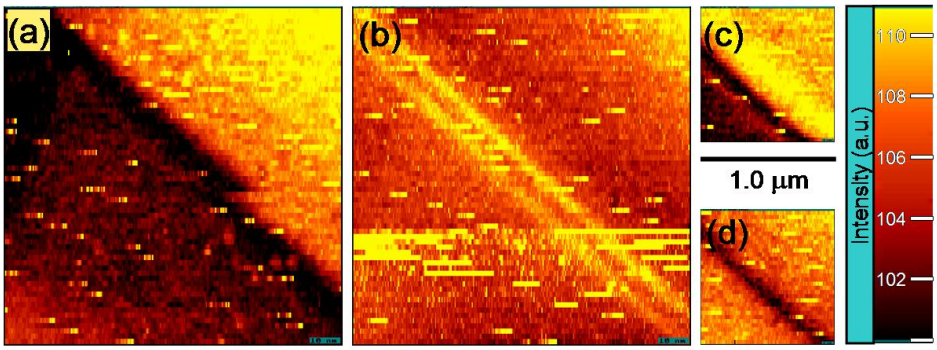

Figure 4.24. NSOM scans of the newly formed FMM phase. Orthogonal polarization states are used in (a) and (b). The polarization has been adjusted to maximize contrast in (c) with the orthogonal polarization used in (d). The wavelength used is 633 nm. The temperature is 167 K.

Starting with 4.23(a) at 133 K, there is no dramatic qualitative change in the near-field intensity image until (c) at 154 K, a temperature at which FMM domains can be forming. In the polarization where the COI twin-stripe appears bright, the overall contrast of the stripe is reduced except in a narrow region at the upper boundary. This phenomenon had been observed in a previous temperature sweep as well, shown in Figure 4.25. In both sweeps, relatively little topography is observed, as shown in Figure 4.26. The interpretation of the NSOM scans during the temperature sweep is somewhat subtle. The images suggest two possible explanations: one involving strain and one involving the formation of the FMM phase.

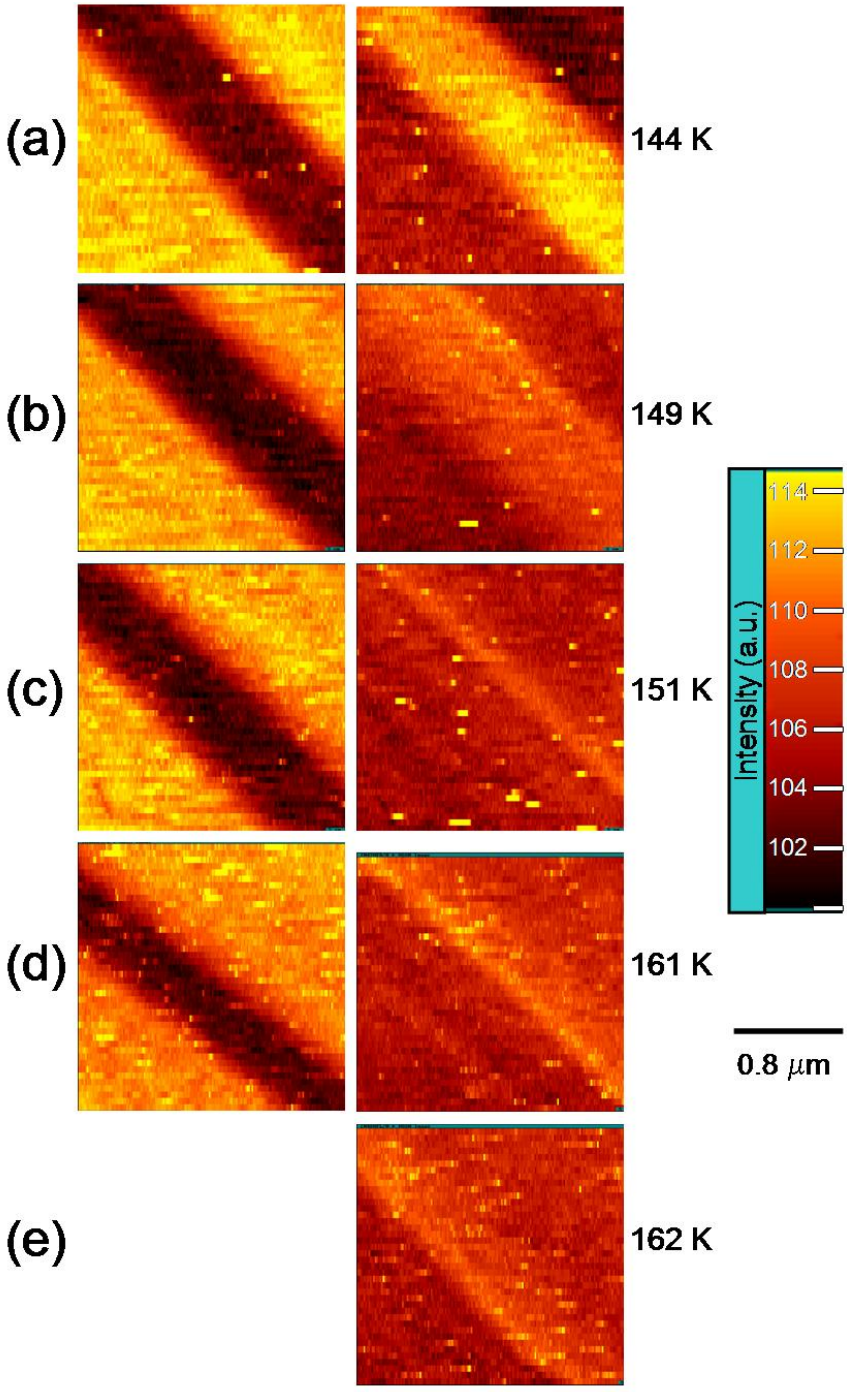

Figure 4.25. Second set of NSOM scans of the COI phase as temperature is swept upwards. Orthogonal polarizations are used in left and right scans. The wavelength used is 633 nm.

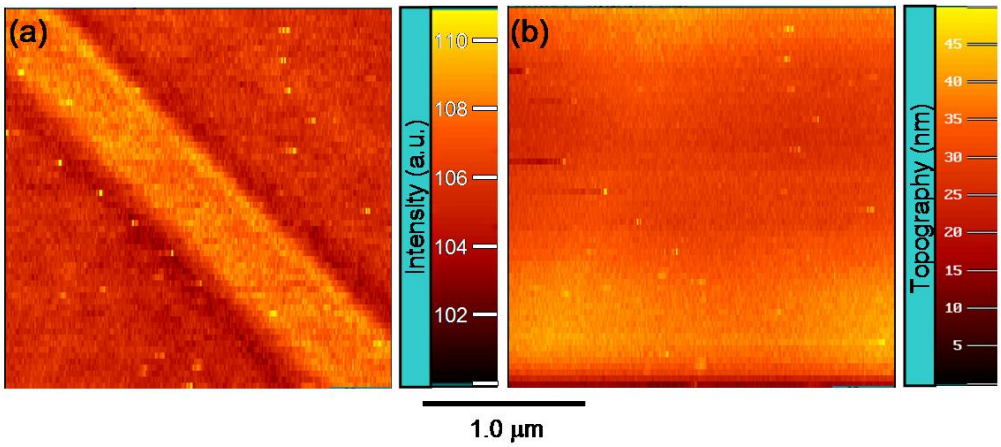

Figure 4.26. NSOM scans of a flat COI twin. The near-field intensity scan (a) shows the twin. The facet topography shown in (b) of the twin stripe is relatively small. Also small but present is a frozen-in facet boundary running at about 65° counterclockwise from the horizontal. The wavelength used is 633 nm. The temperature is 150 K.

As suggested earlier, strain could be responsible for observed lines on the edges of twins. To explain the emergence of the bright lines in Figures 4.23 and 4.25, the strain would have to evolve with temperature. One might expect a significant change in topography which does not seem to occur. Because the edge significantly changes only near the phase transition temperature, it is unlikely to be due to the temperature dependence of the strain alone. Alternatively, the strain could be changing as a result of a phase transition occurring somewhere else in the sample. However, the results of the far-field imaging do not support this picture. The far-field images of Figures 4.14, 4.15, and 4.16 show that the optical FMM optical domains evolve during the phase transition but COI optical domains do not. An evolving strain is clearly present in the FMM phase, but the same thing cannot be concluded for the COI phase.

Alternatively, the emergence of the narrow bright line could be associated with the formation of the FMM phase. In this proposed explanation, the bright line is either the remnant of COI twin or the formation of a FMM needle. The former is considered first. Since the contrast of the bright COI twin-stripe fades gradually as temperature rises (except for the bright line at the twin boundary), the FMM phase must be replacing the COI twin-stripe gradually. This picture suggests that the FMM and COI phases are mixing uniformly and gradually with temperature. However, this picture is inconsistent with the results of the far-field imaging where regions of different phase are well demarcated.

The picture of the formation of a bright FMM needle is most consistent with the results of far-field imaging, but this is not readily obvious. FMM needle-like wedges clearly form along COI twin boundaries in the far-field images of Figure 4.17. However, in these images the FMM needles appear dark, not bright as they do in the near-field. Unlike in the far-field, the FMM and COI phase domains have roughly the same brightness in the near-field and thus are more difficult to distinguish. The reader is reminded that in both phases the near-field intensity is strongly polarization dependent and can vary roughly by a factor of 2 from minimum to maximum. Even though the brightness of each NSOM scan has been re-scaled for ease of viewing and to adjust for intensity drifts, the actual brightness of each scan is different. In order for the FMM phase domains to appear bright in the near-field compared to the COI phase, the polarization should be chosen such that the COI phase

appears dark. This is indeed the case for both temperature sweeps in the case of the polarization of the bright twin-stripe. In other words, the average near-field intensity in the polarization where the twin stripe appears bright is *always* less than that in the orthogonal polarization where the stripe appears dark. In the case of Figure 4.23(c), it is about 1.5 times dimmer, in Figure 4.25(c), it is about 1.4 times dimmer, and the picture of a forming bright FMM phase domain is consistent with those facts.

The fading contrast of the COI twin-stripe observed in both Figure 4.23 and Figure 4.25 remains to be explained. This effect could be due to a temperature dependence of the reflectance, a gradually evolving strain, a light collection artifact, or a combination of the three. In Figure 4.23, the contrast of the bright twin-stripe consistently decreases with increasing temperature while the contrast of the dark twin-stripe at first increases with temperature and then decreases. Compared to the images of Figure 4.23, in Figure 4.25 the contrast of the bright twin-stripe fades more dramatically with temperature, and the contrast of the dark twin-stripe is slightly larger and does not change with temperature. Despite the quantitative differences between temperature sweeps, the emergence of the bright line in both is unmistakable.

To establish more definitively the behavior of twin boundaries during the COI to FMM transition, probing the transition with different wavelengths could be useful. For instance, Figure 4.7 shows that near 1.55 eV, there is a large far-field contrast in reflectance between the COI and FMM phases. Alternatively, a variant boundary could be probed in the near-field as a

function of temperature. Given the slow scan rate of the NSOM, such a boundary would be difficult to find.

V. Summary

This dissertation has provided a description of a cryogenic near-field scanning optical microscope (NSOM) compatible with high magnetic fields that may be useful for many different problems in condensed matter. The discussion of image formation should make a contribution to the NSOM field in general, where image interpretation remains an important on-going issue.

The investigation of quantum dots (QDs) with NSOM has provided insight to the nature of the excitonic wavefunction confinement. In particular, spatial scans of the photoluminescence from QDs formed by monolayer islands suggest they might be naturally coupled. The picture of coupled dots formed by islands in the shape of a "dumbbell" consistently describes the observed PL and is consistent with known geometries of QDs. PL excitation (PLE) spectroscopy could confirm the dumbbell picture by mapping out the excited state wavefunctions of potentially coupled dots. Although PLE experiments did not yield useful data due to insufficient near-field signal, they could do so in the future by using near-field probes with improved throughput.

Optical and phase domains of $Nd_{½}Sr_{½}MnO_3$ have successfully been imaged using far-field microscopy and NSOM. Proper interpretation of the near-field images in conjunction with far-field imaging leads to a consistent description. In both near-field and far-field imaging, optical anisotropy is observed in the low temperature charge-ordered insulator (COI) phase, the ferromagnetic metal (FMM) phase, and the paramagnetic insulator phase. The anisotropy is attributed to differences in Mn-O bond lengths in different

crystallographic orientations. NSOM images show that optical domains consistent with twinning have an associated topography. Consistent with far-field imaging, polarization-dependent features are observed in the near-field on twin boundaries and are attributed to tensile or compressive strain. The importance of strain in the evolution of optical domains and the formation of phase domains is borne out by the far-field images. During the phase transition, strain causes the appearance of FMM optical domains to evolve while COI optical domains are unchanged. Indicating that the COI to FMM phase transition upon warming is driven by strain, the preferential formation of the FMM phase on COI variant boundaries is observed in the far-field images. Though less common, the FMM phase is also observed to form needle-like wedges on COI twin boundaries. In the near-field images, evidence for the nucleation of FMM needles on COI twin boundaries has also been observed. To definitively confirm this, probing the COI to FMM transition at variant boundaries or with different wavelengths might prove insightful.

REFERENCES

[1] E. Abbe, "Beiträge zur Theorie des Mikroskops und der miroskopischen Wahrnehmung," *Archiv für mikroskopische Anatomie* **9,** 413 (1873).

[2] E. H. Synge, "A suggested model for extending microscopic resolution into the ultra-microscopic region," *Philosophical Magazine* **6,** 356 (1928).

[3] E. A. Ash and G. Nicholls, "Super-Resolution Aperture Scanning Microscope," *Nature* **237,** 510 (1972).

[4] E. Betzig and R. J. Chichester, "Single Molecules Observed by Near-Field Scanning Optical Microscopy," *Science* **262,** 1422 (1993).

[5] F. de Lange, A. Cambi, R. Huijbens, B. de Bakker, W. Rensen, M. Garcia-Parajo, N. van Hulst, and C. G. Figdor, "Cell biology beyond the diffraction limit: near-field scanning optical microscopy," *Journal of Cell Science* **114,** 4153 (2001).

[6] H. F. Hess, E. Betzig, T. D. Harris, L. N. Pfeiffer, and K. W. West, "Near-Field Spectroscopy of the Quantum Constituents of a Luminescent System," *Science* **264,** 1740 (1994).

[7] K. Matsuda, T. Saiki, S. Nomura, M. Mihara, Y. Aoyagi, S. Nair, and T. Takagahara, "Near-field optical mapping of exciton wave functions in a GaAs quantum dot," *Physical Review Letters* **91,** (2003).

[8] J. R. Guest, T. H. Stievater, G. Chen, E. A. Tabak, B. G. Orr, D. G. Steel, D. Gammon, and D. S. Katzer, "Near-Field Coherent Spectroscopy and Microscopy of a Quantum Dot System," *Science* **293,** 2224 (2001).

[9] I. I. Smolyaninov, V. N. Smolyaninova, C. C. Davis, B. G. Kim, S. W. Cheong, and R. L. Greene, "High Resolution Study of Permanent Photoinduced Reflectivity Changes and Charge-order Domain Switching in $Bi_{0.3}Ca_{0.7}MnO_3$," *Physical Review Letters* **8712,** (2001).

[10] R. S. Decca, H. D. Drew, E. Osquiguil, B. Maiorov, and J. Guimpel, "Anomalous Proximity Effect in Underdoped $YBa_2Cu_3O_{6+x}$ Josephson Junctions," *Physical Review Letters* **85,** 3708 (2000).

[11] L. L. Chang, L. Esaki, and R. Tsu, "Resonant tunnelling in semiconductor double barriers," *Applied Physics Letters* **24,** 593 (1974).

[12] R. Dingle, W. Wiegmann, and C. H. Henry, "Quantum States of Confined Carriers in Very Thin $Al_xGa_{1-x}As$-GaAs-$Al_xGa_{1-x}As$ Heterostructures," *Physical Review Letters* **33,** 827 (1974).

[13] C. A. Warwick, W. Y. Jan, A. Ourmazd, and T. D. Harris, "Does luminescence show semiconductor interfaces to be atomically smooth?," *Applied Physics Letters* **56,** 2666 (1990).

[14] D. Gammon, E. S. Snow, B. V. Shanabrook, D. S. Katzer, and D. Park, "Fine Structure Splitting in the Optical Spectra of Single GaAs Quantum Dots," *Physical Review Letters* **76,** 3005 (1996).

[15] M. Bayer, A. Schmidt, A. Forchel, F. Faller, T. L. Reinecke, P. A. Knipp, A. A. Dremin, and V. D. Kulakovskii, "Electron-Hole Transitions Between States with Nonzero Angular Momenta in the Magnetoluminescence of Quantum Dots," *Physical Review Letters* **74,** 3439 (1995).

[16] A. Zrenner, "A close look on single quantum dots," *Journal of Chemical Physics* **112,** 7790 (2000).

[17] D. Leonard, M. Krishnamurthy, C. M. Reaves, S. P. Denbaars, and P. M. Petroff, "Direct formation of quantum-sized dots from uniform coherent islands of InGaAs on GaAs surfaces," *Applied Physics Letters* **63,** 3203 (1993).

[18] L. Jacak, P. Hawrylak, and A. Wojs, *Quantum Dots* (Springer-Verlag, Berlin, 1998) pp. 1-14

[19] N. Kirstaedter, O. G. Schmidt, N. N. Ledentsov, D. Bimberg, V. M. Ustinov, A. Y. Egorov, A. E. Zhukov, M. V. Maximov, P. S. Kop'ev, and Z. I. Alferov, "Gain and differential gain of single layer InAs/GaAs quantum dot injection lasers," *Applied Physics Letters* **69,** 1226 (1996).

[20] H. Saito, K. Nishi, I. Ogura, S. Sugou, and Y. Sugimoto, "Room-temperature lasing operation of a quantum-dot vertical-cavity surface-emitting laser," *Applied Physics Letters* **69,** 3140 (1996).

[21] D. L. Huffaker, O. Baklenov, L. A. Graham, B. G. Streetman, and D. G. Deppe, "Quantum dot vertical-cavity surface-emitting laser with a dielectric aperture," *Applied Physics Letters* **70,** 2356 (1997).

[22] J. A. Lott, N. N. Ledentsov, V. M. Ustinov, A. Y. Egorov, A. E. Zhukov, P. S. Kop'ev, Z. I. Alferov, and D. Bimberg, "Vertical cavity lasers based on vertically coupled quantum dots," *Electronics Letters* **33,** 1150 (1997).

[23] N. H. Bonadeo, J. Erland, D. Gammon, D. Park, D. S. Katzer, and D. G. Steel, "Coherent Optical Control of the Quantum State of a Single Quantum Dot," *Science* **282,** 1473 (1998).

[24] M. Bayer, P. Hawrylak, K. Hinzer, S. Fafard, M. Korkusinski, R. Wasilewski, O. Stern, and A. Forchel, "Coupling and Entangling of Quantum States in Quantum Dot Molecules," *Science* **291,** 451 (2001).

[25] G. Chen, N. H. Bonadeo, D. G. Steel, D. Gammon, D. S. Katzer, D. Park, and L. J. Sham, "Optically Induced Entanglement of Excitons in a Single Quantum Dot," *Science* **289,** 1906 (2000).

[26] M. Bayer, A. Kuther, A. Forchel, A. Gorbunov, V. B. Timofeev, F. Schafer, J. P. Reithmaier, T. L. Reinecke, and S. N. Walck, "Electron and Hole g Factors and Exchange Interaction from Studies of the Exciton Fine Structure in $In_{0.60}Ga_{0.40}As$ Quantum Dots," *Physical Review Letters* **82,** 1748 (1999).

[27] S. M. Mansfield and G. S. Kino, "Solid immersion microscope," *Applied Physics Letters* **57,** 2615 (1990).

[28] W. Qiang, R. D. Grober, D. Gammon, and D. S. Katzer, "Imaging Spectroscopy of Two-Dimensional Excitons in a Narrow GaAs/AlGaAs Quantum Well," *Physical Review Letters* **83,** 2652 (1999).

[29] K. Matsuda, T. Saiki, S. Nomura, M. Mihara, and Y. Aoyagi, "Near-Field Photoluminescence Imaging of Single Semiconductor Quantum Constituents with a Spatial Resolution of 30 nm," *Applied Physics Letters* **81,** 2291 (2002).

[30] P. Schiffer, A. P. Ramirez, W. Bao, and S. W. Cheong, "Low-Temperature Magnetoresistance and the Magnetic Phase-Diagram of La1-Xcaxmno3," *Physical Review Letters* **75,** 3336 (1995).

[31] N. Mathur and P. Littlewood, "Mesoscopic Texture in Manganites," *Physics Today* **56,** 25 (2003).

[32] C. Zener, "Interaction between the D-Shells in the Transition Metals," *Physical Review* **81,** 440 (1951).

[33] K. Karrai and R. D. Grober, "Piezoelectric Tip-Sample Distance Control for near-Field Optical Microscopes," *Applied Physics Letters* **66,** 1842 (1995).

[34] K. Karrai and R. D. Grober, "Tip-sample distance control for near-field scaning optical microscopes," in *Near-Field Optics* by SPIE--The International Society for Optical Engineering, San Diego, California (July 9-10, 1995) pp. 69-81

[35] K. Karrai and R. D. Grober, "Piezo-electric tuning fork tip-sample distance control for near field optical microscopes," *Ultramicroscopy* **61,** 197 (1995).

[36] R. C. Dorf, *Modern Control Systems*. 9th ed. (Prentice Hall, Upper Saddle River, NJ, 2001).

[37] S. Kleindiek, H. S. Kim, E. Kratschmer, and T. H. P. Chang, "Miniature three-axis micropositioner for scanning proximal probe and other applications," *Journal of Vacuum Science & Technology B* **13,** 2653 (1995).

[38] P. W. Kolb, R. S. Decca, and H. D. Drew, "Capacitive sensor for micropositioning in two dimensions," *Review of Scientific Instruments* **69,** 310 (1998).

[39] G. A. Valaskovic, M. Holton, and G. H. Morrison, "Parameter control, characterization, and optimization in the fabrication of optical-fiber near-field probes," *Applied Optics* **34,** 1215 (1995).

[40] B. Palmer, *fabrication of NSOM tip* (circa 2002)

[41] H. A. Bethe, "Theory of Diffraction by Small Holes," *The Physical Review* **66,** 163 (1944).

[42] C. J. Bouwkamp, "On Bethe's Theory of Diffraction by Small Holes," *Philips Research Reports* **5,** 321 (1950).

[43] R. S. Decca, H. D. Drew, and K. L. Empson, "Investigation of the electric-field distribution at the subwavelength aperture of a near-field scanning optical microscope," *Applied Physics Letters* **70,** 1932 (1997).

[44] S. I. Bozhevolnyi, M. F. Xiao, and J. M. Hvam, "Polarization-resolved imaging with a reflection near-field optical microscope," *Journal of the Optical Society of America a-Optics Image Science and Vision* **16,** 2649 (1999).

[45] E. Betzig, J. K. Trautman, J. S. Weiner, T. D. Harris, and R. Wolfe, "Polarization contrast in near-field scanning optical microscopy," *Applied Optics* **31,** 4563 (1992).

[46] G. A. Valaskovic, M. Holton, and G. H. Morrison, "Image-contrast of dielectric specimens in transmission mode near-field scanning optical microscopy - imaging properties and tip artifacts," *Journal of Microscopy-Oxford* **179,** 29 (1995).

[47] E. B. McDaniel and J. W. P. Hsu, "Nanometer scale optical studies of twin domains and defects in lanthanum aluminate crystals," *Journal of Applied Physics* **80,** 1085 (1996).

[48] C. Durkan and I. V. Shvets, "Reflection-mode scanning near-field optical microscopy: Influence of sample type, tip shape, and polarization of light," *Journal of Applied Physics* **83,** 1171 (1998).

[49] B. Palmer, *private communication* (2003)

[50] K. D. Weston, J. A. DeAro, and S. K. Buratto, "Near-field scanning optical microscopy in reflection: A study of far-field collection geometry effects," *Review of Scientific Instruments* **67,** 2924 (1996).

[51] J. A. Cline and M. Isaacson, "Probe-sample interactions in reflection near-field scanning optical microscopy," *Applied Optics* **34,** 4869 (1995).

[52] R. S. Decca, *private communication* (2003)

[53] C. Obermuller and K. Karrai, "Far field characterization of diffracting circular apertures," *Applied Physics Letters* **67,** 3408 (1995).

[54] M. Born and E. Wolf, *Principles of Optics*, 7th ed. (Cambridge University Press, Cambridge, 1999) pp. 753-754

[55] E. D. Palik, *Handbook of Optical Constants of Solids* (Academic Press, Inc., New York, 1985) pp. 294, 438

[56] C. Durkan and I. V. Shvets, "Polarization effects in reflection-mode scanning near-field optical microscopy," *Journal of Applied Physics* **83,** 1837 (1998).

[57] P. Y. Yu and M. Cardona, *Fundamentals of Semiconductors* (Springer-Verlag, Berlin, 1996) pp. 66, 70, 157, 258, 271, 280, 457-474

[58] C. Bosio, J. L. Staehli, M. Guzzi, G. Burri, and R. A. Logan, "Direct-energy-gap dependence on Al concentration in $Al_xGa_{1-x}As$," *Physical Review B* **38,** 3263 (1988).

[59] E. Merzbacher, *Quantum Mechanics*, 2nd ed. (Wiley, New York, 1970) pp. 105-108

[60] N. Watanabe and H. Kawai, "Single and coupled double-well GaAs/AlGaAs and energy-dependent light-hole mass," *Journal of Applied Physics* **60,** 3696 (1986).

[61] V. Srinivas, *Exciton Dynamics in GaAs Quantum Wells*, Ph.d. thesis, University of Maryland, College Park, 1992

[62] Q. Wu, R. D. Grober, D. Gammon, and D. S. Katzer, "Spectroscopic imaging in a narrow GaAs quantum well," *Sixth International Workshop on Nonlinear Optics and Excitation Kinetics in Semiconductors (NOEKS 2000)* **221,** 505 (2000).

[63] D. Gammon, E. S. Snow, and D. S. Katzer, "Excited State Spectroscopy of Excitons in Single quantum dots," *Applied Physics Letters* **67,** 2391 (1995).

[64] W. Qiang, R. D. Grober, D. Gammon, and D. S. Katzer, "Excitons, biexcitons, and electron-hole plasma in a narrow 2.8-nm GaAs/$Al_xGa_{1-x}As$ quantum well," *Physical Review B (Condensed Matter)* **62,** 13022 (2000).

[65] D. E. Aspnes, "GaAs lower conduction-band minima - ordering and properties," *Physical Review B* **14,** 5331 (1976).

[66] T. Förster, *Annals of Physics* **2,** 55 (1948).

[67] M. Stavola, D. L. Dexter, and R. S. Knox, "Electron-hole pair excitation in semiconductors via energy-transfer from an external sensitizer," *Physical Review B* **31,** 2277 (1985).

[68] M. Batsch, T. Meier, P. Thomas, M. Lindberg, S. W. Koch, and J. Shah, "Dipole-dipole coupling of excitons in double-quantum wells," *Physical Review B* **48,** 11817 (1993).

[69] N. W. Aschroft and N. D. Mermin, *Solid State Physics* (Harcourt Brace College Publishers, Fort Worth, 1976) pp. 398-400

[70] J. R. Reitz, F. J. Milford, and R. W. Christy, *Foundations of Electromagnetic Theory*, 4th ed. (Addison-Wesley Publishing Company, Reading, Massachusetts, 1993) pp. 131-132

[71] T. Saiki and K. Matsuda, "Near-field optical fiber probe optimized for illumination-collection hybrid mode operation," *Applied Physics Letters* **74,** 2773 (1999).

[72] R. Kajimoto, H. Yoshizawa, H. Kawano, H. Kuwahara, Y. Tokura, K. Ohoyama, and M. Ohashi, "Hole-concentration-induced transformation of the magnetic and orbital structures in $Nd_{1-x}Sr_xMnO_3$," *Physical Review B* **60,** 9506 (1999).

[73] M. Uehara, K. H. Kim, and S. W. Cheong, *personal communication with H. D. Drew - Phase Diagram of* $La_{1-x}Ca_xMnO_3$ (circa 1998)

[74] A. Tomer, *Structure of Metals Through Optical Microscopy* (ASM International, United States, 1991).

[75] Z. Nishiyama, *Martensitic Transformation*, edited by M. Fine, M. Meshii, and C. Wayman (Academic Press, New York, 1978) pp. 23

[76] V. Podzorov, B. G. Kim, V. Kiryukhin, M. E. Gershenson, and S. W. Cheong, "Martensitic accommodation strain and the metal-insulator transition in manganites," *Physical Review B* **6414,** (2001).

[77] T. Maki, S. Shimooka, T. Arimoto, and I. Tamura, "Morphology of Thin Plate-Like Martensite in Fe-Ni-C Alloys," *Transactions of the Japan Institute of Metals* **14,** 62 (1973).

[78] Y. Moritomo, H. Kuwahara, Y. Tomioka, and Y. Tokura, "Pressure effects on charge-ordering transitions in Perovskite manganites," *Physical Review B* **55,** 7549 (1997).

[79] J. H. Jung, H. J. Lee, T. W. Noh, E. J. Choi, Y. Moritomo, Y. J. Wang, and X. Wei, "Melting of charge/orbital ordered states in $Nd_{½}Sr_{½}MnO_3$: Temperature and magnetic-field-dependent optical studies," *Physical Review B* **62,** 481 (2000).

[80] D. B. Romero, Y. Moritomo, J. F. Mitchell, and H. D. Drew, "Competition of charge, orbital, and ferromagnetic correlations in layered manganites," *Physical Review B* **6313,** (2001).

[81] H. J. Lee, J. H. Jung, Y. S. Lee, J. S. Ahn, T. W. Noh, K. H. Kim, and S. W. Cheong, "Optical properties of a $Nd_{0.7}Sr_{0.3}MnO_3$ single crystal," *Physical Review B* **60,** 5251 (1999).